STRUCTURE CHANGES AT LOW-INDEX Pd SURFACES INDUCED BY ADSORPTION AND EPITAXY

PAR

Nicolas WAELCHLI

physicien diplômé de l'Université de Neuchâtel
originaire de Wynigen (BE)

Abstract

Structure changes at the (110) and (100) surfaces of palladium are studied by means of scanning tunneling microscopy (STM) and reflection absorption infrared spectroscopy (RAIRS) of adsorbed CO. The structural modifications of the Pd substrates are induced by hydrogen chemisorption, homoepitaxial growth and silicide formation.

The homoepitaxial growth on Pd(110) has been investigated in the temperature range 190 K $\leq$ T $\leq$ 400 K. At substrate temperatures below 295 K, Pd adatoms were found to nucleate as monoatomic chains in the Pd(110) troughs running along the $[\bar{1}10]$ direction. At higher temperatures two-dimensional lens shaped islands grow. The dependence of the island density on temperature and deposition rate has been quantitatively analyzed and related to nucleation theory. Surprisingly Pd adatom diffusion was found to be isotropic with a migration barrier of (0.14 $\pm$ 0.05) eV. The anisotropic island shapes are caused by anisotropic corner rounding. The stable island was determined to be the dimer in the low and the tetramer in the high temperature range. At T $\geq$ 300 K multilayers are found to grow in a layer-by-layer mode.

The effect of hydrogen adsorption on the Pd(110) surface structure has been studied at room temperature. Depending on the partial pressure of hydrogen, two different reconstructions of Pd(110) have been observed: a (1 $\times$ 3) phase at hydrogen pressures in the 10^{-9} mbar range and an additional (1 $\times$ 2) phase at $p_{H_2} \geq 5 \times 10^{-8}$ mbar. Both reconstructions are found to be of the missing-row type. The evolution of the surface reconstructions has been followed in situ.

The growth and reaction of Si on the Pd(110) surface have been studied in the temperature range 100 K $\leq$ T $\leq$ 600 K. The growth scenario is found to depend strongly on the deposition temperature, which determines the competition between Si subsurface diffusion and silicide formation. Below 140 K the Si deposition on the substrate is nonreactive and amorphous Si clusters grow. The resonance frequency of CO adsorbed on the Si clusters is centered at 2104 cm^{-1}. With increasing temperature amorphous silicide clusters (140 K - 320 K) and well-shaped crystalline silicide islands ($\geq$ 320 K) grow at the metal surface. Below 450 K the ordered silicide grows in strained islands while above 450 K strain is partially relieved through misfit dislocations. The vibrational spectrum of CO adsorbed on palladium-silicide

films is characterized by two absorption bands: a high frequency mode at 2090 cm^{-1} (amorphous silicide) or 2074 cm^{-1} (crystalline silicide) and a low frequency mode at 2000 cm^{-1}.

Silicide formation has also been studied at the Pd(100) surface in the temperature range 100 K $\leq$ T $\leq$ 600 K. Below 150 K, the Si deposition is nonreactive and amorphous Si clusters grow. The resonance frequency of CO adsorbed on the Si clusters is centered at 2100 cm^{-1}. At T $\geq$ 150 K silicide clusters grow at the Pd(100) surface. Surprisingly the resonance frequency of adsorbed CO does not shift. Thus the chemical nature of the Si atoms in the silicide resembles that of unreacted Si. The data suggest that silicide grows as amorphous alloy with randomly varying chemical composition. In contrast to the Pd(110) surface, no crystalline silicide layers could be grown on Pd(100).

Résumé

Des changements de structure aux surfaces (110) et (100) du palladium sont étudiés par microscopie à effet tunnel (STM) et spectroscopie vibrationnelle infrarouge (RAIRS) du CO adsorbé. Les modifications structurelles des substrats de Pd sont induites par chimisorption d'hydrogène, croissance homoépitaxiale et formation de siliciure.

La croissance homoépitaxiale sur Pd(110) a été étudiée dans la gamme de température 190 K $\leq$ T $\leq$ 400 K. Aux températures du substrat inférieures à 295 K, les adatomes de Pd nucléent en chaînes monoatomiques dans les sillons de Pd(110) le long de la direction $[\bar{1}10]$. À plus hautes températures des îlots bidimensionels lenticulaires croissent. La densité d'îlots a été analysée quantitativement en fonction de la température et du taux de déposition et mise en relation avec la théorie de la nucléation. Étonnamment on a trouvé que la diffusion des adatomes de Pd est isotrope avec une barrière de migration de (0.14 ± 0.05) eV. Les formes anisotropes des îlots sont causées par le contournement anisotrope des coins. L'îlot stable a été déterminé comme étant le dimère dans le domaine des basses et le tétramère dans le domaine des hautes température. À T $\geq$ 300 K les multicouches croissent suivant le mode couche-par-couche.

L'effet de l'adsorption d'hydrogène sur la structure de la surface (110) du Pd ont été étudiées à température ambiante. Dépendant de la pression partielle d'hydrogène, deux reconstructions différentes de Pd(110) ont été observées: une phase (1×3) à des pressions d'hydrogène dans le domaine 10^{-9} mbar et une autre phase (1×2) à $p_{H_2} \geq 5 \times 10^{-8}$ mbar. Les deux reconstructions sont du type "rangée manquante". L'évolution de ces reconstructions de surface a été suivie in situ.

La croissance et la réaction du Si sur la surface (110) du Pd a été étudiée dans la gamme de température 100 K $\leq$ T $\leq$ 600 K. Le scénario de croissance dépend fortement de la température de déposition, qui détermine la compétition entre la diffusion subsurface du Si et la formation de siliciure. Au-dessous de 140 K, la déposition de Si sur le substrat est non-réactive et des agrégats amorphes de Si croissent. La fréquence de résonance du CO adsorbé sur les agrégats de Si est centrée à 2104 cm^{-1}. En augmentant la température, des agrégats amorphes de siliciure (140 K - 320 K) puis des îlots cristallins de siliciure ($\geq$ 320 K) croissent

à la surface du métal. En dessous de 450 K le siliciure ordonné croît en ilots distordus tandis qu'au-dessus de 450 K la tension est partiellement réduite par des dislocations de désaccord de maille. Le spectre vibrationel du CO adsorbé sur les films de siliciure de palladium est caractérisé par deux bandes d'absorption: un mode à haute fréquence à 2090 cm^{-1} (siliciure amorphe) ou 2074 cm^{-1} (siliciure cristallin) et un mode à basse fréquence à 2000 cm^{-1}.

La formation de siliciure a aussi été étudiée à la surface (100) du Pd dans la gamme de température 100 K $\leq$ T $\leq$ 600 K. Au-dessous de 150 K, la déposition de Si est non-réactive et des agrégats amorphes de Si croissent. La fréquence de résonance du CO adsorbé sur les agrégats de Si est centrée à 2100 cm^{-1}. À T $\geq$ 150 K des agrégats amorphes de siliciure croissent sur la surface (100) du Pd. Étonnamment la fréquence de résonance du CO adsorbé n'est pas décallée. La nature chimique des atomes de Si dans le siliciure ressemble donc à celle du Si non-réagit. Les données suggèrent que le siliciure croit comme un alliage amorphe avec une composition chimique variant aléatoirement. Au contraire de la surface (110) du Pd, on ne peut pas faire croître des couches cristallines de siliciure sur Pd(100).

Table of contents

1. Introduction

The last ten years have witnessed a substantial progress in the understanding of surface phenomena on the microscopic level. This is due to the development of novel experimental and theoretical techniques. On the theoretical side, todays computer power allows the application of ab-initio methods to surface problems. Experimentally the development of scanning probe microscopies has opened the possibility to characterize surfaces and to study surface processes on the atomic level. The microscopic scale studies are essential to acquire a deeper knowledge of basic surface phenomena in order to understand phenomena like heterogeneous catalysis, epitaxial growth or corrosion.

The purpose of the present thesis is to induce and to control on the atomic scale structural changes at low-index surfaces of Pd. In this context some physical mechanisms that can induce structure changes at metal surfaces are briefly introduced in the following.

The outermost layers of most metals are relaxed due to the smoothing of the surface electronic charge density, but the in-plane structure retains the bulk termination. However, some clean metal surfaces are known to spontaneously reconstruct in a UHV environment, i.e. the in-plane surface structure deviates from the bulk plane structure. We have to distinguish between two types of reconstructions: displacive reconstructions and reconstructions involving mass transport and interatomic bond changes [1]. In general displacive reconstructions are favored on bcc metal surfaces like W(100) and Mo(100) [2] whereas mass transport reconstructions are favored on fcc metal surfaces [1]. Examples are the fcc(110) surfaces of the 5d metals Ir, Pt and Au which show reconstructions of the (1 × 2) missing-row type [3]. It is believed that the minimization of the kinetic energy of the s electrons are the main reasons for this type of reconstruction to occur [4].

The charge transfer resulting from the adsorption of molecules or atoms from the gas phase onto a metal surface can also induce a variety of reconstructions on surfaces which are otherwise stable [5]. The (110) surfaces of the 3d and 4d metals Pd, Ag, Cu and Ni are unreconstructed when free of impurities, but they show an inherent tendency towards reconstruction when certain molecules are adsorbed. Even the weak chemisorption of hydrogen is known to induce a (1 × 2) missing-row reconstruction of the (110) surfaces of Ni

and Pd [6, 7]. Also displacive reconstructions may be induced by adsorption. For instance a low-temperature (1 × 2) pairing-row reconstruction of Pd(110) is induced by hydrogen adsorption [8, 9].

It is important to note that the displacive reconstructions are very rapid and completely reversible [1, 2] such that they cannot be controlled kinetically. In contrast, mass transport reconstructions are slow processes which can be controlled kinetically such that tailoring of surface structure is possible.

A particularly attractive technique for the manipulation of surface structure and morphology is epitaxial growth. The term epitaxy refers to the ordered growth of crystalline layers on a single crystal surface such that the orientations of the two crystals bear some well-defined relationship. The thermodynamic picture of epitaxial growth based on the idea of minimizing the surface free energy predicts three growth modes: layer, island and layer plus island growth [10]. Thermodynamic growth is only established at sufficiently high substrate temperatures and growth manipulation is difficult to realize. Most growth experiments, however, are run far from thermal equilibrium for instance at relatively low temperatures and high deposition rates. The grown structures now reflect kinetic behavior which can be exploited to manipulate the growth morphology. By exploiting the dependence of the mobility of adsorbed atoms on the symmetry of the surfaces and on the substrate temperature, it is possible to grow nanostructures of varying shape and size [11]. Square or irregular-shaped adislands are grown on fcc(100) surfaces [12, 13]. The anisotropy of the fcc(110) surface allows to grow one-dimensional adislands [14, 15]. On fcc(111) surfaces the island shape varies between fractals, triangles and hexagones [16, 17]. In general, shape and size can be varied independently by two free parameters: the temperature and the deposition rate.

The special case of epitaxial growth involving a chemical reaction between the deposited atoms and the substrate atoms is referred to reactive epitaxy. The chemical reaction offers a further degree of freedom which can be controlled kinetically. Many systems have been investigated with respect to surface alloying [18-20]. Not expected from their bulk phase diagrams, surface reaction may take place. For examples, metals which are not miscible in the bulk intermix at surfaces [21, 22]. The formation of covalent Si-metal compounds (silicide)

2

on a Si surface is of great interest for its application in semiconductor devices [23, 24]. More particularly cobalt and iron silicides are well known and already introduced in silicon technology [25, 26]. The most common methods to produce silicide on Si surfaces are reactive deposition epitaxy (RDE) and solid phase epitaxy (SPE). Various crystalline phases of silicides are grown on low-index Si surfaces [27-30]. The Si deposition on metal surfaces, however, has rarely been investigated [31, 32].

In chapter 3, we present our analysis of the diffusion, nucleation and aggregation mechanisms of Pd adatoms on Pd(110). The density and the shape of the Pd islands have been quantitatively analyzed. It has been possible to grow a variety of highly anisotropic islands including monoatomic Pd chains. In chapter 4 a detailed and systematic STM study of the hydrogen-induced reconstruction of the Pd(110) surface will be presented. The evolution of the reconstruction at room temperature from a (1×1) to a (1×3) structure has been followed in situ as a function of the hydrogen exposure. In chapter 5 and 6 we study the reactive epitaxial growth of Si on the (110) and (100) surface of Pd. We evaluate how the surface chemical composition and morphology can be controlled by kinetics. On the (110) surface we are able to grow a crystalline silicide structure while on the (100) surface only amorphous silicide is formed. We discuss in detail the relevant kinetic processes.

The experimental results were obtained by a combination of scanning tunneling microscopy (STM) and reflection absorption infrared spectroscopy (RAIRS) of adsorbed CO. The CO stretch frequency is a sensitive probe of the local chemical environment and thus a valuable probe of the surface chemical composition whereas STM gives the atomic-level surface structure (chapter 2). This combination offers a unique possibility of correlating surface chemical analysis with atomic-level surface structure. This is particularly important in the case of very reactive systems like Si/Pd.

References

[1] P. J. Estrup, *Reconstruction of Metal Surfaces* in *Chemistry and Physics of Solid Surfaces V*, R. Vanselow and R. Howe, Springer, Berlin (1984).
[2] P. J. Estrup, *Surface phases of reconstructed tungsten (100) and molybdenum (100)*, Surf. Sci. **299/300**, 722 (1994).
[3] T. Gritsch, D. Coulman, R. J. Behm and G. Ertl, *A scanning tunneling microscopy investigation of the structure of the Pt(110) and Au(110) surfaces*, Surf. Sci. **257**, 297 (1991).
[4] K. M. Ho and K. P. Bohnen, *Stability of the Missing-Row Reconstruction on fcc (110) Transition-Metal Surfaces*, Phys. Rev. Lett. **59**, 1833 (1987).

[5] D. P. Woodruff, *Adsorbate-induced reconstruction of surfaces: an atomistic alternative to microscopic faceting?*, J. Phys.: Condens. Matter **6**, 6067 (1994).

[6] L. P. Nielsen, F. Besenbacher, E. Laegsgaard and I. Stensgaard, *Nucleation and growth of a H-induced reconstruction of Ni(110)*, Phys. Rev. B **44**, 13156 (1991).

[7] J. Yoshinobu, H. Tanaka and M. Kawai, *Elucidation of hydrogen-induced (1 x 2) reconstructed structures on Pd(110) from 100 to 300 K by scanning tunneling microscopy*, Phys. Rev. B **51**, 4529 (1995).

[8] K. H. Rieder, M. Baumberger and W. Stocker, *Selective Transition of Chemisorbed Hydrogen to Subsurface Sites on Pd(110)*, Phys. Rev. Lett. **51**, 1799 (1983).

[9] H. Niehus, C. Hiller and G. Comsa, *ROW PAIRING INDUCED BY HYDROGEN ADSORPTION AT Pd(110)*, Surf. Sci. Lett. **173**, L599 (1986).

[10] A. Zangwill, *Physics at surfaces*, Cambridge University Press, Cambridge (1988).

[11] H. Röder, E. Hahn, H. Brune, J. P. Bucher and K. Kern, *Building one- and two-dimensional nanostructures by diffusion-controlled aggregation at surfaces*, Nature **366**, 141 (1993).

[12] E. Kopatzki, S. Günther, W. Nichtl-Pechler and R. J. Behm, *Homoepitaxial growth on Ni(100) and its modification by a preadsorbed oxygen adlayer*, Surf. Sci. **284**, 154 (1993).

[13] E. Hahn, E. Kampshoff, N. Waelchli and K. Kern, *Strain Driven fcc-bct Phase Transition of Pseudomorphic Cu Films on Pd(100)*, Phys. Rev. Lett. **74**, 1803 (1995).

[14] J. P. Bucher, E. Hahn, P. Fernandez, C. Massobrio and K. Kern, *Transition from One- to Two-Dimensional Growth of Cu on Pd(110) Promoted by Cross-Exchange Migration*, Europhys. Lett. **27**, 473 (1994).

[15] E. Hahn, E. Kampshoff, A. Fricke, J. P. Bucher and K. Kern, *Pseudomorphic growth of thin Cu films on Pd(110)*, Surf. Sci. **319**, 277 (1994).

[16] H. Brune, C. Romainczyk, H. Röder and K. Kern, *Mechanism of the transition from fractal to dendritic growth of surface aggregates*, Nature **369**, 469 (1994).

[17] T. Michely, M. Hohage, M. Bott and G. Comsa, *Inversion of Growth Speed Anisotropy in Two Dimensions*, Phys. Rev. Lett. **70**, 3943 (1993).

[18] P. W. Murray, I. Stensgaard, E. Laegsgaard and F. Besenbacher, *Growth and structure of Pd alloys on Cu(100)*, Surf. Sci. **365**, 591 (1996).

[19] S. Rousset, S. Chiang, D. E. Fowler and D. D. Chambliss, *Intermixing and Three-Dimensional Islands in the Epitaxial Growth of Au on Ag(110)*, Phys. Rev. Lett. **69**, 3200 (1992).

[20] D. D. Chambliss and S. Chiang, *Surface alloy formation studied by scanning tunneling microscopy: Cu(100)+Au-c(2x2)*, Surf. Sci. Lett. **264**, L187 (1992).

[21] L. P. Nielsen, F. Besenbacher, I. Stensgaard and E. Laegsgaard, *Initial Growth of Au on Ni(110): Surface Alloying of Immiscible Metals*, Phys. Rev. Lett. **71**, 754 (1993).

[22] H. Röder, R. Schuster, H. Brune and K. Kern, *Monolayer-Confined Mixing at the Ag-Pt(111) Interface*, Phys. Rev. Lett. **71**, 2086 (1993).

[23] V. G. Lifshits, A. A. Saranin and A. V. Zotov, *Surface Phases on Silicon: Preparation, Structures, and Properties*, Wiley, Chichester (1994).

[24] S. P. Murarka, *Silicides for VLSI Applications*, Academic Press, Orlando (1983).

[25] A. H. Reader, A. H. van Ommen, P. J. W. Weijs, R. A. M. Wolters and D. J. Oostra, *Transition metal silicides in silicon technology*, Rep. Prog. Phys. **56**, 1397 (1992).

[26] R. Miranda, J. Alvarez and A. L. Vazquez de Parga, *L'électronique des alliages fer-silicium*, La Recherche **26**, 42 (1995).

[27] J. M. Gallego, J. Alvarez, J. J. Hinarejos, E. G. Michel and R. Miranda, *The growth and characterization of iron silicides on Si(100)*, Surf. Sci. **251/252**, 59 (1991).

[28] W. Raunau, H. Niehus, T. Schilling and G. Comsa, *Scanning tunneling microscopy and spectroscopy of iron silicide epitaxially grown on Si(111)*, Surf. Sci. **286**, 203 (1993).

[29] H. Itoh, S. Narui, H. Tanabe and T. Ichinokawa, *Nucleation and surface reconstruction of Pd on Si(100) observed by scanning tunneling microscopy*, Sur. Sci. **284**, 236 (1993).

[30] U. K. Köhler, J. E. Demuth and R. J. Hamers, *Surface Reconstruction and the Nucleation of Palladium Silicide on Si(111)*, Phys. Rev. Lett. **60**, 2499 (1988).

[31] M. C. Muñoz, F. Soria and J. L. Sacedon, *THE INTERACTION OF Si WITH Al(111) SURFACES ABOVE ROOM TEMPERATURE*, Surf. Sci. **189/190**, 204 (1987).

[32] K. Nishimori, H. Tokutaka, H. Sumi and N. Ishihara, *Silicide Reaction of Si Thin Film Deposited on Platinum Metal*, J. Vac. Soc. Japan **34**, 143 (1991).

4

2. Experimental methods

2.1. Scanning Tunneling Microscopy (STM)

2.1.1. General principles

The scanning tunneling microscope (STM) has been invented in 1982 by G. Binnig and H. Rohrer [1, 2]. The principle of the STM is straightforward. It consists essentially in scanning a metal tip over a surface while maintaining a constant tunneling current through the vacuum gap (s $\approx$ 10 Å). The very high resolution of the STM is based on the strong distance dependence of the tunnel current J_T between tip and sample. A rough estimation assuming two flat parallel electrodes with an applied voltage V_T and separated by a distance s reveals:

$$J_T \sim (V_T/s) \exp(-A\sqrt{\phi}s) \tag{2.1}$$

where A $\approx$ 1.025 (eV)$^{-1/2}$Å^{-1} and ϕ the average work function. With typical work functions of a few eV, J_T changes by an order of magnitude for every Å change of s. Figure 2.1 shows the principle of operations of the STM [1, 2].
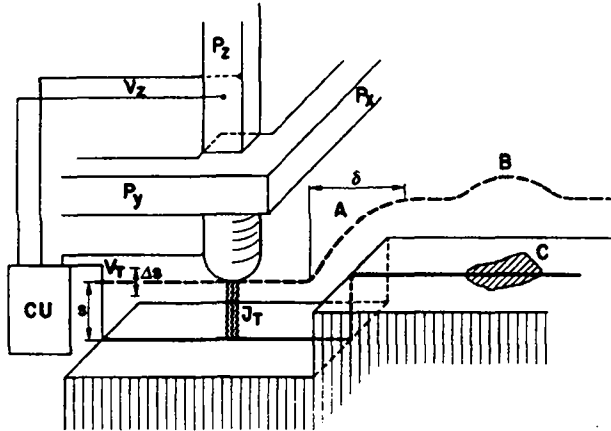
Fig. 2.1: Principle of the STM [1, 2].

The tip is fixed to a piezodrive P_x, P_y, P_z. P_x and P_y scan the tip over the surface. A voltage V_z is applied to P_z by the control unit (CU) such that J_T remains constant during the scan. Thus at constant ϕ and s and according to equation 2.1, V_z reflects the topography of the surface, for instance at a step (A) in figure 2.1. The lateral resolution δ at a step is a matter of

sharpness of the tip. A naive calculation gives $\delta \approx 3\sqrt{R}$ where R is the radius of curvature (as δ in Å). A resolution of $\delta \approx 10$ Å requires $R \approx 10$ Å. A change in the work function ϕ, for instance at the place of adsorbed atoms, will induce a corresponding change in s according to equation 2.1 (zone C in figure 2.1).

2.1.2. Variable temperature STM

The STM used for the experiments is based on the beetle (or Besocke) type [3]. The coarse tip distance approach and positioning was developed by J. Frohn and coworkers [4]. Our STM is schematized in figure 2.2: it consists of a microscope disc (aluminium) which holds four equal piezoceramic tubes.
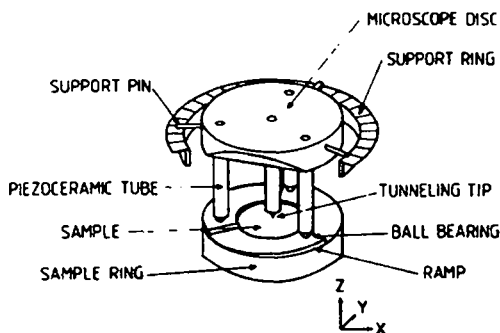
Fig. 2.2: Sketch of the Besocke STM [4].

The microscope is temperature compensated to first order since the thermal expansion of all four piezo tubes is equal, leaving the tip to sample distance unchanged upon temperature variations. This facilitates temperature-dependent measurements with fast temperature equilibration and slow drift. The temperature variability is therefore restricted to the range 150 - 550 K, limited by the vibrations due to liquid helium flow and the piezo tube depolarization temperature. The inner tube holds the STM tip, the outer tubes are provided with small metal spheres and act as positioners. Each tube is covered with several electrodes connected by thin wires (Cu, 50 μm diameter). The STM can be mechanically decoupled from the support ring by lowering it down onto the sample holder. The sample holder consists mainly of a molybdenum ring with three ramps cut into it, each 0.4 mm high and spanning an arc of 120° (figure 2.2). The tip approach is achieved by applying triangular voltage pulses to the outer piezo tube electrodes rotating the microscope clockwise down the ramps until tip

6

comes within tunneling distance. Sample scans are in general performed by the inner piezo tube. The tip is made of a 0.25 mm diameter tungsten wire electrochemically etched at one extremity in a NaOH solution [5].

2.2. Reflection Absorption Infrared Spectroscopy (RAIRS)

2.2.1. General principles

Since metals are nontransparent to infrared radiation, vibrations of adsorbed molecules on metal surfaces must be investigated by reflection. R. G. Greenler showed using classical electrodynamics that under certain conditions a single reflection is sufficient to obtain useful spectra [6]. He introduced a three-layer model (vacuum/adsorbed layer/metal) displayed in figure 2.3.a. According to this model, he solved the wave equations and calculated the absorption factor A:

$$A = (R^0 - R) / R^0 \qquad (2.2)$$

where R is the reflectance (ratio of intensites) of the modeled system and R^0 the reflectance with $k_2 = 0$ (figure 2.3). The results of his model for metal surfaces are the following (see also reference [7]):

1) Surface selection rule: Only molecular vibrations with a component of their dipole moment perpendicular to the surface are dipole active because the light component polarized parallel to the metal surface undergoes a 180° phase shift upon reflection such that the resulting electric field vanishes.

2) The RAIRS experiment is most effective near grazing incident angle as revealed by the calculated curves in figure 2.3.b.

3) The absorption is largest for highly reflecting metal (k_3 large) and for adsorbates with high absorption coefficients k_2.

Notice: in the spectra presented in this thesis (chapters 5, 6) the value reported is the normalized reflectance r:

$$r = 1 - A = R / R^0 \qquad (2.3)$$
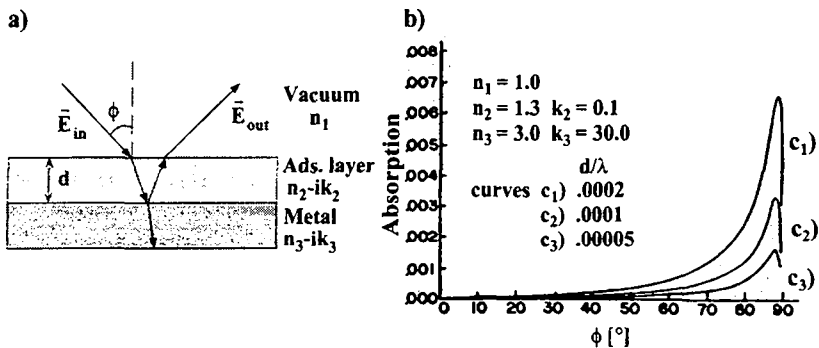
Fig. 2.3: a) Three-layer model of Greenler [6] (vacuum/adsorbed layer/metal). $n_j - ik_j$ is the optical constant of the layer j, d is the thickness of the adsorbed layer. b) Calculated absorption factor as a function of angle of incidence ϕ for polarization perpendicular to the surface and for three different values d/λ (λ: IR-light wavelength).

The RAIRS measurements of this work are made with a Fourier transform infrared (FTIR) spectrometer. The design of the FTIR spectrometer is based on the classical interferometer originally designed by A. A. Michelson in 1891. It is a device that can divide a beam of IR radiation through a beamsplitter into two beams and then recombine them after a path difference has been intoduced by a movable mirror, thereby creating interferences. The intensity of the emerging beam can be measured by a detector [8]. The main advantage of using a FTIR spectrometer is the high sensitivity compared to conventional dispersive instruments [7]. The high sensitivity of FTIR spectrometer is extremly valuable with regard to the spectroscopy of adsorbed molecules.

2.2.2. Infrared absorption spectra of chemisorbed CO

In this paragraph a brief introduction to vibrational spectra of CO chemisorbed on metal surfaces is presented. All RAIRS experiments in this work deal with this molecule which is the best studied chemisorbed species on metals.

A N-atom species has 3N degrees of freedom: 3 are translations, 3 are rotations (2 for a linear species) and 3N-6 are vibrations (3N-5 respectively). When the molecule is adsorbed on a surface, all degrees of freedom are converted to vibrations (including hindered translations and rotations). In case of adsorbed CO, only the internal C-O stretching mode v_1 has a frequency above 500 cm^{-1} and thus lies within the range accessible to the conventional

8

IR detector used in the present studies. The gas phase frequency of the internal vibration $\bar{v}_1 = 2143\,\text{cm}^{-1}$ is shifted to lower frequencies when CO adsorbs on a metal surface. The frequency shift induced by the bonding is due to three contributions [7]: the bonding configuration, the coordination of the substrate atom(s) and the local chemical environment.

The bonding mechanism of the CO molecule on a metal surface is well explained by the Blyholder model [9]. The CO-metal bonding is formed by charge transfer from the 5σ molecular orbital of CO to the metal, with backdonation of the metal d electrons into the unoccupied $2\pi^*$ orbital of CO. Since the CO 5σ orbital in only weakly bonding with respect to the C-O bond and the $2\pi^*$ is strongly antibonding, the C-O bond is weakened upon adsorption and the corresponding vibrational frequency is lower than in the gas phase. The three contributions to the frequency shift mentioned above can be qualitatively understood with the help of this model.

The bonding configuration of chemisorbed CO gives rise to the largest frequency shift. It is a downward shift depending on the configuration: the higher the coordination of the CO, the larger is the amount of backdonation and the lower is the frequency. In general, the following empirical relation holds [7]:

Linear (on-top):	$2130 - 2000\,\text{cm}^{-1}$
Bridge:	$2000 - 1860\,\text{cm}^{-1}$
Threefold:	$1920 - 1800\,\text{cm}^{-1}$
Fourfold:	$1800 - 1700\,\text{cm}^{-1}$

This assignment should be regarded only as a rough guide to the possible CO configurations. For example, the bridge domain and the threefold domain overlap. Some problems have been encountered in determining the configuration of CO on Ni(111) solely based on the vibrational frequency which lies in this overlapping domain. Quantitative surface structure analysis was the only reliable way to determine these adsorption sites [10].

The key parameter which determines the vibrational frequency is the coordination of the substrate atom(s) to which CO chemisorbs. This has particular consequences for adsorption at defect sites like steps or kinks. In general the C-O stretch frequency is lower for CO adsorbed at steps (or kinks) than for CO adsorbed at terrace sites [7]. With respect to the bonding

model of Blyholder it indicates that CO is more strongly bound to steps (or kinks) than to terrace sites.

The local chemical environment is the third main contribution to the frequency shift. It includes the chemical composition of the metal substrate, effects due to coadsorbates and the CO coverage dependent frequency shift. The coverage dependent frequency shift is usually to higher frequencies. Two effects contribute to it: the dipole coupling between adsorbed molecules (dynamic shift) and the change in the electronic density distribution between CO and the metal with increasing coverage (chemical or static shift). Exclusively upward dipole shifts of 25 - 50 cm^{-1} with increasing coverage have been experimentally observed [7]. This shift has been accurately calculated by means of classical electrodynamics [11]. The intensity transfer from the low-frequency vibrations to their higher frequency counterparts is one consequence of the dipolar interaction between adsorbed molecules coupling their individual vibrations [12]. The chemical shift can be positive or negative depending on the substrate. It is based on the fact that the π^* backbonding depends on the relative energies of the Fermi level and the CO $2\pi^*$ level. It can be shown that for CO adsorbed on transition metals, the frequency increases with CO coverage whereas for CO adsorbed on noble metals it decreases [7].

The actual C-O stretch frequency is different at various metal surfaces mainly because of the bonding mechanism described above. The amount of the π^* backdonation differs from metal to metal and thus changes the vibrational frequency in a way characteristic for each substrate. The C-O stretch frequency has been measured at various metal surfaces [7, 13] and can be used as chemical fingerprint. The use of the C-O vibrational frequency as chemical fingerprint is extremly valuable at heterogeneous surfaces [14-16]. In the frame of this work, we will use this method to qualitatively and quantitatively determine the chemical composition of heterogeneous Si/Pd surfaces (chapters 5 and 6). The RAIR spectra of CO adsorbed on Si and on silicide will be discussed with respect to the surface morphologies characterized by STM.

2.3. Experimental setup

The experiments were carried out in a two-chamber stainless-steel UHV system with a base pressure of 2×10^{-10} mbar (figure 2.4) [5, 14, 17].
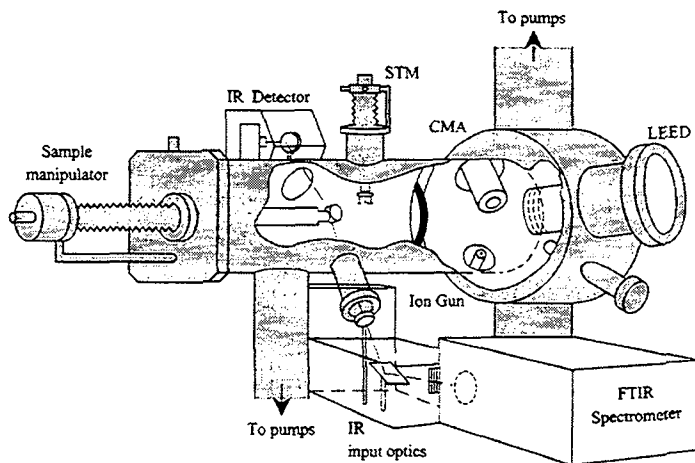
Fig. 2.4: Schematic view of the UHV (ultra-high-vacuum) system: on the right-hand side, the sample preparation chamber; on the left-hand side, the STM/RAIRS chamber [5, 14, 17]. Acronyms: LEED = Low Energy Electron Diffraction, AES = Auger Electron Spectroscopy, CMA = Cylindrical Mirror Analyzer.

The preparation chamber is equipped with the usual techniques for sample preparation and control, like ion-gun (fixed energy 800 eV), quadrupole mass analyzer, reverse-view LEED and AES with CMA (see for instance references [13, 18]). By a long travel manipulator, the sample can be transferred to the analysis chamber where RAIRS and STM experiments are performed. The two N_2-purged plexiglas chambers contain the infrared optics and are linked to the UHV chamber by KBr windows. The infrared beam leaving the spectrometer (Mattson Galaxy 6020) passes through a polarizer and is focused through one of the windows onto the sample at an angle of $85° \pm 1°$. The reflected IR-light leaves the UHV chamber through a second window and is collected by a mercury-cadmium-telluride detector. Both chambers can be separated by a gate valve in order to perform STM or RAIRS experiments under "real" pressure conditions (mbar range). By turning the crystal in a horizontal position, the beetle type STM (see § 2.1.2) can be positioned onto the sample holder. The holder is directly mounted to a liquid helium (or nitrogen) cryostat, allowing the crystal to be cooled down to

11

20 K. By means of electron bombardment it can be heated up to 1400 K. The temperature range for tunneling experiments, however, is currently restricted to 150 - 550 K, limited by vibrations due to the liquid helium flow and the piezo tube depolarization temperature. Evaporation of Si, Pd or Cu on well-prepared surfaces was achieved by electron bombardment heating. The evaporator displays continuously the measured ion flux which is directly proportional to the flux of evaporated atoms.

2.4. Sample preparation

The Pd(110) and Pd(100) crystals were oriented, cut by spark erosion and polished to the desired orientation to within 0.1°. They were cleaned by cycles of 800 eV Ar$^+$-ions sputtering at 300 K and 700 K, heating in a 10^{-6} mbar O_2 atmosphere and flash annealing at 900 K. Surface order and cleanliness was routinely verified by STM, LEED and AES.

Palladium is a transition metal with the fcc crystal structure. Its clean (110) face is unreconstructed and shows a rectangular unit cell with interatomic spacings of 2.75 Å and 3.89 Å as illustrated in figure 2.5 [19]. The surface consists of close-packed atom rows separated by channels in the [$\bar{1}$10] direction.
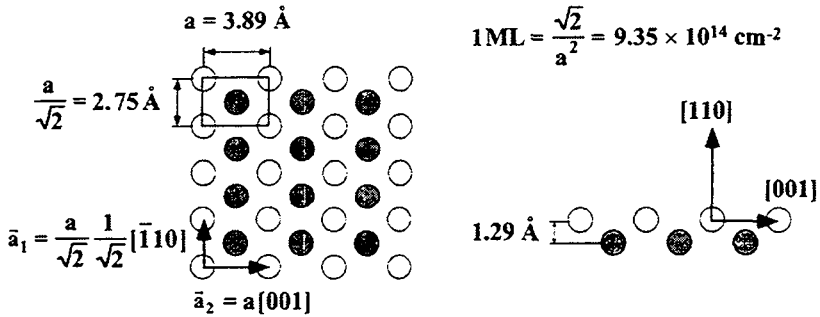

Fig. 2.5: Schematic top (left) and side (right) view of the Pd(110) surface. The white circles represent the topmost layer atoms, and the grey circles are the atoms in the second layer [19]. One monolayer (ML) is defined as the atomic areal density of the topmost layer.

The (100) face of the Pd is schematically represented in figure 2.6: its unit mesh is square of size 2.75 Å [19].
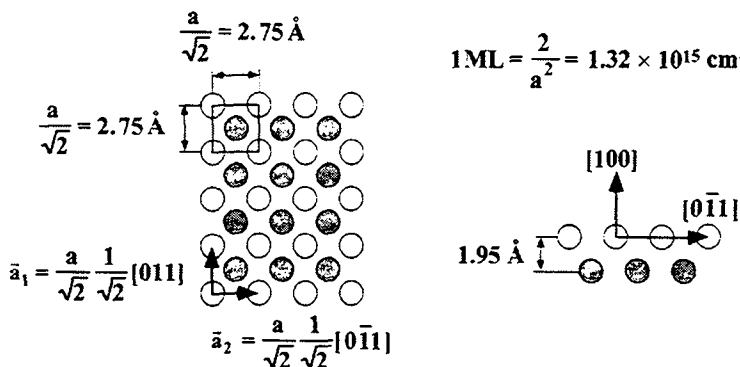
$$\frac{a}{\sqrt{2}} = 2.75 \text{ Å}$$

$$1 \text{ML} = \frac{2}{a^2} = 1.32 \times 10^{15} \text{ cm}^{-2}$$

$$\frac{a}{\sqrt{2}} = 2.75 \text{ Å}$$

[100]

[0$\bar{1}$1]

$$\vec{a}_1 = \frac{a}{\sqrt{2}} \frac{1}{\sqrt{2}} [011]$$

1.95 Å

$$\vec{a}_2 = \frac{a}{\sqrt{2}} \frac{1}{\sqrt{2}} [0\bar{1}1]$$

Fig. 2.6: Schematic top (left) and side (right) view of the Pd(100) surface. ML definition also indicated.

2.5. References

[1] G. Binnig and H. Rohrer, *Scanning tunneling microscopy*, Helv. Phys. Acta **55**, 726 (1982).

[2] G. Binnig, H. Rohrer, C. Gerber and E. Weibel, *Surface Studies by Scanning Tunneling Microscopy*, Phys. Rev. Lett. **49**, 57 (1982).

[3] K. Besocke, *AN EASY OPERABLE SCANNING TUNNELING MICROSCOPE*, Surf. Sci. **181**, 145 (1987).

[4] J. Frohn, J. F. Wolf, K. Besocke and M. Teske, *Coarse tip distance adjustment and positioner for a scanning tunneling microscope*, Rev. Sci. Instrum. **60**, 1200 (1989).

[5] H. Röder, *Aufbau und Test einer UHV-Kombinationsapparatur: Rastertunnelmikroscopie und IR-Spektroskopie an Halbleiteroberflächen*, Diplomarbeit, Bonn (1991).

[6] R. G. Greenler, *Infrared Study of Adsorbed Molecules on Metal Surfaces by Reflection Techniques*, J. Chem. Phys. **44**, 310 (1966).

[7] B. E. Hayden, *Reflection Absorption Infrared Spectroscopy* in *Vibrational Spectroscopy of Molecules on Surfaces*, J. T. Yates and T. E. Madey, Plenum Press, New York and London (1985).

[8] P. R. Griffiths and J. A. deHaseth, *Fourier Transform Infrared Spectrometry*, Wiley, New York (1986).

[9] G. Blyholder, *Molecular Orbital View of Chemisorbed Carbon Monoxide*, J. Phys. Chem. **68**, 2772 (1964).

[10] K. M. Schindler, *et al.*, *Is the frequency of the internal mode of an adsorbed diatomic molecule a reliable guide to its local adsorption site?*, J. El. Spec. Rel. Phen. **64/65**, 75 (1993).

[11] B. N. J. Persson and R. Ryberg, *Vibrational interaction between molecules adsorbed on a metal surface: The dipole-dipole interaction*, Phys. Rev. B **24**, 6954 (1981).

[12] P. Hollins, *The influence of surface defects on the infrared spectra of adsorbed species*, Surf. Sci. Rep. **16**, 51 (1992).

[13] G. Ertl and J. Küppers, *Low Energy Electrons and Surface Chemistry*, VCH, Weinheim (1985).

[14] E. Hahn, *STRUCTURE AND REACTIVITY OF VICINAL Pt AND LOW-INDEX Cu/Pd SURFACES*, THESE N° 1218, EPFL (1994).

[15] E. Hahn, E. Kampshoff and K. Kern, *Surface stress effects in chemical activation*, Chem. Phys. Lett. **223**, 347 (1994).

[16] J. A. Rodriguez, C. M. Truong and D. W. Goodman, *Infrared vibrational studies of CO adsorption on Cu/Pt(111) and CuPt(111) surfaces*, J. Chem. Phys. **96**, 7814 (1992).

[17] E. Hahn, A. Fricke, H. Röder and K. Kern, *Structure and complete chemical passivation of Pt(997)*, Surf. Sci. **297**, 19 (1993).
[18] D. P. Woodruff and T. A. Delchar, *Modern Techniques of Surface Science, Second Edition*, Cambridge University Press, Cambridge (1994).
[19] J. M. MacLaren, J. B. Pendry, P. J. Rous, D. K. Saldin, G. A. Somorjai, M. A. Van Hove and D. D. Vvedensky, *Surface Crystallographic Information Service. A handbook of Surface Structures*, D. Reidel Publishing Company, Dordrecht (1987).

3. Diffusion, nucleation and growth of Pd on Pd(110)

3.1. Introduction

The thermodynamic approach of epitaxial growth is based on the idea that surface free energy must be minimized. It predicts the well known three growth modes: layer or Frank - van der Merwe (FM), island or Volmer - Weber (VW) and layer plus island or Stranski - Krastanov (SK) growth. Provided that the deposit does not alloy with the substrate, the modes can be undestood in terms of the relative surface energies of the deposited film (γ_{fn}), substrate materials (γ_s) and interface (γ_{in}), where n refers to the number of layers. One obtains the FM mode if the condition $\gamma_{fn} + \gamma_{in} \leq \gamma_s$ is fulfilled independant of n. γ_{in} contains the n-dependant strain energy in the film caused by the structural misfit between adlayer and substrate. If the strain energy increases with n the FM mode is no longer valid and SK growth occurs. If the FM condition is not fulfilled even for $n = 1$, three-dimensional islands grow from the very beginning (VW mode). In many experiments, however, metastable structures that reflect kinetic limitations are the rule. Far from equilibrium, novel structures can be created by controlling the symmetry of the substrate, the temperature, the deposition rate and the atom composition of the substrate-adlayer system.

In this respect, the Pd/Pd(110) system is an interesting example in which anisotropic growth mechanisms are expected, similar to the Cu/Pd(110) system. This one was already studied by STM [1, 2]. Mean field nucleation theory [3-5] (see § 3.2), in particular the variation of saturation island density with temperature and deposition rate, have been used to study quantitatively Cu adatom diffusion on Pd(110). It was found that below 300 K, due to anisotropic diffusion, the adatoms move exclusively along the [$\bar{1}$10] direction and one-dimensional Cu chains are formed. A power law dependence in island density versus deposition rate of 1/4 (using the reasonable assumption that the critical nucleus $i = 1$) yields a characteristic energy for surface diffusion along [$\bar{1}$10] of (0.51 ± 0.05) eV. In the present work the exponent of 1/4 has experimentally been verified for Cu/Pd(110). At higher temperature ($T \geq 300$ K) adatom diffusion in the [001] direction is also activated and two-dimensional islands start to grow. From the initial slope of island density for $T \geq 300$ K and

from an analysis of island aspect ratio based on anisotropic diffusion, a value of (0.75 ± 0.07) eV was inferred for the energy barrier in the [001] direction.

To my knowledge the above mentioned article by J. P. Bucher et al. [1] is the only one published so far dealing with STM study providing a quantitative analysis of the diffusion barrier of metal adatoms on fcc(110) metal surfaces. There are however many other anisotropic metal-on-metal systems (like adatom diffusion on fcc(110), fcc(311) or bcc(211)) which have been studied by field ion microscopy (FIM) by measuring the mean-square displacement of the adatoms in a certain time interval [6]. This value shows an Arrhenius behavior, from which the activation energy for surface diffusion can be deduced (equations 3.2 and 3.3 in § 3.2). Also simulations have been made to predict the energy barriers for self-diffusion on fcc(110) surfaces [7]. A kinetic model developed by Y. Li et al. [8] allows an indirect determination of the energy barriers from the experimental data of Cu/Pd(110) [1] (see § 3.3.2.3). In table 1 we summarize some available data.

Systems	$E_{d,[\bar{1}10]}$ (eV)	$E_{d,[001]}$ (eV)	Methods	References
Cu/Pd(110)	0.51	0.75	STM, eq.3.10	[1]
Ni/Ni(110)	0.45	0.45	FIM	[6]
Pt/Pt(110)	0.79	0.78	FIM	[6]
Ni/Ni(110)	0.18	0.35	simulation	[7]
Pd/Pd(110)	0.30	0.33	simulation	[7]
Cu/Pd(110)	0.30	0.45	STM, model	[8]

Table 1: Energy barriers for adatom diffusion along the [$\bar{1}$10] and [001] directions of some fcc(110) surfaces. Based on STM measurements, two methods give the barriers for Cu/Pd(110): the equation 3.10 (§ 3.2) and the anisotropic corner-rounding model (§ 3.3.2.3).

3.2. Nucleation theory

The first part of this paragraph summarizes the nucleation theory [3-5] for the case of complete condensation and isotropic diffusion, which provides the saturation island density as a function of temperature, deposition rate and critical nucleus. It has proven to apply to the STM study of the nucleation of Ag on Pt(111) at low temperature [9]. In the second part, the result for the case of strongly anisotropic diffusion [10] will be briefly presented. We will

show here that it is valid in the case of Cu adatom diffusion on Pd(110). Its applicability to the Pd/Pd(110) system will be discussed.

All the individual atomic processes responsible for adsorption and crystal growth on surfaces are schematized in figure 3.1. The rate of arrival of atoms on the substrate $R[cm^{-2}s^{-1}]$ is controlled by an evaporation source. This creates single adatoms (density $n_1(t)$) on a substrate with N_0 sites per unit area. These single adatoms may then diffuse on the surface until they are lost by one of several processes which are governed by characteristic times (τ_x) depending on the substrate temperature (T). On a perfect surface, only three of the competitive processes shown in figure 3.1 are considered. The single adatoms may evaporate from the surface (τ_a), or they may alternatively start the nucleation chain (τ_n) of small clusters containing j atoms (density $n_j(t)$) up to the size j = i. It is called critical because clusters of size > i tend to grow rather than decay, whereas for j < i decay is more probable. When more adatoms encounter the critical clusters they form stable clusters (density $n_x(t) = \Sigma_{j \geq i+1} n_j(t)$). This opens up another channel for loss of individual adatoms, namely diffusive capture by stable clusters (τ_c). These three processes give rise to the following rate equation for the density of single adatoms:

$$\frac{dn_1}{dt} = R - \frac{n_1}{\tau_a} - \frac{n_1}{\tau_n} - \frac{n_1}{\tau_c} \tag{3.1}$$

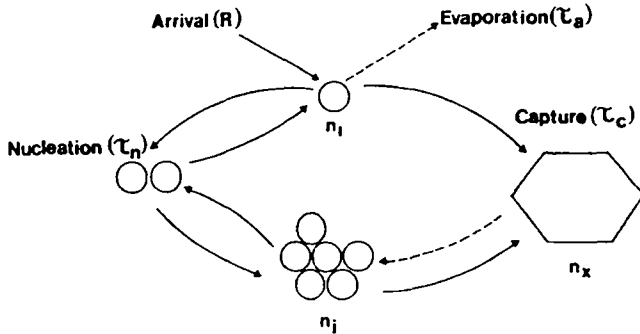*Fig. 3.1: Illustration of the interactions between different cluster populations in the early stage of film growth. The adatom density n_1 determines the density of the critical clusters n_i and of the stable nuclei n_x. n_1 is itself determined by the arrival rate R in conjunction with the various loss processes described in the text. The dotted lines indicate improbable processes in the case of layer growth [3].*

The complete condensation regime ($\tau_a = \infty$) applies to layer growth which occurs if the binding energy of adatoms to the substrate (adsorption energy E_a) is much larger than the binding energy between these adatoms (E_b). With increasing deposition time, the loss of adatoms during nucleation itself (τ_n) is negligible in comparison to the loss of adatoms to stable clusters which is related to τ_c in an atomistic description by $\tau_c^{-1} = \sigma_x Dn_x$. σ_x is a capture number (of order 5 - 10). D is the diffusion coefficient of single atoms defined by [6]:

$$D = \frac{\langle r^2 \rangle}{2m\Delta t} \tag{3.2}$$

where $\langle r^2 \rangle$ is the adatom average mean-square displacement during the time interval Δt and m the dimensionality of the diffusion (m = 1 or 2).

The above equation can be expressed as (if one considers only jumps to neighboring sites) [6]:

$$D = D_0 \exp\left(-\frac{E_d}{k_B T}\right) \quad \text{with} \quad D_0 = \frac{\nu_0}{2mN_0} \tag{3.3}$$

where ν_0 is an attempt frequency (order of magnitude of atomic vibrational frequencies 10^{12} s^{-1}), so $D_0 \sim 10^{-3}$ cm^{2}s^{-1} ($N_0 \sim 10^{15}$ cm^{-2}). In the above equation, E_d is the activation energy for single atoms to diffuse on the surface. With these considerations equation 3.1 reduces to:

$$\frac{dn_1}{dt} = R - \sigma_x Dn_1 n_x \tag{3.4}$$

If only single atoms are mobile on the surface, the rate equation for n_x is the following:

$$\frac{dn_x}{dt} = \sigma_i Dn_1 n_i - 2n_x \frac{R}{N_0} \tag{3.5}$$

The first term is the increase of density of stable islands due to capture of a single atom by a critical nucleus (capture number $\sigma_i = 2 - 4$), and the second represents its decrease due to coalescence.

In order to determine $n_x(R,T,i)$, we would have to resolve the coupled rate equations 3.4 and 3.5. Since nucleation usually occurs under steady-state conditions ($dn_1/dt = dn_x/dt = 0$) these equations simplify to:

$$n_1 = \frac{R}{\sigma_x Dn_x} \tag{3.6}$$

$$\frac{n_x}{N_0} = \frac{1}{2} \frac{\sigma_i Dn_i}{R} n_1 \tag{3.7}$$

Statistical mechanics allows to calculate the density of critical nuclei n_i in terms of the single atom density n_1 and the free energy of the critical cluster E_i. The following relation is useful to solve the problem:

$$\frac{n_i}{N_0} = C_i \left(\frac{n_1}{N_0} \right)^i \exp \left(\frac{E_i}{k_B T} \right) \qquad (C_i = 1 - 10)$$ (3.8)

We obtain $n_x(R,T,i)$ in the case of complete condensation by inserting equation 3.6 in 3.7 and 3.8, then equation 3.8 in 3.7 and finally equation 3.3 in 3.7. Equation 3.7 thus reduces to:

$$\frac{n_x}{N_0} \sim \left(\frac{R}{N_0 v_0} \right)^\chi \exp \left(\chi \frac{E_d + E_i / i}{k_B T} \right) \quad \text{with} \quad \chi = \frac{i}{i+2}$$ (3.9)

For i = 1, 2, 3, 4 the corresponding values of χ are 1/3, 1/2, 3/5, 2/3, respectively.

This formula applies in the case of isotropic diffusion. n_x is the island density at saturation and can be measured on STM images. T is the substrate temperature. R is the deposition rate. This equation relates external parameters like T and R and to the parameters governing the adatom diffusion: the migration barrier E_d, the critical cluster size i and free energy E_i.

J. W. Evans [10] developed a modified version of rate equations which allows a unified treatment of both isotropic and anisotropic diffusion. In his coupled rate equations, similar to those presented by J. A. Venables [5], he distinguishes two different capture times τ_c for isotropic and anisotropic diffusion according to random walk theory. For isotropic diffusion in the steady-state regime he recovers the result obtained above (equation 3.9). In contrast, for strongly anisotropic diffusion when $n_1 \ll n_x$ he gets equation 3.9 but with a different exponent:

$$\frac{n_x}{N_0} \sim \left(\frac{R}{N_0 v_0} \right)^\chi \exp \left(\chi \frac{E_d + E_i / i}{k_B T} \right) \quad \text{with} \quad \chi = \frac{i}{2i+2}$$ (3.10)

For i = 1, 2, 3, 4 the corresponding values of χ are 1/4, 1/3, 3/8, 2/5, respectively.

The power law dependence of n_x (R) allows to distinguish between isotropic (equation 3.9) and anisotropic diffusion (equation 3.10). Once χ has been determined in that way, the Arrhenius plot $n_x(1/T)$ provides the characteristic energy $(E_d + E_i / i)$. If i = 1 the plot yields directly E_d since $E_1 = 0$.

3.3. Nucleation and submonolayer growth of Pd on Pd(110)

In this paragraph, the experimental results concerning Pd diffusion and growth on Pd(110) in the submonolayer range will be presented. Once the calibration rate is determined, curves

of island density versus Pd coverage permit to find the saturation regime (§ 3.3.1). The dependence of the saturation island density (which is called now ρ) on temperature and deposition rate will be discussed. We will demonstrate that in contrast to the Cu/Pd(110) system [1, 2], Pd diffusion on Pd(110) cannot be suitably described by an anisotropic diffusion approach. A model developed by Y. Li and coworkers [8] explaining anisotropic island shape with isotropic diffusion and anisotropic bonding appears to be more appropriate to explain our data (§ 3.3.2). In § 3.3.3 a detailed analysis of the shape and the separation of the Pd adislands grown on Pd(110) will be presented.

3.3.1. Basic experimental observations

3.3.1.1. Calibration of the deposition rate

First of all, we have to calibrate accurately the deposition rate of our Pd evaporator. For this purpose, we perform the following experiment:

For a fixed value of the deposition rate (see § 2.3), Pd is deposited during 300 s on the Pd(110) surface held at 400 K. The STM image taken immediately after deposition is shown in figure 3.2. It reveals that the Pd adatoms have grown in lens shaped islands elongated along the [$\bar{1}$10] direction. The flux calibration has been achieved with a similar image, but in grey-scale height representation, by measuring the fraction of terraces covered by islands. This is justified because the growth of Pd adatoms on Pd(110) is pseudomorphic as revealed by a sharp (1 × 1) LEED pattern. So on figure 3.2 we measured a Pd coverage of 0.33 ML which gives an atomic flux of R = 1.1 × 10^{-3} ML/s.

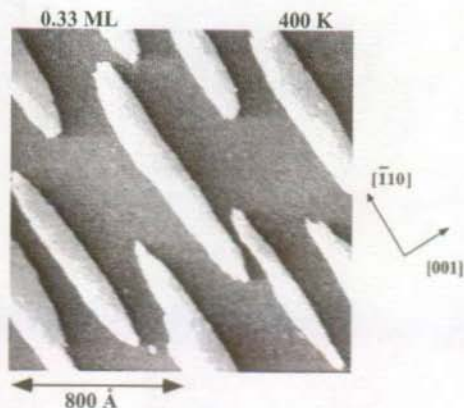**0.33 ML**   **400 K**

[$\bar{1}$10]

[001]

800 Å

Fig. 3.2: STM image (differential mode) showing lens shaped Pd islands elongated along the [$\bar{1}$10] direction. Pd atoms have been deposited during 300 s on the Pd(110) surface at 400 K.

3.3.1.2. Nucleation and saturation regimes

Our purpose is to determine the saturation density of adislands homoepitaxially grown on the (110) surface of Pd, because this density is the crucial parameter for the formulas derived from nucleation theory in § 3.2 (equations 3.9 and 3.10 have been calculated at saturation values of n_1 and n_x). In general, for a given deposition rate, the saturation island density is expected to depend on the temperature and the size of the critical nucleus. The temperature dependence is understandable because for higher temperatures, the adatom diffusion path is longer and consequently the island density reduces. The dependence on the critical nucleus i is even more significant because i determines directly the number of nucleation centers. So, for each temperature regime associated to a critical nucleus, a certain saturation density must be chosen.

Figure 3.3.a displays a series of STM images characterizing the growth of Pd on the Pd(110) surface at 250 and 300 K. They reveal chain-like Pd islands running along the [$\bar{1}$10] direction. This direction can be identified with added / missing rows induced by hydrogen on Pd(110) (see chapter 4). By measuring the total length of the pseudomorphic chains in each image and comparing it to the known number of deposited Pd atoms, we have a mean for evaluating their width. We found that at 250 K they are monoatomic in width for coverages less than 0.1 ML whereas at 300 K they are diatomic in width for coverages less than 0.2 ML. This result will be discussed later (§ 3.3.2.2).

The islands are counted as a function of coverage on STM images of 800 - 3200 Å in size at two different temperatures: 250 K and 300 K. The deposition rate is kept at R = 1.1 × 10^{-3} ML/s and the thermal drift is corrected. From inspection of figure 3.3, we distinguish two regimes: a nucleation regime characterized by a linear increase of the island density as a consequence of the creation of stable nuclei, followed by a growth regime during which adatoms are attached to the stable nuclei so that the density remains constant at its saturation value. At 300 K after depositing further adatoms (Θ > 0.2 ML), we observe the onset of coalescence. The density decreases because islands are starting to merge.

Figure 3.3 reveals that the saturation density is reached with a Pd coverage of about 0.1 ML at 250 K and about 0.2 ML at 300 K. In the following, we choose 0.1 ML of Pd in the
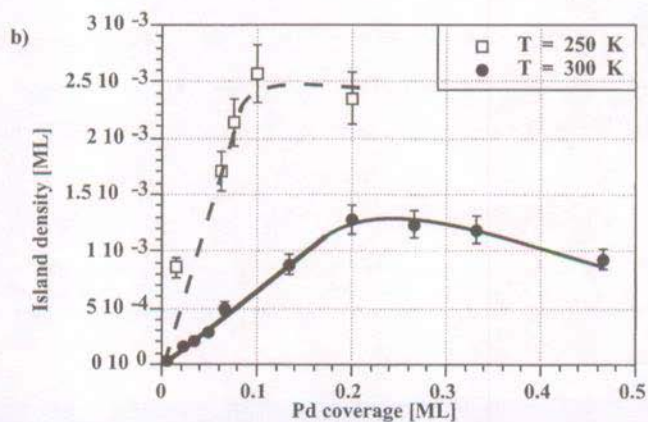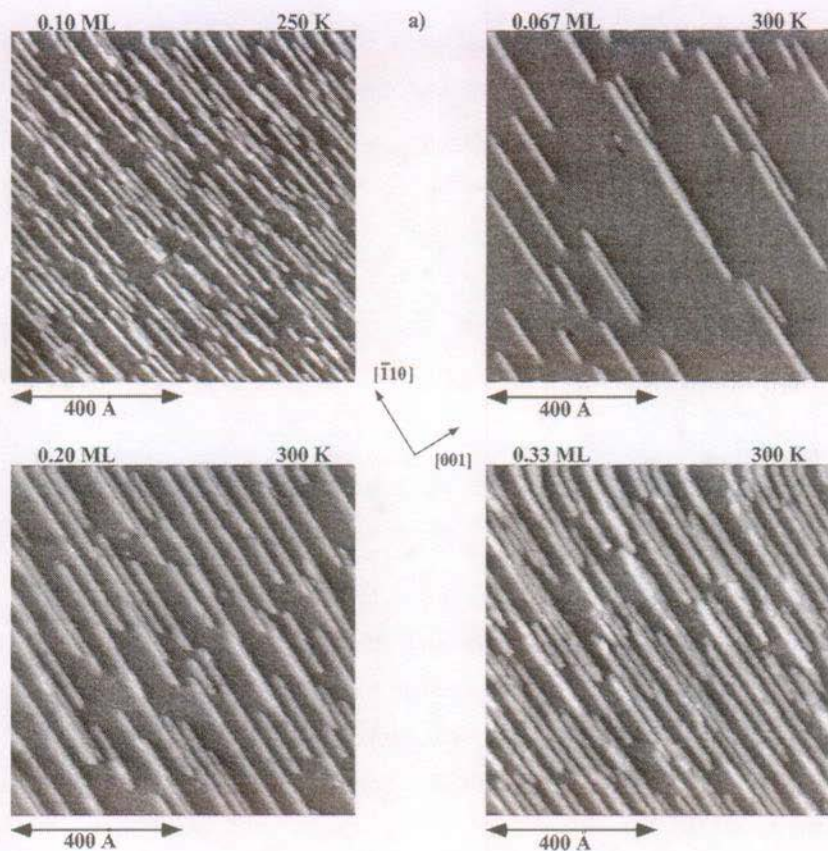
Fig. 3.3: a) STM images showing the surface morphology of Pd grown on Pd(110) at 250 and 300 K as a function of Pd coverage. b) Corresponding plot of the island density versus Pd coverage for substrate temperatures of 250 and 300 K.

temperature range 190 K ≤ T ≤ 290 K and 0.2 ML of Pd in 300 K ≤ T ≤ 400 K as corresponding to saturation densities. This choice is based on the fact that all islands are found to be monoatomic in width in the low temperature range and from 300 K they start to grow two-dimensionally. This will be discussed in more detail below.

3.3.2. Anisotropic versus isotropic diffusion

3.3.2.1. Temperature and flux dependence of the island density

In the first part of this paragraph, the deposition rate is fixed to R = 1.1 × 10^{-3} ML/s. We will focus on the dependence of the saturation island densities (overall and 1D along [001]) on temperature. In the second part, the flux dependence of the overall saturation density of islands will be presented. The measurements will be compared to the Cu/Pd(110) system [1, 2].

The two following quantities have been measured in STM images in the temperature range from 190 K to 400 K: the overall density of islands ρ (counted number of islands on large terraces of at least 800 Å in width divided by the surface area), and the average island length $\overline{L}$ resulting of a statistics on about 100 measured islands (error on $\overline{L}$ given by the standard error of the distribution $\sigma_\mu = \sigma / \sqrt{N}$; comments concerning island length distribution are given in § 3.3.3.2). Thermal drift corrections were performed in all measurements.

We are interested in measuring ρ because it can be directly related to theoretical equations (3.9 or 3.10 in § 3.2). Its dependence on the deposition rate reveals the diffusion type (isotropic or anisotropic) and from its temperature dependence, energy barriers for surface diffusion are inferred (detailed analysis presented in § 3.3.2.3).

In figure 3.4 we show a series of STM images of Pd deposited on Pd(110) at saturation coverage as a function of temperature. At all measured temperatures, Pd islands are elongated along the [$\overline{1}$10] direction and the average island length $\overline{L}$ is measured along this direction. $\overline{L}$ increases progressively with temperature while the average width stays constant up to 300 K and drastically increases at higher temperatures. The island density decreases with increasing temperature, i.e. the number of atoms per island increases.

In lower plot of figure 3.5 is shown the overall island density ρ measured from the STM images as a function of 1 / T (Arrhenius plot). The experimental points can be interpolated by
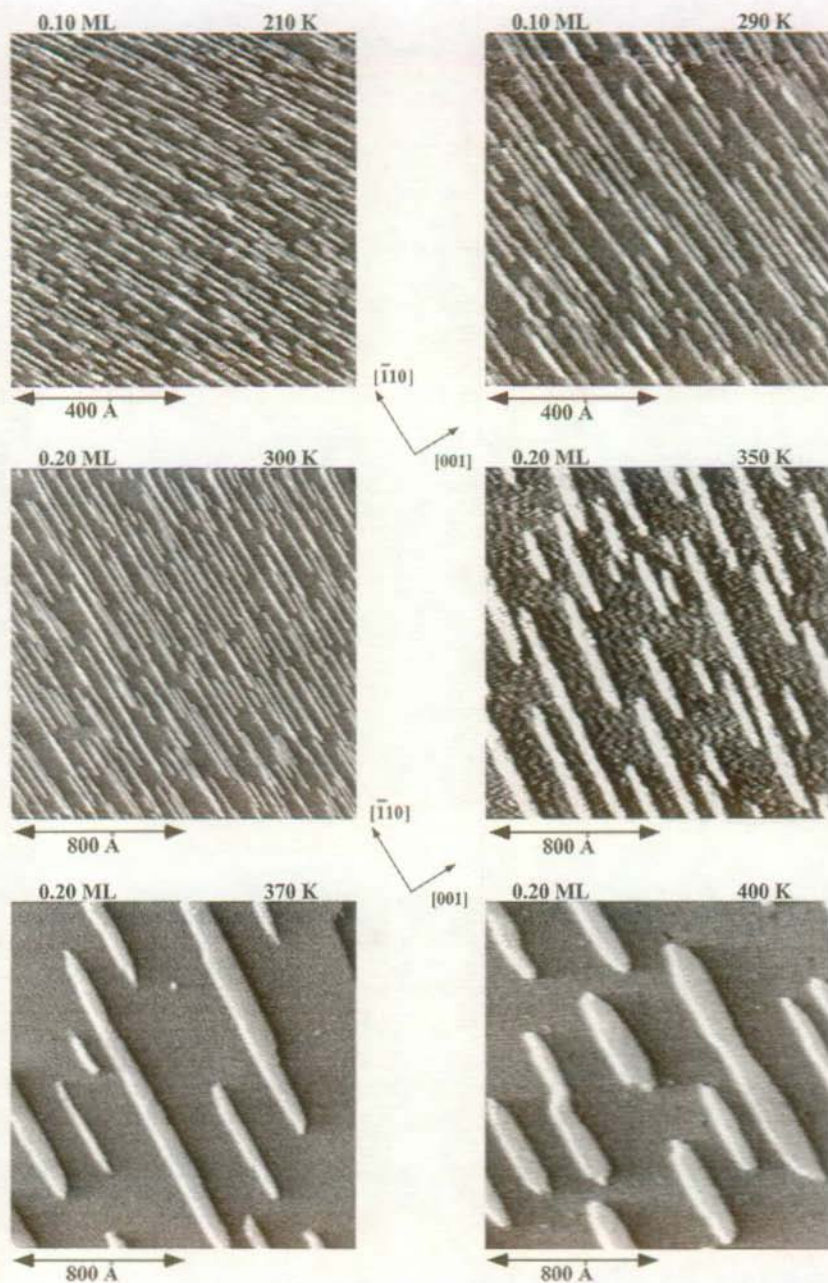
23

Fig. 3.4: STM images of Pd islands grown on Pd(110) at different temperatures at saturation density. Temperature and Pd coverage are indicated. This series is completed by the data shown in figures 3.6.a right-hand side (240 K) and 3.3.a (250 K).

two lines of quite different slopes revealing Arrhenius behavior and crossing at about 295 K. In the low temperature regime an exponential interpolation gives a slope of (0.048 ± 0.017) eV/k_BT, a value which is much smaller than the corresponding one obtained for Cu/Pd(110) of (0.13 ± 0.01) eV/k_BT [1, 2]. In the high temperature regime $(T \geq 300$ K) we obtain a slope of (0.39 ± 0.07) eV/k_BT for Pd/Pd(110).

From the measurements of ρ and $\overline{L}$ we can deduce the one-dimensional island density in the [001] direction in the case where islands are elongated in the [$\overline{1}$10] direction [8]:

$$\rho_{[001]} = \overline{L}\rho \tag{3.11}$$

The above formula comes from the fact that $\rho_{[\overline{1}10]} = \overline{L}^{-1}$ and $\rho = \rho_{[\overline{1}10]}\rho_{[001]}$. ρ is given in units of ML = $(a^2/\sqrt{2})^{-1}$, $\rho_{[\overline{1}10]}$ in $(a/\sqrt{2})^{-1}$ and $\rho_{[001]}$ in a^{-1}. $\rho_{[001]}$ is the number of islands per unit of lattice constant $a = 3.89$ Å in the [001] direction. Its measurement versus $1/T$ provides the island dimensionality and allows to find the critical temperature separating the 1D from the 2D growth regime.

From both measurements other important physical parameters can be inferred [8]:

- The average atom number per island:

$$\overline{N} = \frac{\Theta}{\rho} \tag{3.12}$$

Where Θ and ρ are expressed in ML.

- The average island width (in the [001] direction) expressed in atom number:

$$\overline{W} = \frac{\overline{N}}{\overline{L}} = \frac{\Theta}{\rho\overline{L}} \tag{3.13}$$

Where $\overline{L}$ is also dimensionless.

- The average island aspect ratio:

$$\overline{\alpha} = \frac{\overline{L}}{\overline{W}} = \frac{\rho\overline{L}^2}{\Theta} \tag{3.14}$$

Combining equations 3.11 and 3.13 we obtain a relation between the one-dimensional density $\rho_{[001]}$ and the average width $\overline{W}$:

$$\rho_{[001]} = \frac{\Theta}{\overline{W}} \tag{3.15}$$

Figure 3.5 displays in the upper plot the one-dimensional density in the [001] direction $\rho_{[001]}$ as calculated with equation 3.11 by multiplying $\overline{L}$ (figure 3.10 upper plot, in § 3.3.3.1) and ρ (figure 3.5 lower plot). Below 295 K it is found to stay approximately constant around

the value of 0.1 a^{-1}. Taking into account $\Theta_{Pd} = 0.1$, this value indicates that there are exclusively monoatomic chains parallel to the [$\bar{1}$10] direction (equation 3.15). At higher temperatures $\rho_{[001]}$ decreases rapidly with T; a slope of (0.31 ± 0.07) eV/k$_B$T is inferred from the Arrhenius plot; it is slightly larger than the one for Cu/Pd(110) of (0.19 ± 0.02) eV/k$_B$T [1, 2].
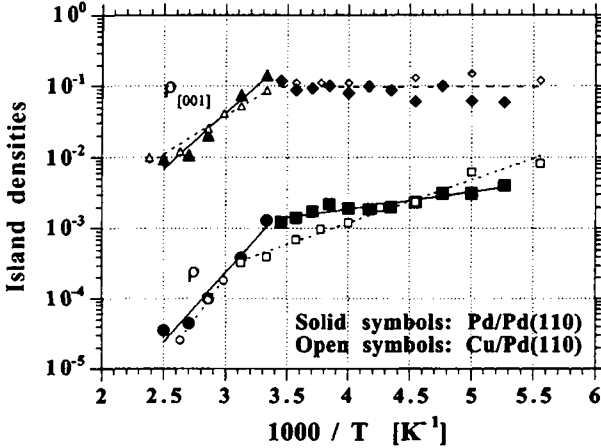

Fig. 3.5: Overall saturation density of islands ρ (lower plot) and one-dimensional density of islands in the [001] direction $\rho_{[001]}$ (upper plot) as a function of the reciprocal temperature (Arrhenius plots). Error bars are indicated by the size of the symbols. Units are: ρ in ML = $(a^2/\sqrt{2})^{-1}$ and $\rho_{[001]}$ in a^{-1}. The dashed horizontal line at $\rho_{[001]} = 0.1$ a^{-1} and low T is the value expected from equation 3.15 with $\overline{W} = 1a$ and $\Theta_{Pd} = 0.1$. Data of the Cu/Pd(110) system [1, 2] are included for comparison.

At this point, we come to the second part of this paragraph: the island density dependence on the deposition rate R. The used evaporator allows us to vary linearly the deposition rate in the range 10^{-5} ML/s < R < 10^{-2} ML/s.

In figure 3.6.a, two STM images are displayed. They show monoatomic Pd chains formed after deposition of 0.1 ML Pd on Pd(110) at 240 K at two different deposition rates. We notice immediately that a higher deposition rate leads to the formation of more and shorter adislands. The nucleation probability is obviously larger. The log-log plot displayed below (figure 3.6.b) represents the measured saturation island density as a function of deposition rate which has been varied over two orders of magnitude. We get a power law dependence

with an exponent of 0.39 ± 0.12. For comparison, the corresponding plot of Cu/Pd(110) at 280 K is shown on the same graph. It completes the results obtained by J.P. Bucher and coworkers [1, 2] and reveals an exponent of 0.19 ± 0.07. This value is compatible within errors to $\chi(i=1) = 1/4$ and confirms the anisotropic diffusion mechanism for Cu/Pd(110). The exponent obtained for Pd/Pd(110) suggests a different mechanism.
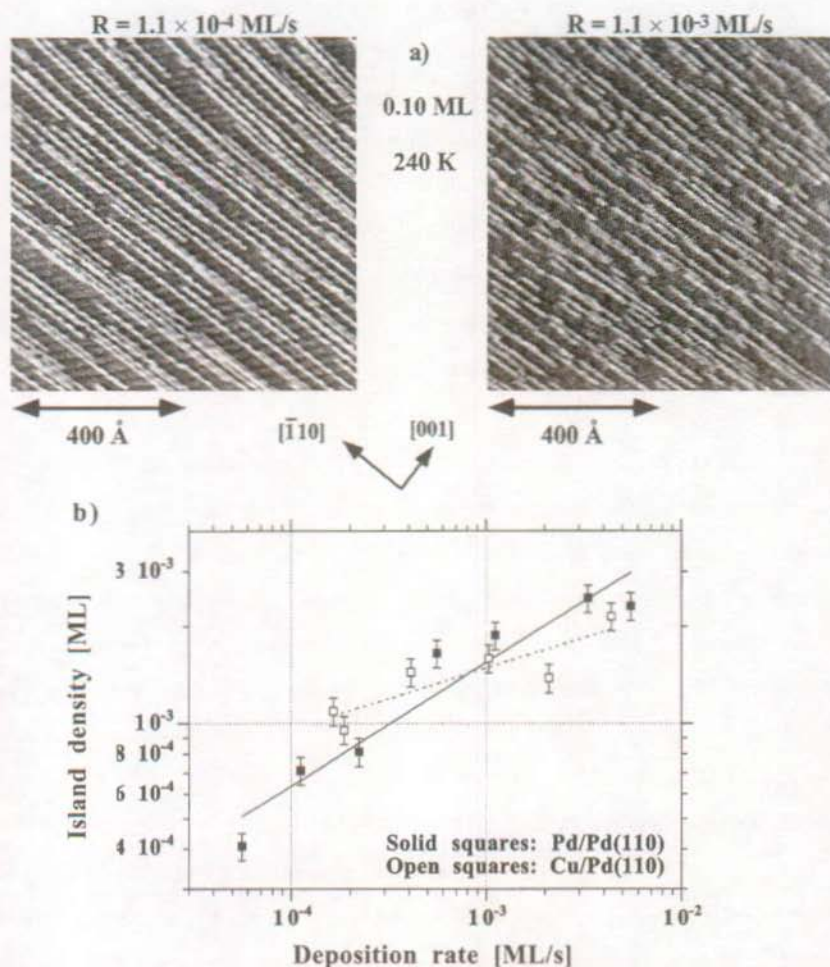

Fig. 3.6: a) Two STM images illustrating the effect of flux on the growth of Pd on Pd(110) at 240 K ($\Theta_{Pd} = 0.1$ ML). b) Corresponding Arrhenius plot of the island density as a function of the deposition rate compared with that obtained for Cu/Pd(110) at 280 K ($\Theta_{Cu} = 0.1$ ML).

3.3.2.2. Transition in critical nucleus

We found in § 3.3.2.1 that Pd adislands grown at $T \leq 290$ K are monoatomic in width and that 2D growth starts at 300 K. If the diffusion is not anisotropic, this suggests a change in the critical nucleus i occurring between 290 K and 300 K. We perform the following annealing experiment to determine the critical temperature T_c for which the low temperature critical nucleus which is assumed to be the dimer ($i = 1$) is no more stable:

0.1 ML Pd is deposited on the Pd(110) surface at 290 K as shown on the left-hand side of figure 3.7.a. From the STM data, the island density ρ is counted and a statistics on island length is performed to determine $\overline{L}$. The island density in the [001] direction is calculated with equation 3.11 ($\rho_{[001]} = \overline{L}\rho$) and the expected value is calculated with equation 3.15 ($\rho_{[001]} = \Theta / \overline{W}$) for monoatomic wires ($\overline{W} = 1a$). These data are displayed under the corresponding STM image (see figure 3.7.b on the left-hand side). Then the sample is annealed to 297 K and the same area is scanned immediately afterwards (figure 3.7.a, right-hand side). The same measurements are made and the corresponding data are displayed below (figure 3.7.b, right-hand side).

The analysis displayed in figure 3.7.b shows that after annealing the island density is reduced by a factor of two, the average length of the adisland remains constant, and consequently the average island density in the [001] direction is reduced by a factor of two (equation 3.11). Furthermore the experimental data for $\rho_{[001]}$ are within error bars compatible with equation 3.15 if the average width passes from one to two atoms. Taking simply the reciprocal value of the island density in the [001] direction, we obtain the average island separation before ($\rho_{[001]}(290 \text{ K})^{-1} \approx 10 \text{ a}$) and the doubled value after annealing ($\rho_{[001]}(297 \text{ K})^{-1} \approx 20 \text{ a}$).

The above analysis leads us to the following interpretation: At $T = 290$ K, the 0.1 ML Pd atoms evaporated on the Pd(110) surface nucleate from a critical cluster $i = 1$ in monoatomic chains parallel to the [$\bar{1}$10] direction. At the annealing temperature of 297 K, the 1D chains dissociate because beginning with this temperature, the dimer is no longer stable. Isotropic diffusion (confirmation in § 3.3.2.3) of individual adatoms occurs on the surface until four of them meet to create a stable cluster: the tetramer (critical nucleus $i = 3$) formed of two

28

neighboring pairs of atoms along the $[\bar{1}10]$ direction. These nuclei will further grow by binding other adatoms and finally form diatomic linear chains of same average length separated by a distance twice as large with respect to the configuration before annealing.

0.10 ML   deposited at 290 K   a)   **0.10 ML   annealed to 297 K**

← 400 Å → $[\bar{1}10]$ ← 400 Å →

$[001]$

b)

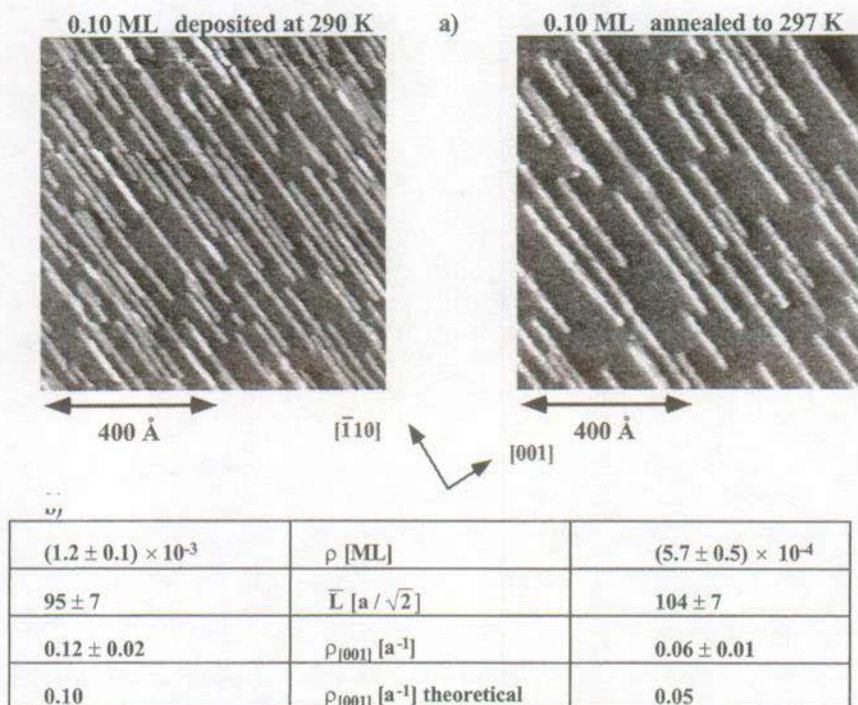| $(1.2 \pm 0.1) \times 10^{-3}$	ρ [ML]	$(5.7 \pm 0.5) \times 10^{-4}$
95 ± 7	$\bar{L}$ [$a/\sqrt{2}$]	104 ± 7
0.12 ± 0.02	$\rho_{[001]}$ [a^{-1}]	0.06 ± 0.01
0.10	$\rho_{[001]}$ [a^{-1}] theoretical	0.05

Fig. 3.7: a) STM images showing Pd adislands grown after deposition of 0.1 ML Pd on Pd(110) at 290 K (left) and after annealing to 297 K (right). b) Corresponding experimental values for ρ, $\bar{L}$ and $\rho_{[001]}$ (equation 3.11) and calculated theoretical values of $\rho_{[001]}$ using equation 3.15 with $\bar{W}(290\ K) = 1a$ and $\bar{W}(297\ K) = 2a$.

We exclude the trimer (i = 2) as being the stable nucleus at T ≥ 300 K since the energy necessary to remove one atom from the trimer is approximately the same as for the dimer; so the trimer will be unstable at T ≥ 300 K. The experimental evidence that all islands are diatomic in width at 297 K supports our conclusion that the tetramer is the stable nucleus.

The experimental temperature range is thus divided into two regimes: 1) 190 K - 290 K with i = 1 and 2) 300 K - 400 K with i = 3. The change in slope between these temperature ranges at $T_c \approx 295$ K is associated with a change in the critical nucleus size i.

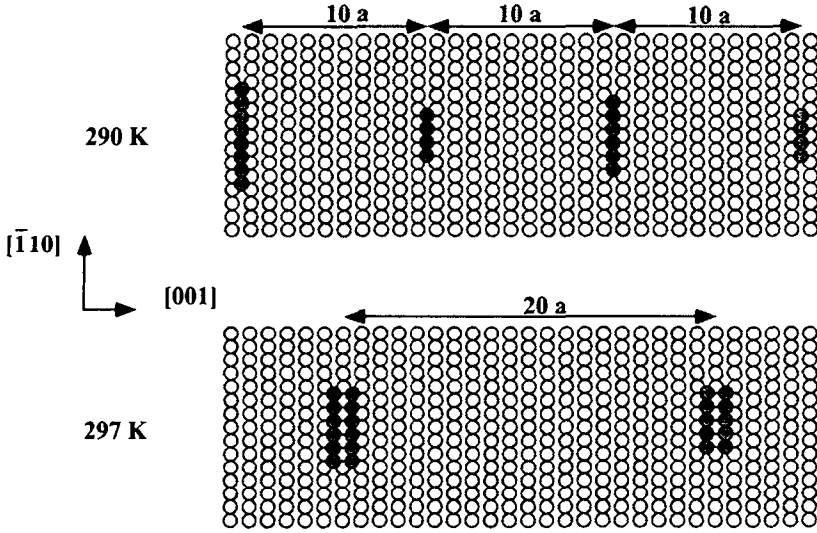Figure 3.8 summarizes the analysis discussed in this paragraph.

Fig. 3.8: Schematic ball model showing the transition of monoatomic to diatomic chains corresponding to the annealing experiment of figure 3.7.

3.3.2.3. Analysis of the diffusion mechanism

Our experiments reveal that Pd islands grown on Pd(110) exhibit anisotropic shapes at all temperatures studied.

The first intuitive idea to explain the anisotropically shaped islands (elongation along the [Ī10] direction) is anisotropic diffusion. In this case, two quite different energy barriers for surface diffusion along the [Ī10] and [001] directions govern the adatom diffusion ($E_{d,[\bar{1}10]} < E_{d,[001]}$). The Cu/Pd(110) system is very well explained by this model: at substrate temperatures below 300 K, the adatoms move exclusively along the [Ī10] direction forming 1D Cu chains. At higher temperatures, adatom diffusion in the [001] direction is activated and 2D islands start to grow [1, 2, 8].

For the Pd/Pd(110) system, the experimental χ value obtained for the power law dependence of the island density versus deposition rate of (0.39 ± 0.12) at 240 K is consistent within the error bars with all $\chi(i \geq 2) = 1/3, 3/8, 2/5, ...$ values calculated with equation 3.10 in

30

the case of strongly anisotropic diffusion. By applying equation 3.10 to the experimental island density ρ at $T \leq 290$ K (figure 3.5), we obtain:

$$E_{d,[\bar{1}10]} + \frac{(i-1)}{i} E_b = \frac{2i+2}{i}(0.048 \pm 0.017)\text{eV} \quad (i \geq 2) \tag{3.16}$$

In the above equation E_i has been replaced by $(i-1) E_b$, where $E_b = E_2$ is the binding energy between 2 atoms in the cluster $i = 2$. The equation 3.16 cannot be fulfilled with any values of $i \geq 2$ since we can estimate E_b from the cohesive bulk energy of 3.95 eV [6, 11] (in the fcc lattice, each atom has 6 nearest neighbors):

$$E_b \approx 3.95 \text{ eV} / 6 \approx 0.66 \text{ eV} \tag{3.17}$$

We conclude that anisotropic diffusion is not the main reason for the anisotropically shaped islands of Pd/Pd(110).

In contrast, Cu/Pd(110) was described by anisotropic diffusion [1, 2]. The experimental proof that this view is correct is presented in this work (figure 3.6.b, open squares): the island density power law dependence on deposition rate has a characteristic exponent of 0.19 ± 0.07 at $T = 280$ K. This value is only compatible with anisotropic diffusion with $i = 1$, $\chi = 1/4$. In the low temperature regime ($T \leq 280$ K), Cu atoms travel along the $[\bar{1}10]$ direction without any mobility in the [001] direction and the island formation is a true 1D problem leading to monoatomic chains. The 1D island density in [001] direction remains constant at the value corresponding to monoatomic chains $\rho_{[001]} = 0.1a^{-1}$ (figure 3.5, equation 3.15) and thus $\rho = 0.1a^{-1}\rho_{[\bar{1}10]}$. Applying equation 3.10 to the experimental data ρ (figure 3.5) yields ($E_1 = 0$): $E_{d,[\bar{1}10]} = (0.51 \pm 0.05)\text{eV}$. It is important to note here that the onset of diffusion in the transverse direction occurs before the critical nucleus changes at 320 K. Thus from $\rho_{[001]}$ (1/T) at $T \geq 300$ K (figure 3.5), the authors obtain using equation 3.10 with $\chi = 1/4$: $E_{d,[001]} = (0.75 \pm 0.07)$ eV [1, 2].

Within errors the experimental value of $\chi = 0.39 \pm 0.12$ for Pd adatom diffusion on Pd(110) is compatible with two values given by equation 3.9 in the case of isotropic diffusion: $\chi(i=1) = 1/3$, $\chi(i=2) = 1/2$. The case $i = 2$ is directly excluded for of the same reason as before (equation 3.17). This result suggests that the dimer is the stable nucleus for $T \leq 290$ K. Isotropic diffusion means that in this model both diffusion barriers are equal. We

apply equation 3.9 with $\chi(i=1) = 1/3$ to the experimental slope of $\rho(1/T)$ at $T \leq 290$ K of figure 3.5 and we obtain the barrier for diffusion:

$$E_d = (0.14 \pm 0.05)\,eV \tag{3.18}$$

At $T \geq 300$ K it is reasonable to assume $i = 3$ (as in § 3.3.2.2) which gives $\chi = 3/5$. From the island density along the [001] direction at $T \geq 300$ K in figure 3.5, we obtain with equation 3.9:

$$E_d + \frac{E_3}{3} = (0.65 \pm 0.12)\,eV \tag{3.19}$$

By inserting equation 3.18 in equation 3.19, we get a value for the binding energy of the critical cluster $i = 3$:

$$E_3 = (1.53 \pm 0.36)\,eV \tag{3.20}$$

This value is compatible with the estimation of E_3 obtained from the cohesive energy (equation 3.17):

$$E_3 = 2E_2 \approx 1.32\,eV \tag{3.21}$$

In general, anisotropic island shape is found on anisotropic substrates (made of parallel troughs). However they can be explained by two different mechanisms: either anisotropic diffusion or anisotropic sticking of monomers to exisiting islands, or both. A famous example of anisotropically shaped island was found in semiconductor epitaxy. For the Si/Si(100) system, island elongation was found to be perpendicular to the direction of fast diffusion (dimer rows), and has been interpreted as resulting from anisotropy in the sticking of monomers [12-14]. H. Metiu and coworkers questioned this interpretation and proposed an alternative model based on an exchange mechanism [15]. C. Pearson et al. however found in a recent paper [16] that the exchange mechanism that operates in some metal-on-metal systems, evoked by H. Metiu, does not affect the growth of Si islands on Si(100). The large sticking anisotropy overwhelms the diffusional anisotropy.

In the case of metal-on-metal fcc(110) epitaxy, Y. Li and coworkers [8] developed a new description for growth kinetics via Monte Carlo simulations which can explain anisotropy in the island shape without necessarily diffusional anisotropy. In summary this model is the following: They considered the atomistic processes on a (110) surface (E is the notation for the activation energies and x, y refer to [001] and [$\bar{1}$10] directions, respectively, see figure

3.9): random deposition at a rate R, terrace diffusion of isolated adatoms by hopping $E_{h,x} \geq E_{h,y}$, diffusion of edge atoms $E_{e,x} > E_{e,y}$ and movement of edge atoms to terrace sites at island corners $E_{c,x} > E_{c,y}$. Both last inequalities arise from weaker cross-trough bonding. They found that the relationship between the barriers for terrace diffusion ($E_{h,x}$, $E_{h,y}$) and edge diffusion ($E_{e,x}$, $E_{e,y}$) is not crucial for the island shape and density and set $E_{e,x} = E_{c,x} > E_{h,x}$ and $E_{e,y} = E_{c,y} > E_{h,y}$. They incorporated in the model the crucial anisotropic "corner-rounding" process: after detaching from one side of an island at a corner, the atom may re-attach to the other side. The net effect of this process is mass transport between two island edges. This transport is direction-dependent because of the inequality $E_{c,x} > E_{c,y}$. This process is found to be the kinetic mechanism responsible for the 1D-2D transition at the critical temperature T_c. These atomic processes, schematized in figure 3.9, allow to explain the general Arrhenius behavior of the overall island density (ρ) and the 1D island density along the [001] direction ($\rho_{[001]}$) displayed in figure 3.5. At $T < T_c$, $E_{c,x}$ is insurmountable. ρ is mainly determined by in-trough dimer formation ($i = 1$) and decreases with increasing T. Anisotropic corner rounding occurs, edge atoms being transported from the y- to the x-edge, but not in the inverse direction. Consequently the island average length ($\bar{L}$) increases with T and $\rho_{[001]}$ remains constant because of equation 3.11. At $T > T_c$, $E_{c,x}$ is surmountable. Because the critical cluster size exceeds one ($i > 1$), the Arrhenius slope of ρ increases. Two way corner-rounding occurs such that the islands grow two-dimensionally and $\rho_{[001]}$ decreases. The authors showed that T_c (onset temperature for growth in x direction) depends strongly on the degree of anisotropy in the corner-rounding ($E_{c,x} / E_{c,y}$) but is insensitive to anisotropy in terrace diffusion ($E_{h,x} / E_{h,y}$). The only way to fit the experimental data of Cu/Pd(110) [1, 2] $\rho_{[001]}(1/T)$, $\rho(1/T)$ and $\rho(R)$ (open symbols in figures 3.5 and 3.6) with this model was nevertheless to admit anisotropic diffusion (because of $\chi \approx 1/4$). The activation energies obtained (0.30 eV and 0.45 eV) are less anisotropic than those found using equation 3.10 with $i = 1$ in the anisotropic diffusion case (0.51 eV and 0.75 eV). These data are listed in table 1 (§ 3.1) in comparison with other data for migration barriers on (110) surfaces.

At the present time, this model is being applied to our data of Pd/Pd(110) in the purpose of determing in another way the migration barriers.
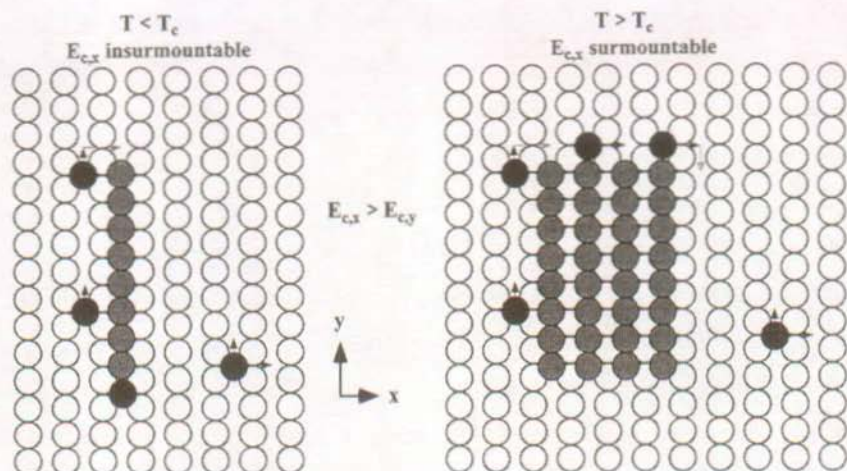
Fig. 3.9: Y. Li and coworkers' model [8]. White balls represent the atoms of a fcc(110) metal substrate, grey balls refer to metal adatoms incorporated in adislands and black balls to newly deposited adatoms. Atomistic processes considered on fcc(110) surface during submonolayer epitaxy are indicated by black arrows. The movement of edge atoms from island corners to terrace sites is governed by barriers $E_{c,x} > E_{c,y}$. Grey arrows indicate anisotropic corner-rounding processes.

It is worth comparing our results to related systems: J. W. Evans and coworkers [17] had to assume a value of i = 1 for self-diffusion of Pd adatoms on Pd(100) at 300 K to be consistent with the diffusion energy they found: (0.56 ± 0.04) eV. The diffusion barrier determined for Pd/Pd(110) (equation 3.18) seems rather small compared to this value. Also most values obtained by FIM for single atom diffusion on fcc(110) metal in the [$\bar{1}$10] direction are much larger than E_d of equation 3.18: 0.45 eV for Ni/Ni(110), 0.79 eV for Pt/Pt(110) (see table 1 in § 3.1). In contrast, simulations of L. S. Perkins and coworkers [7] dealing with self-diffusion on fcc(110) surfaces predict much smaller energy barriers, comparable to the value given by equation 3.18: 0.18 eV and 0.35 eV for Ni, 0.30 eV and 0.33 eV for Pd, for diffusion in the [$\bar{1}$10] and [001] directions, respectively (table 1). According to our experimental results, these simulations indicate that Pd adatom diffusion on Pd(110) is almost isotropic. The authors found that in-channel diffusion occurs via hopping, cross-channel via exchange.

3.3.3. Island shape and separation

3.3.3.1. Aspect ratio

Figure 3.10 represents Arrhenius plots of the average island length $\bar{L}$ determined from STM data and the average island width $\bar{W}$ calculated using equation 3.13 (or 3.15). Note that $\bar{L}(1/T)$ increases monotonically with T in the whole temperature range whereas $\bar{W}(1/T)$ remains constant around one atom width for $T < T_c \approx 295$ K and increases 4 times faster than $\bar{L}$ for $T > T_c$, where 2D growth sets in. These findings are explainable in the frame of the Li model with isotropic diffusion (§ 3.3.2.3).
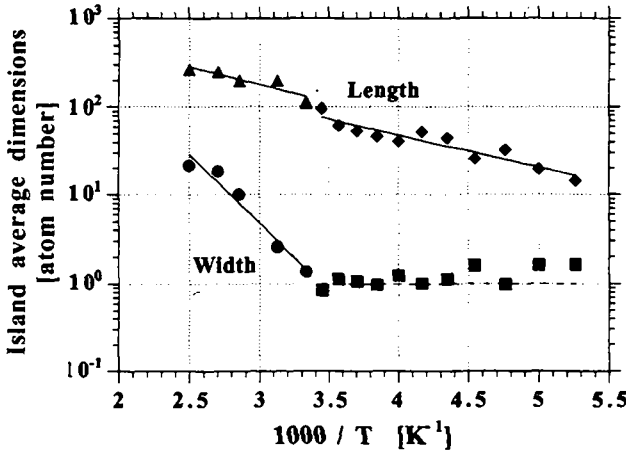

Fig. 3.10: Island average length ($\bar{L}$) and average width ($\bar{W}$) as a function of the reciprocal temperature. Dimensions are given in atom number (or equivalently in units of $a/\sqrt{2}$ for $\bar{L}$ and a for $\bar{W}$). Error bars on dimensions correspond to symbol size. The dashed horizontal line at $\bar{W} = 1$ indicates monoatomic chains. ($\Theta_{Pd} = 0.1$ ML in the low and 0.2 ML in the high temperature range.)

Using equation 3.14, the average island aspect ratio $\bar{\alpha}$ has been evaluated. Figure 3.11 shows the corresponding Arrhenius plot. At low temperatures ($T < T_c$) adatoms grow 1D as monoatomic chains and $\bar{\alpha} \approx \bar{L}$. $\bar{\alpha}$ increases with temperature until 2D growth sets in at $T_c \approx$ 295 K. The maximum value is found at 290 K ($\bar{\alpha} \approx 100$). At $T > T_c$ the aspect ratio decreases with T because of the two ways corner-rounding; at 400 K, it comes back to its initial value of 190 K ($\bar{\alpha} \approx 10$). The Arrhenius slope in the high temperature regime gives: (0.23 ± 0.09)

eV/k_BT. For comparison, the plot for Cu/Pd(110) is shown in the same graph: at low temperatures its behavior is very similar, $\bar{\alpha} \approx \bar{L}$ increasing with T until its maximum value of $\bar{\alpha} \approx 50$ is reached at 265 K. For higher temperatures it decreases slower with a characteristic slope of (0.11 ± 0.01) eV/k_BT back to the its initial value. The fact that the Pd islands grown on Pd(110) exhibit a maximum aspect ratio twice as high is presumably related to the different mechanisms leading to the anisotropic shape: anisotropic diffusion for Cu/Pd(110) versus anisotropic binding for Pd/Pd(110) as discussed in § 3.3.2.3.
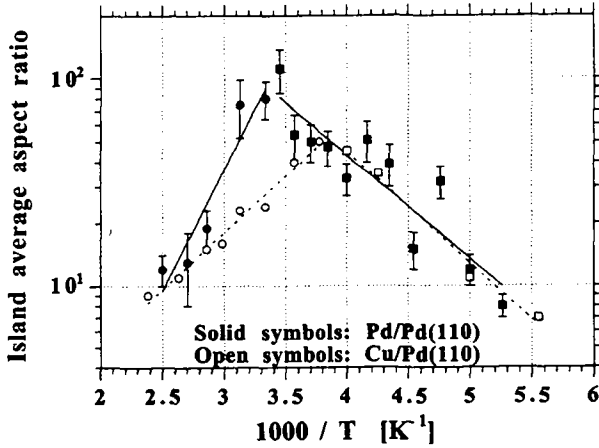

Fig. 3.11: Island average aspect ratio ($\bar{\alpha}$) as a function of the reciprocal temperature for the systems Pd/Pd(110) (from figure 3.10) and Cu/Pd(110) (from references [1, 2]).

To confirm the validity of our analysis concerning the diffusional isotropy, we apply the following formula for the mean aspect ratio to our result [1, 2]:

$$\ln \bar{\alpha} = \frac{E_{d,[001]} - E_{d,[\bar{1}10]}}{2k_BT} \quad \text{with} \quad T > T_c \tag{3.22}$$

This formula is applicable in case of anisotropic diffusion when the growth is 2D as for the Cu/Pd(110) system: $\Delta E_d = (0.22 \pm 0.02)$ eV/k_BT in accordance with results of § 3.3.2.3. In the case of Pd/Pd(110), one would obtain from equation 3.22:

$$\Delta E_d = E_{d,[001]} - E_{d,[\bar{1}10]} = (0.46 \pm 0.18)\,eV \tag{3.23}$$

This value is quite unrealistic when comparing it with experimental data for other metal-on-metal systems (see table 1 in § 3.1) and so the hypothesis of diffusional anisotropy fails again.

This result corroborates the proposed process for the origin of anisotropic island shape for Pd/Pd(110): anisotropic corner-rounding with isotropic diffusion as discussed in § 3.3.2.3.

3.3.3.2. Length distribution

As mentioned in § 3.3.2.1, a statistics on island length has been established at all studied temperatures (at saturation coverage) to determine the average length $\overline{L}$ (or mean μ) and the standard deviation of the distribution (σ). A few typical histograms and the plot of $\mu(\sigma)$ for the low temperature regime are displayed on figure 3.12. In this regime ($190\ K \leq T \leq 290\ K$) all Pd adislands are monoatomic chains oriented along the [$\bar{1}$10] direction. This figure shows that the Pd island length distribution is very wide and that $\mu \approx 1.6\sigma$.

As we have demonstrated in § 3.3.2.3, the growth mechanism is well described by isotropic diffusion. We assume that the Arrhenius plot of $\rho(1/T)$, in the range $190\ K \leq T \leq 290\ K$, is not affected by the the anisotropic binding but depends on isotropic diffusion barrier E_d only. So we can relate our results of island length distribution to the island size distribution simulated for submonolayer growth on a square lattice [18]. The authors found that the width of the island size distribution decreases with increasing critical nucleus i. For i = 1 the ratio of the full-width at half-maximum (Γ) to the mean (μ) is $\Gamma/\mu \approx 1.3$ and for i = 2 it reduces to $\Gamma/\mu \approx 0.9$. The value for i = 1 is close to our value for Pd/Pd(110), because $\mu \approx 1.6\sigma$ and $\Gamma = 2.35\sigma$ [19], we have $\Gamma/\mu \approx 1.5$. This finding strongly supports that the stable cluster is the dimer (i = 1) for the Pd/Pd(110) system for $190\ K \leq T \leq 290\ K$.

3.3.3.3. Lateral separation

We are now interested to study the distribution of the lateral separations in the [001] direction of the monoatomic Pd chains. For that purpose, we choose a deposition temperature of 250 K for which adislands are monoatomic in width (§ 3.3.3.1) and the saturation coverage of 0.2 ML just below coalescence (§ 3.3.1.2). The corresponding situation is shown on the STM image in figure 3.13.a. A simple visual inspection reveals that the chains are not statistically distributed but are separated with a most probable distance measured to 3a. The mean distance between monoatomic chains is estimated from the reciprocal value of the island density in the [001] direction: $\rho_{[001]}(250\ K)^{-1} = 5a$ (from equation 3.15 with $\Theta = 0.2$, $\overline{W} = 1a$).
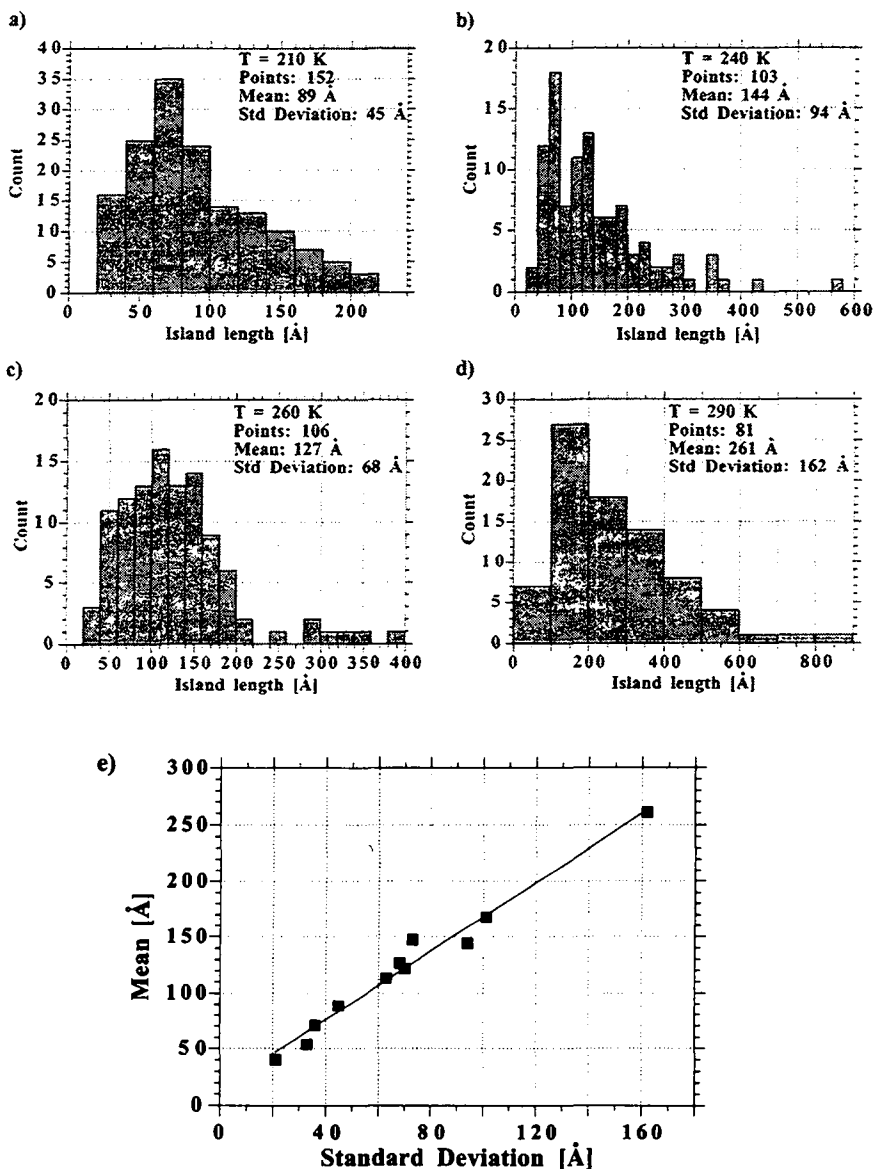
Fig. 3.12: a - d) Typical histograms for island lengths measurements of 0.1 ML Pd deposited on Pd(110) at 190 K ≤ T ≤ 290 K where islands are monoatomic chains (corresponding STM data in figure 3.4). e) Corresponding plot of the mean μ as a function of the standard deviation of the island length distribution σ.

To evaluate this in a more quantitative way, we measure the experimental probability of finding a chain at all integer distances n = x/a (x is the island separation in the [001] direction) from a certain chain. We proceed as follows: the STM image displayed in figure 3.13.a is divided in four equally sized areas which are zoomed by a factor of two to allow distinguishing island separations down to n = 1. The chain i = 1 in the bottom left corner of the image is selected. In the [001] direction the closest chain is found at a distance n. The orthogonal projection of this chain on the chain i is l_{ni}. The same procedure is applied for all the other chains separated from the selected chain i by p, q, r, ... $\geq$ n lattice constants. We then select the second chain i = 2 and repeat the same procedure. Finally the frequency of a given distance n is given by the sum over all the partial island lengths separated by a distance n: $\Sigma_i\, l_{ni}$. This frequency is normalized by the total island length $\Sigma_{i,n}\, l_{ni}$ to obtain the experimental probability P(n) of finding two chains separated by a distance of n lattice constants. The values of P(n) are displayed in figure 3.13.b as solid circles. The preferred distance separating two chains is 3. Knowing the form of P(n) it is easy to calculate the average separation between the chains:

$$\bar{n} = \Sigma_n\, nP(n) \approx 5 \qquad (3.24)$$

This value is consistent with the one calculated above with the help of equation 3.15.

Suppose the Pd chains are created upon one-dimensional diffusion of randomly deposited atoms, the probability $P_0(n)$ for the chain separation is given by a geometric law:

$$P_0(n) = \Theta\, (1 - \Theta)^{n-1} \qquad (3.25)$$

where Θ is the Pd coverage ($\Theta = 0.2$ in the present case). The points $P_0(n)$ are also shown for comparison on figure 3.13.b as open circles. The maximum of this curve is at n = 1 in total discrepancy with the experimental result of n = 3. Furthermore the short distances i = 1, 2 are less populated $P(i) < P_0(i)$, and longer distances j = 3 - 6 are more populated $P(j) > P_0(j)$ than expected from strictly one-dimensional diffusion.

This experimental island separation distribution agrees well with the isotropic diffusion mechanism associated with the anisotropic corner-rounding model found in § 3.3.2.3. An adatom landing on the surface diffuses randomly until it is captured by an existing island. Since $T < T_c \approx 295$ K, the adatom will be incorporated at the end of a monoatomic island

39

according to Li and coworkers' model (§3.3.2.3) as illustrated in figure 3.9 on the left-hand side. Within a certain distance, existing adislands act as sink for arriving adatoms. This means that there is a band on either side of each chain within which nucleation is depressed due to capture.

a)

0.20 ML   250 K

$[\bar{1}10]$ [001]

400 Å

b)
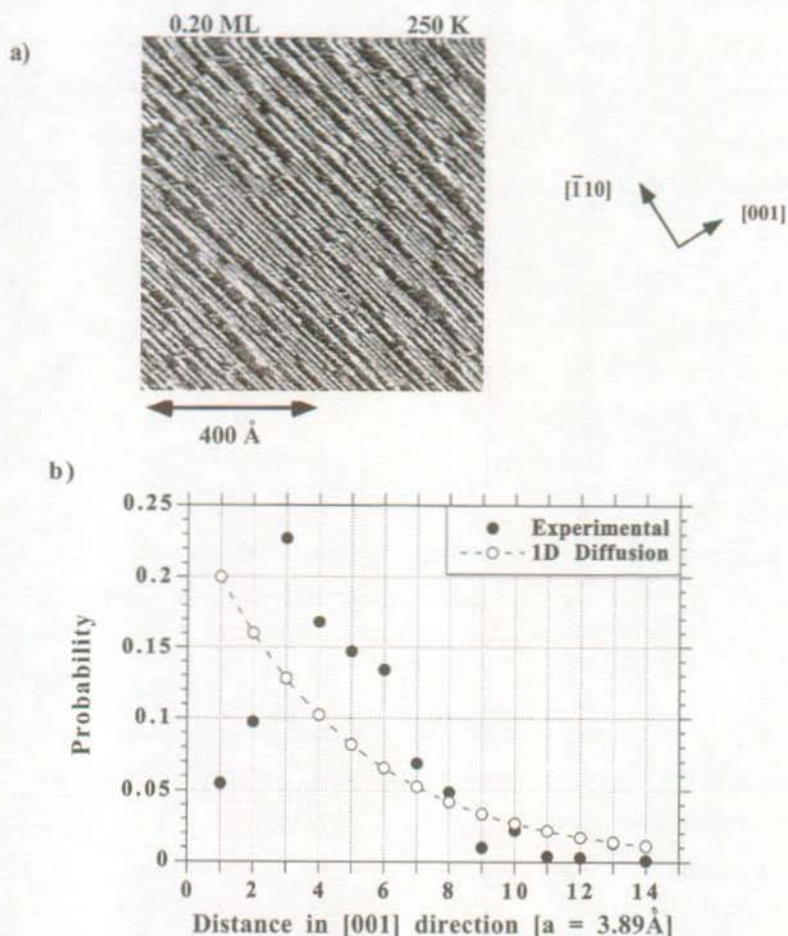

Fig. 3.13: a) STM image showing monoatomic Pd wires at saturation density close to coalescence ($\Theta_{Pd} = 0.2$ ML, $T = 250$ K). b) Experimental probability $P(n)$ of finding two monoatomic chains separated by a distance na in the [001] direction deduced from the image displayed above and calculated probability $P_0(n)$ for chains created after one-dimensional diffusion (equation 3.25).

This capture by existing islands is similar to the capture by atomic steps, where a "denuded zone" is created [3, 14]. By means of equation 3.2 the width of this band can be estimated. One considers that the adatom walks at random two-dimensionally during the time interval defined by the capture by an island $\tau_c = (\sigma_x D n_x)^{-1}$ with $\sigma_x = 5 - 10$ (§ 3.2, following equation 3.1). With equation 3.2 in the case of 2D random walk limited by island capture, one obtains:

$$\langle r^2 \rangle = \langle x^2 \rangle + \langle y^2 \rangle = 2\langle x^2 \rangle = 4D\tau_c \quad \Rightarrow \quad \langle x^2 \rangle = 2D\tau_c = 2(\sigma_x n_x)^{-1} \quad (3.26)$$

If we take the measured value of $n_x = 2.2 \times 10^{12}$ cm^{-2} of figure 3.3.b, we obtain a denuded zone of typically 9a. In fact by applying the above interpretation to our measurement, it predicts an average denuded zone somewhat smaller. Because an adatom can diffuse in [001] or [00$\bar{1}$], the average denuded zone is given by the half of the average island separation (equation 3.24): $W_{DZ} = 2a - 3a$. However, the calculation of equation 3.26 is only qualitative and merely the order of magnitude is of importance.

The denuded zone concept explains the discrepancy in figure 3.13.b between the experimentally determined distribution P(n) and the statistical distribution $P_0(n)$ expected by a 1D diffusion model. In the vicinity (n = 1, 2) of monoatomic chains, most of the diffusing adatoms are captured and incorporated to them. Pd adatoms walk at random over a certain distance limited by captures to existing islands. This long diffusion path causes larger island separations (n = 3 - 6).

The above interpretation confirms again our conclusion of § 3.3.2.3: adatom self-diffusion on Pd(110) is rather isotropic and the anisotropically shaped islands are a consequence of anisotropic corner-rounding processes.

3.4. Multilayer growth

The multilayer growth of Pd/Pd(110) at 300 K (at a fixed deposition rate of 1.1×10^{-3} ML s^{-1}) is illustrated by the data in figure 3.14.a. We notice that from 0.67 ML some atoms are found on the second layer (white points). At a coverage of 1.0 ML some very narrow holes, elongated in [$\bar{1}$10], are still present in the first layer. Their counterparts have nucleated on this first layer exactly in the same manner as in the initial stage of nucleation, also with diatomic width. By visually comparing these chains with the first two STM images of figure 3.3.a, we can estimate the coverage on the first Pd layer to about 0.05 ML. Thus the first layer

0.67 ML

1.0 ML

300 K

$[\bar{1}10]$

400 Å

[001]

400 Å

1.3 ML

2.0 ML

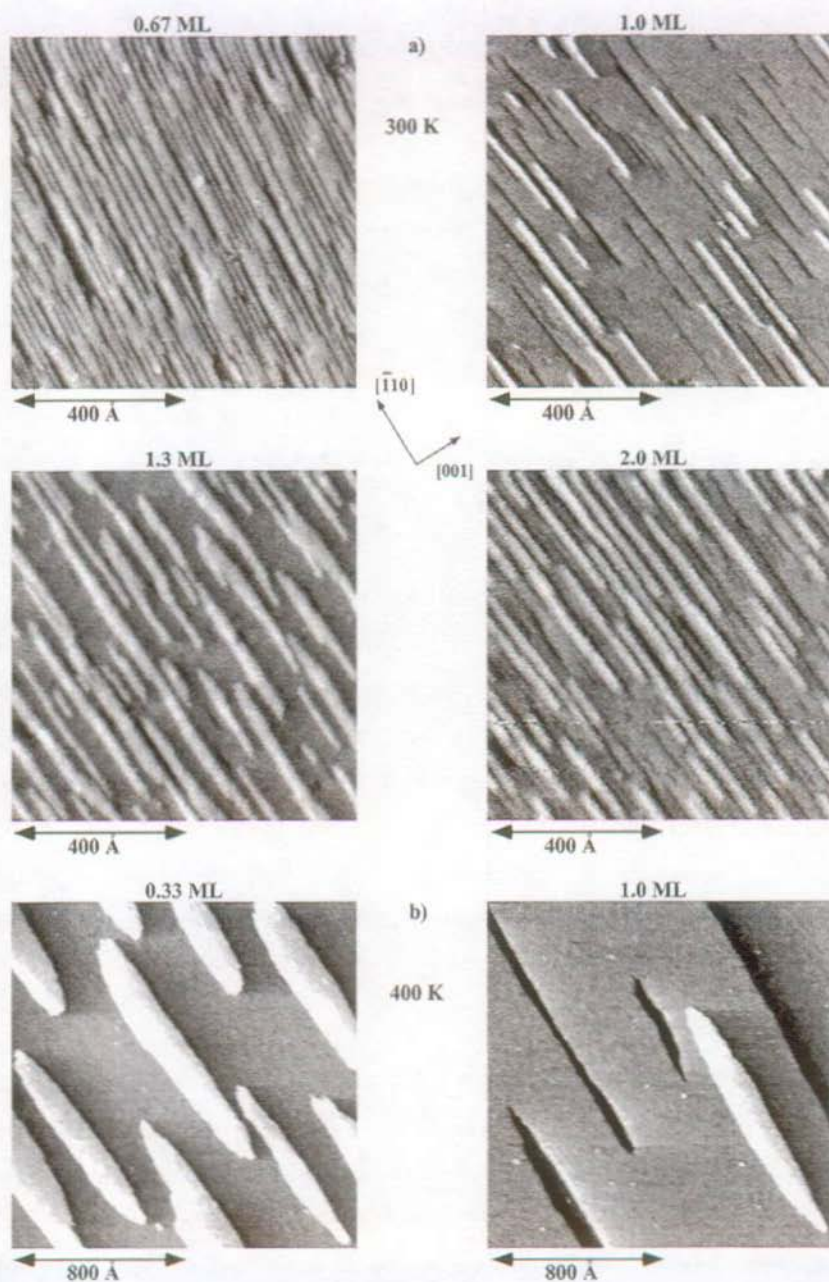400 Å

400 Å

0.33 ML

b)

1.0 ML

400 K

800 Å

800 Å

Fig. 3.14: STM images showing the multilayer growth of Pd on Pd(110) at 300 K (a) and at 400 K (b) at the indicated coverages.

42

is to about 95% completed. In the next image at 1.3 ML Pd coverage, the first layer is entirely completed and the 30% of the deposited Pd adatoms have again nucleated on the first layer like they would have done on the bare Pd(110) substrate (the islands formed are somewhat broader, compare with 0.33 ML in figure 3.3.a). If one deposits the equivalent quantity of 2.0 ML, the second layer is not completed and the proportion of atoms missing is larger than for the case of 1.0 ML. The islands of the third layer are even broader (diffusion on the first layer in [001] direction enhanced), longer and separated on each side by remaining holes in the second layer. About 3/4 of the second layer is filled and 0.25 ML Pd have nucleated on it (compare with the last two images of figure 3.3.a). The same growth mode has been observed up to 5 ML: a maximum of three levels are visible at a time. This growth mode is nearly layerwise. The interlayer mass transport is hardly hindered. Note that the growth at 300 K is strictly pseudomorphic, as expected, the LEED pattern remains (1 × 1).

At 400 K the growth mode is similar: we still don't find a perfect layer-by-layer growth. At 1.0 ML coverage, there are also holes in the first layer and Pd islands on top of it. Holes and adislands are lens shaped consitently with the form of the adislands grown on the Pd(110) substrate. At $T = 400$ K » $T_c \approx 295$ K, anisotropic effects are expected to be reduced and the island shape tends thus to be more symmetric.

The system Pd/Pd(110) exhibits a layerwise growth up to 5 ML at 300 K. For comparison, the Cu on Pd(110) growth mode at 300 K is exactly the same up to 0.7 ML. For coverages exceeding 1 ML, Cu layers are microrough consisting of small 3D clusters, due to the 7% misfit [20]. At 400 K an ideal three-dimensional Cu growth from the second layer on (Stranski - Krastanov growth mode) is inferred from the visible fraction of the n-th layer.

3.5. References

[1] J. P. Bucher, E. Hahn, P. Fernandez, C. Massobrio and K. Kern, *Transition from One- to Two-Dimensional Growth of Cu on Pd(110) Promoted by Cross-Exchange Migration*, Europhys. Lett. **27**, 473 (1994).
[2] E. Hahn, *STRUCTURE AND REACTIVITY OF VICINAL Pt AND LOW-INDEX Cu/Pd SURFACES*, THESE N° 1218, EPFL (1994).
[3] J. A. Venables, *Atomic processes in crystal growth*, Surf. Sci. **299/300**, 798 (1994).
[4] J. A. Venables, *Nucleation and growth processes in thin film formation*, J. Vac. Sci. Technol. B **4**, 870 (1986).
[5] J. A. Venables, G. D. T. Spiller and M. Hanbücken, *Nucleation and growth of thin films*, Rep. Prog. Phys. **47**, 399 (1984).
[6] G. L. Kellogg, *Field ion microscope studies of single-atom surface diffusion and cluster nucleation on metal surfaces*, Surf. Sci. Rep. **21**, 1 (1994).

[7] L. S. Perkins and A. E. DePristo, *Self-diffusion of adatoms on fcc(110) surfaces*, Surf. Sci. Lett. **317**, L1152 (1994).

[8] Y. Li, M. C. Bartelt, J. W. Evans and A. E. DePristo, *Transition from One- to Two-Dimensional Island Growth on Metal(110) Surfaces Induced by Anisotropic Corner Rounding*, **to be published**.

[9] H. Brune, H. Röder, C. Borragno and K. Kern, *Microscopic View of Nucleation on Surfaces*, Phys. Rev. Lett. **73**, 1955 (1994).

[10] J. W. Evans and M. C. Bartelt, *Nucleation and growth in metal-on-metal homoepitaxy: Rate equations, simulations and experiments*, J. Vac. Sci. Technol. A **12**, 1800 (1994).

[11] S. Günther, E. Kopatzki, M. C. Bartelt, J. W. Evans and R. J. Behm, *Anisotropy in Nucleation and Growth of Two-Dimensional Islands during Homoepitaxy on "Hex" Reconstructed Au(100)*, Phys. Rev. Lett. **73**, 553 (1994).

[12] Y. W. Mo, B. S. Swartzentruber, R. Kariotis, M. B. Webb and M. G. Lagally, *Growth an Equilibrium Structures in the Epitaxy of Si on Si(001)*, Phys. Rev. Lett. **63**, 2393 (1989).

[13] Y. W. Mo, J. Kleiner, M. B. Webb and M. G. Lagally, *Activation Energy for Surface Diffusion of Si on Si(001): A Scanning-Tunneling-Microscopy Study*, Phys. Rev. Lett. **66**, 1998 (1991).

[14] Y. W. Mo, J. Kleiner, M. B. Webb and M. G. Lagally, *Surface self-diffusion of Si on Si(100)*, Surf. Sci. **268**, 275 (1992).

[15] H. Metiu, Y. T. Lu and Z. Zhang, *Epitaxial Growth and the Art of Computer Simulations*, Science **255**, 1088 (1992).

[16] C. Pearson, M. Krueger and E. Ganz, *Direct Tests of Microscopic Growth Models using Hot Scanning Tunneling Microscopy Movies*, Phys. Rev. Lett. **76**, 2306 (1996).

[17] J. W. Evans, D. K. Flynn-Sanders and P. A. Thiel, *Surface self-diffusion barrier of Pd(100) from low-energy electron diffraction*, Surf. Sci. **298**, 378 (1993).

[18] J. G. Amar and F. Family, *Critical Cluster Size: Island Morphology and Size Distribution in Submonolayer Epitaxial Growth*, Phys. Rev. Lett. **74**, 2066 (1995).

[19] P. R. Bevington, *Data Reduction and Error Analysis for the Physical Sciences*, McGraw-Hill, New-York (1969).

[20] E. Hahn, E. Kampshoff, A. Fricke, J. P. Bucher and K. Kern, *Pseudomorphic growth of thin Cu films on Pd(110)*, Surf. Sci. **319**, 277 (1994).

4. Hydrogen-induced missing-row reconstructions of Pd(110)

4.1. Introduction

It is a well-known phenomenon that the interaction of adsorbates with a metal surface may lead to a complete restructuring of the surface with the number of discovered adsorbate-substrate systems undergoing this reconstruction process raising from year to year [1]. Molecules like sulfur, oxygen, carbon and nitrogen interact strongly with the substrate so that surface rearrangements in order to minimize the total surface free energy seem quite reasonable. Weakly chemisorbed species like hydrogen can also induce the restructuring if the surface has an inherent tendency towards reconstruction. Examples are the (110) surfaces of the 3d and 4d metals Ni and Pd. While the 5d homologue Pt has a missing-row reconstructed ground state, the unreconstructed (1×1) structure is more stable in the 3d and 4d metals. A small charge redistribution due to the chemisorption of hydrogen is however sufficient to induce a reconstruction of the Ni(110) and the Pd(110) surface [2-5]. In the temperature range between 120 K $\leq$ T $\leq$ 300 K two different kinds of (1×2) reconstructions have been found on both substrates, one low temperature pairing-row and a missing-row / added-row reconstruction.

In this chapter we will represent the results of our STM measurements on the system H/Pd(110). This system is of technical relevance as example for hydrogen storage due to its high solubility in the Pd bulk [6-10]. Different structures of the H/Pd(110) surface as a function of temperature and hydrogen coverage have already been examined [2, 3, 8]. In the low temperature regime below 200 K and in the submonolayer hydrogen coverage range the adsorbed gas can be described as disordered lattice gas. Ordering to a (2×1) superstructure sets in at $\Theta_H = 1$ ML, the saturation coverage of hydrogen on the unreconstructed Pd(110) surface. As schematized on figure 4.1.a, the hydrogen atoms form parallel zigzag chains along the close-packed metal rows; the adatoms occupy sites which are shifted from twofold towards almost threefold coordination. With increasing hydrogen exposure, the sharp (2×1) LEED pattern looses intensity in favor to a (1×2) superstructure which is most pronounced at $\Theta_H = 1.5$ ML. Its formation is shown in figure 4.1.b: After completion of the (2×1),

further hydrogen tends to adsorb onto the shifted twofold coordinate sites still available at the surface. The attraction of adjacent linear H chains perpendicular to the close-packed rows causes the pairing of the underlying metal rows (lateral shift of 0.2 - 0.4 Å) and build up the (1 × 2). In this way space is opened for the hydrogen atoms of the adjacent zigzag chain to move into on-top positions on the second metal layer (subsurface). Thus in the (1 × 2) phase there are two different types of chemisorption sites: 1 ML of H occupies the preferred twofold surface sites, whereas 0.5 ML occupies on-top sites in the second layer. At an annealing temperature of about 200 K these hydrogen atoms dissolve into the bulk, the (1 × 2) reconstruction gets lifted and the (2 × 1) superstructure reappears.
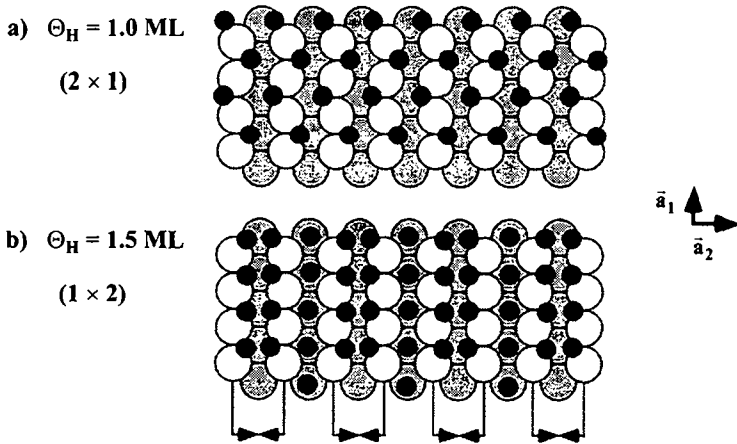

Fig. 4.1: a) Top view of hard-sphere model of the (2 × 1) phase of H on Pd(110). The large white (grey) circles denote Pd atoms of the first (second) layer and the black small circles H atoms. b) (1 × 2) phase of H on Pd(110). The pairing-row reconstruction indicated by arrows creates new adsorption sites of on-top position on the second (or subsurface) layer.

At room temperature another (1 × 2) superstructure is revealed which is assigned to a missing-row / added-row reconstruction of the surface related to hydrogen absorption into bulk [3]. Due to the fair amount of disorder along [001] the LEED pattern of this structure appears streaky. In contrast to the pairing-row, this reconstruction requires a substantial mass transport only possible at sufficiently high temperature. A model of the missing-row / added-row reconstruction is displayed on figure 4.2.
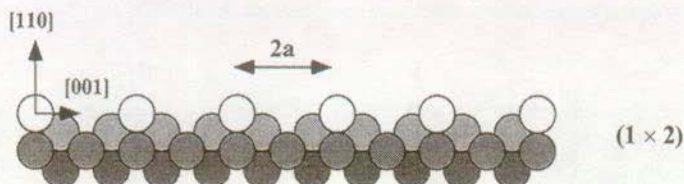
Fig. 4.2: Model of the (1 × 2) missing-row reconstruction. Every second [$\bar{1}$10] close-packed row within the top layer is missing (side view). Position of H not indicated.

We have observed by STM the existence of an additional (1 × 3) phase in the H/Pd(110) phase diagram at room temperature. (In fact this phase has already been observed by LEED [11].) At 300 K and hydrogen coverages between 0.3 ML ≤ Θ_H ≤ 0.5 ML, a (1 × 3) missing-row reconstruction has been found. Upon increasing the hydrogen coverage to 0.8 ML a coexistence regime with (1 × 3) and (1 × 2) phases is observed. The stability of these phases was checked by annealing experiments. At 350 K the Pd(110) surface is found to relax back into the stable (1 × 1) surface.

4.2. STM observations

The well-prepared Pd(110) surface (see § 2.4) was exposed to hydrogen at 300 K. By backfilling the chamber via a standard leak valve the partial pressure of hydrogen was fixed and in situ STM measurements were performed as a function of exposure time.

Figure 4.3 shows a series of STM images characterizing the morphology of the Pd(110) surface during the adsorption process of hydrogen at 300 K. The H_2 partial pressure was fixed to 2×10^{-9} mbar. The hydrogen uptake behavior of the Pd(110) surface can be separated into two regimes. In the first stage of hydrogen exposure, a kinetic equilibrium between the adsorption of hydrogen, its diffusion into the Pd bulk and the desorption will be established. The change in surface morphology during this stage is shown in the STM images in figure 4.3.a and b. The uppermost STM image was taken 45 minutes after starting the hydrogen exposure. As a result of hydrogen exposure we see the formation of holes in the Pd substrate as well as adatom islands on the terraces. Both, the adatom as well as the vacancy islands are elongated in the close-packed [$\bar{1}$10] direction of the substrate. The adisland shape nicely reflects the anisotropic growth of Pd on the Pd(110) surface (see chapter 3). With increasing

exposure the number of vacancy and adatom islands increases continuously as shown in figure 4.3.b.

a) 45 min   b) 95 min

400 Å $[\bar{1}10]$ [001]   400 Å

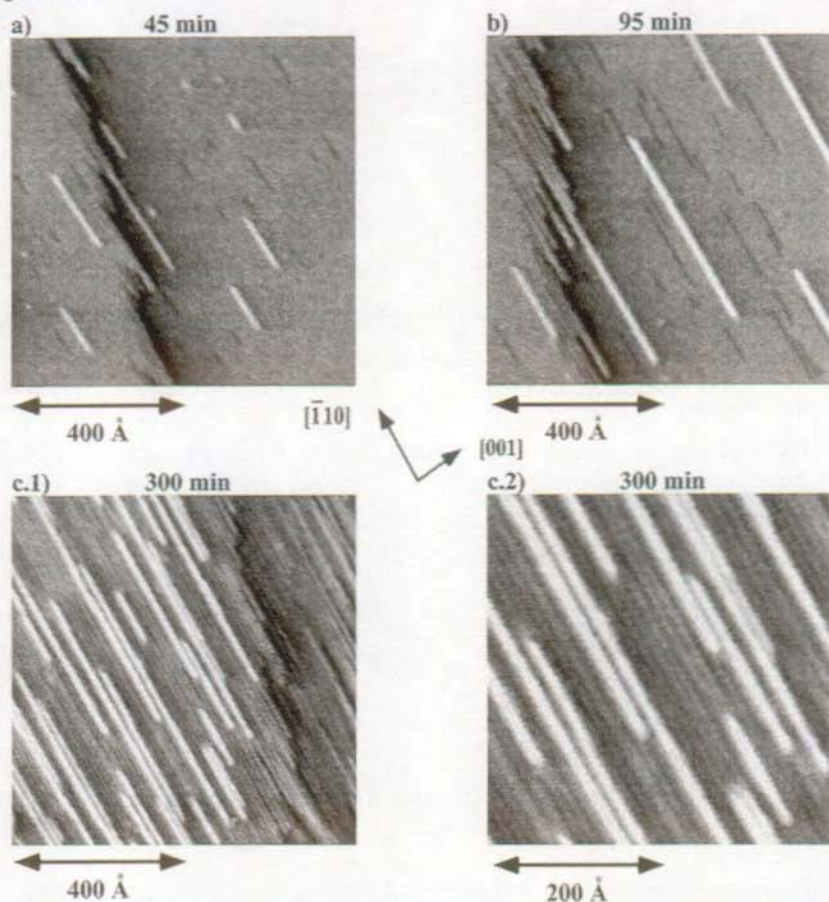c.1) 300 min   c.2) 300 min

400 Å   200 Å

Fig. 4.3: Morphology of the Pd(110) surface during hydrogen exposure. The STM images are taken after the indicated times of hydrogen exposure at 300 K with a fixed pressure of $p_{H_2} = 2 \times 10^{-9}$ mbar.

The height of the adislands and the depth of the vacancy islands correspond to the height of a monoatomic Pd(110) step. It is thus natural to conclude that the adislands have nucleated from Pd adatoms which have been kicked out of the surface. The vacancy islands on the other hand are the result of a nucleation and growth process of the corresponding monovacancies. Surprisingly the total length of vacancy and adislands on large terraces differs by a factor of

two, i.e. the total hole length is twice as large as the adisland length. This result implies that the Pd vacancy islands are monoatomic in width whereas the adislands consist of Pd dimer chains. Our experiments of homoepitaxial Pd/Pd(110) growth confirm this result (see chapter 3). At a deposition temperature of 300 K, the shape of the grown Pd adislands is kinetically determined. In the Pd coverage range below 0.2 ML, they consist also of dimer chains oriented along the closed-packed $[\bar{1}10]$ direction.

What is the origin of the vacancy and the adatom islands? The high solubility of hydrogen at room temperature into the Pd bulk is well known [6-10] and we assume that the formation of vacancy and adatom islands is associated with the diffusion of hydrogen onto subsurface sites and into the Pd bulk. The scenario shown in the STM images of figure 4.3.a and b can be rationalized as follows (figure 4.4): After H_2 dissociation, the hydrogen atoms are adsorbed on the Pd substrate on sites with almost threefold coordination (figure 4.4.a) [3, 8]. In order to establish the equilibrium between hydrogen adsorption / desorption and bulk diffusion, some H atoms have to open up their way into the Pd bulk. The most favorable binding geometry in the fcc lattice is the octahedral site [6]. In order to reach this site the hydrogen atom has to penetrate the topmost Pd layer in the $[\bar{1}\,\bar{1}\,\bar{1}]$ direction. Due to the instability of the (110) surface, the Pd atom from the topmost layer is kicked out and replaced by the hydrogen atom (figure 4.4.b). The H atom is now surrounded by the densely packed (111) facets of the Pd crystal and subsequent diffusion into the Pd bulk can be achieved via interstitial sites. The kicked-out Pd atoms nucleate on the large terraces (figure 4.4.c) and some of them may also reach the step edges. Compared to direct hydrogen attack at step edges, this process is much less probable. Taking into account the high density of Pd rows growing from the edge as well as their regular arrangement (see figure 4.3.b), it seems likely that the main part of adatom rows growing from step edges are due to the direct hydrogen attack.

At the beginning of the hydrogen exposure, the coverage of Pd adatoms is proportional to the hydrogen exposure (figure 4.5). Measurements with different hydrogen partial pressures reveal a proportionality factor m = 0.004 ML / Langmuir H_2. Considering our simple model, this amount of Pd adatoms is equal to the minimum amount of hydrogen atoms dissolved in the Pd bulk.
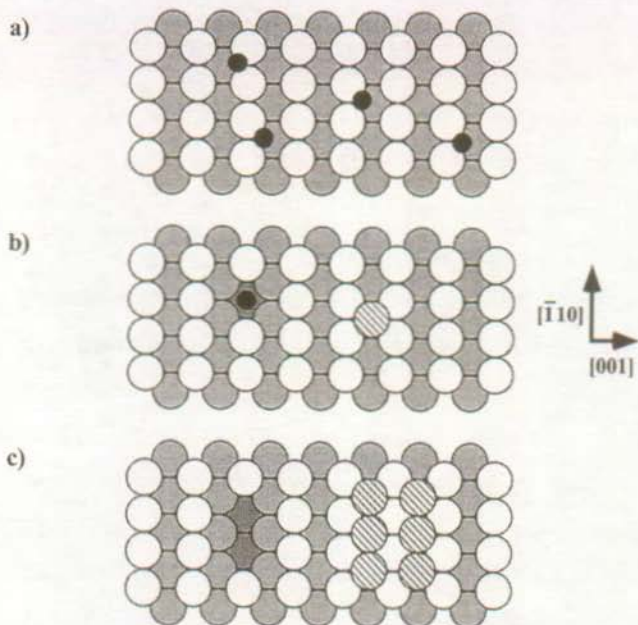
Fig. 4.4: Model explaining the H adsorption on the Pd(110) surface during exposure at 300 K (see STM images of figure 4.3.a and b). a) H atoms adsorb. b) A Pd atom of the topmost layer is kicked out and replace by H. c) Nucleation of the Pd adatoms (hatched circles) and corresponding monovacancies.

It is remarkable here that within the experimental error the graph of figure 4.5 intersects the origin. This result implies that there is no critical hydrogen exposure needed to initiate the morphology changes of the Pd(110) surface. Our experiments indicate that the hydrogen adsorption is not completed instantaneously but covers a time scale of several hours at hydrogen partial pressures $\leq 5 \times 10^{-9}$ mbar. H. Conrad and coworkers have shown that the adsorption / desorption equilibrium is coupled to the bulk diffusion and that relatively long periods are necessary until at a fixed hydrogen partial pressure also a stationary state of surface coverage is reached [12].

At a critical hydrogen exposure above ~ 30 L (depending on partial pressure), the second stage in the restructuring of the surface sets in. This stage involves a substantial mass transport going in hand with a pronounced change in the surface morphology (figure 4.3.c). The amount of missing rows in the surface drastically increases and they start to order laterally.
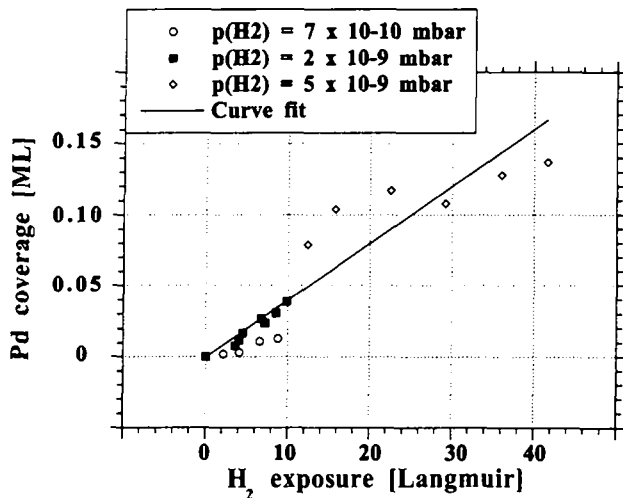
Fig. 4.5: Pd adatom coverage as a function of hydrogen exposure at 300 K for different H_2 partial pressures during the first stage of the reconstruction process. 1 Langmuir = 10^{-6} Torr × second (1 Torr = 1.33 mbar).

Figure 4.3.c.2 shows a zoom-in of figure 4.3.c.1 revealing local ordering of the missing rows in a (1 × 3) superlattice. Also the diatomic added rows start to order. A fair amount of disorder, however, is still present at the surface. This is consistent with the corresponding LEED measurements showing a very streaky (1 × 3) pattern. A further hydrogen exposure substantially improves the order of the missing-row reconstruction. This is demonstrated in figure 4.6. The entire surface exhibits a perfect (1 × 3) ordering which gives rise to a very sharp LEED pattern (figure 4.7). This final transformation into the well-ordered (1 × 3) missing-row phase involves again considerable mass transport. By comparing figure 4.6 with figure 4.3.c.1 and c.2, it becomes evident that the final state is not just due to a lateral ordering of the missing rows but involves intra- and interlayer mass transport. While in the initial stage of the reconstruction only two layers are involved, the fully reconstructed (1 × 3) phase is characterized by a rough morphology with at least 3 layers uncovered. In contrast to the first stage, the second proceeds much faster.
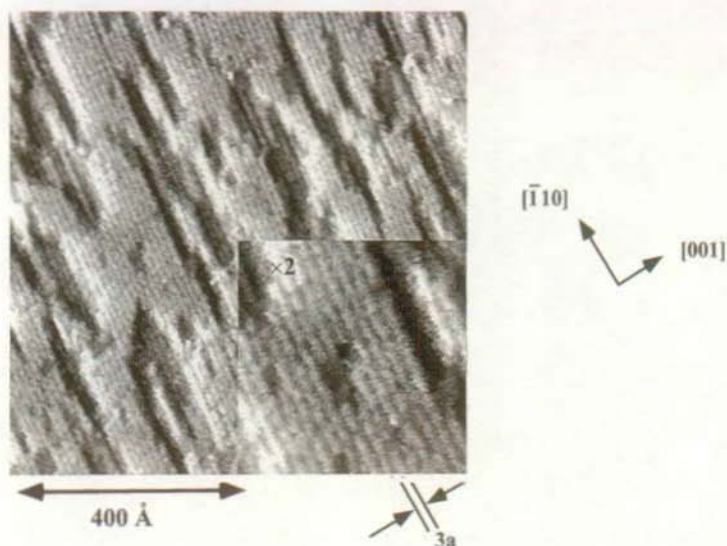
51

$[\bar{1}10]$

$[001]$

400 Å

×2

3a

Fig. 4.6: Hydrogen-induced (1 × 3) reconstruction on the Pd(110) surface at 300 K after 400 min of hydrogen exposure at $p_{H_2} = 2 \times 10^{-9}$ mbar.

(1 × 3)
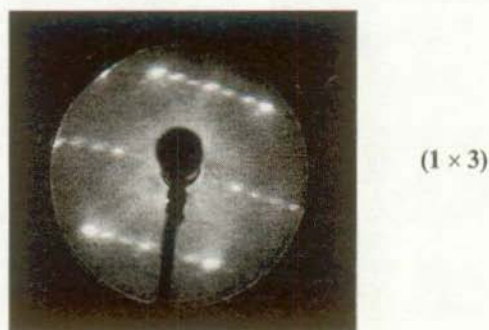
Fig. 4.7: (1 × 3) LEED pattern corresponding to the STM image of figure 4.6 (E = 78 eV).

In figure 4.8 two alternative missing-row types giving rise to a (1 × 3) superstructure on fcc(110) metal are represented. In the first model 4.8.a every third $[\bar{1}10]$ close-packed row within the top layer is missing. V. R. Dhanak and coworkers -who have already discovered the (1 × 2) and (1 × 3) hydrogen induced Pd(110) reconstruction by LEED- interpreted the (1 × 3) superstructure as of the first type [11]. The second type consists of two exposing (111) facets constituted of three rows each (figure 4.8.b). G. Binnig and coworkers were the first to

52

image the Au(110) spontaneous missing-row reconstructions ((1×2) or (1×3)). They proposed this second type [13]. Also I. K. Robinson et al. opted for this structure to explain the carbon induced Pt(110) (1×3) reconstruction [14]. We think that the (1×3) hydrogen induced Pd(110) reconstruction observed on figure 4.6 is described by the first surface structure (figure 4.8.a) because at the beginning of the process the added rows are diatomic whereas vacancy islands are monoatomic.
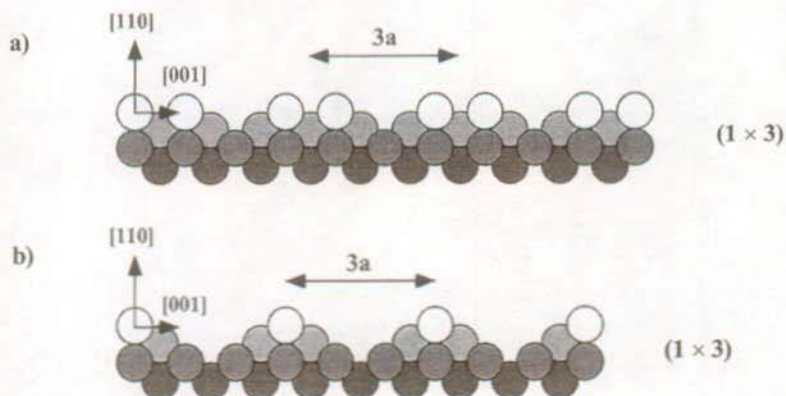

Fig. 4.8: Two alternative models of (1×3) missing-row reconstructions (side view).

The hydrogen induced (1×3) reconstruction was observed at steady-state partial pressures of 7×10^{-10} mbar $\leq p_{H_2} \leq 5 \times 10^{-9}$ mbar. Based on the adsorption isotherms measured by H. Conrad and coworkers and assuming a linearity between work function changes and hydrogen surface coverage Θ_H [12], the hydrogen-induced (1×3) surface phase exists at 300 K in the coverage range between 0.3 ML $\leq \Theta_H \leq 0.5$ ML. A monolayer here is defined by the maximum change in work function measured by H. Conrad et al. and is equivalent with the saturation coverage of hydrogen on the Pd(110) surface at T $\geq$ 300 K.

Increasing the partial pressure to $p_{H_2} = 5 \times 10^{-8}$ mbar (corresponding to $\Theta_H = 0.8$ ML) results in a two-phase regime which is shown in the STM image of figure 4.9. Patches of the (1×3) reconstructed surface coexist besides large patches of a (1×2) reconstructed surface. According to a model proposed by J. Yoshinobu and coworkers [3], the (1×2) structure at room temperature consists of 1 ML hydrogen adsorbed on quasi threefold hollow sites of the missing and/or added Pd rows. Following the already mentioned adsorption isotherms, the

hydrogen partial pressure at 300 K must be raised to $p_{H_2} > 10^{-6}$ mbar to achieve a perfect (1×2) reconstruction. Indeed J. Yoshinobu et al. observed by STM a well-ordered (1×2) structure with an ambient pressure $p_{H_2} = 5 \times 10^{-7}$ mbar corresponding to $\Theta_H = 0.9$ ML.

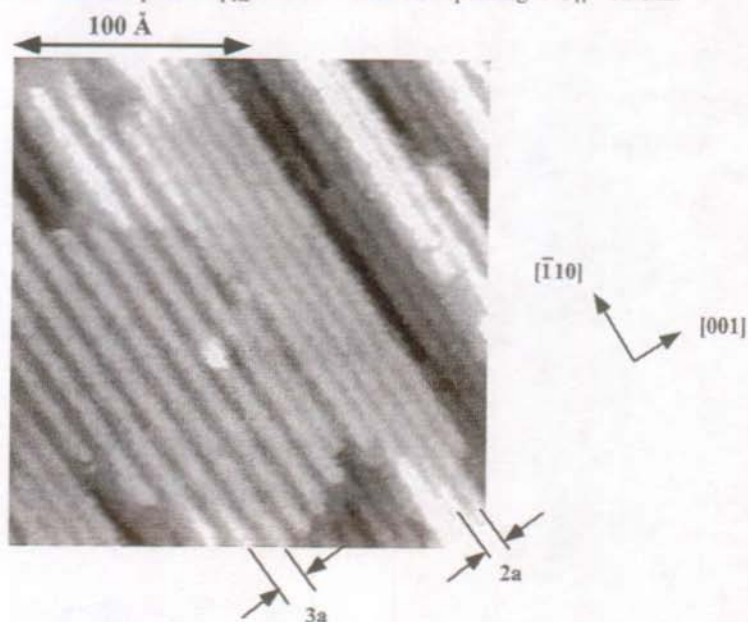Fig. 4.9: Coexistence of the hydrogen-induced (1×3) and (1×2) reconstructions on the Pd(110) surface at 300 K after 150 min of hydrogen exposure at $p_{H_2} = 5 \times 10^{-8}$ mbar.

4.3. Discussion

Annealing experiments show that the hydrogen-induced reconstructions are stable up to about 350 K. At this temperature the missing-row reconstructions, the (1×3) as well as the (1×2) phase, are lifted and a nearly perfect (1×1) surface structure is re-established. The temperature, where the lifting of the reconstruction takes place, coincides roughly with the maximum in the thermal desorption spectrum of adsorbed hydrogen [12]. We can, however, not unequivocally determine if desorbing hydrogen is the major destabilizing force of this transition, as V. R. Dhanak et al. have shown that the (1×2) reconstructed Pd(110) surface is stable up to 355 K and the (1×3) reconstructed Pd(110) surface is stable up to 370 K both without any presence of adsorbed species [11] in close accordance with our experimental

finding. They interpreted the limited stability of the reconstructed surfaces as determined by surface mobility.

The reconstruction scenario described here is similar to the hydrogen induced (1 × 2) restructuring of the Ni(110) surface [4]. For this system L. P. Nielsen et al. studied the reconstruction kinetics by STM and evolved a combined missing-row / added-row reconstruction model. At low hydrogen coverages, the authors also observed a low number of vacancy islands and Ni adatom islands both elongated along the close-packed [$\overline{1}$10] direction. Increasing the hydrogen coverage resulted in an increase of the amount of Ni rows which ended up in the regular arrangement of a (1 × 2) reconstruction. No further ordered phase of the H/Ni(110) system was observed. The kicked-out Ni atoms were found to nucleate at the surface to form monoatomic chains which had to be stabilized by adsorbed hydrogen. The missing rows and the added rows were observed in a hydrogen atmosphere. When the hydrogen was pumped away, the density of added and missing rows slowly decreased due to thermal desorption of hydrogen. The Ni(110) surface finally relaxed into the original (1 × 1). For the H/Ni(110) system the restructuring of the surface is reversible and it depends on the adsorbed hydrogen coverage. This is at variance with the behavior of the H/Pd(110) system. The reconstructed Pd(110) surface is stable up to 350 K, the atoms nucleate at the surface to form adatom islands whose shape is kinetically determined by the temperature and the low Pd flux. It is not required to stabilize these Pd adatom islands by adsorbed hydrogen. Moreover, in the case of Pd(110) the adislands do not take part in the main reconstruction process. This starts in the first Pd layer with the lateral ordering of the missing rows. Therefore the reconstruction process might be better described as being from the missing-row type.

The multi-phase behavior of the hydrogen-induced reconstruction can be related to the small energy difference between the (1 × n) missing-row reconstructions of the transition metals [15]. The structure, thus, responds very sensible to the charge redistribution at the surface associated with the hydrogen coverage. A very similar behavior has been observed for the Pt(110) surface [14]. The surface segregation of carbon impurities was found to change the (1 × 2) missing-row phase of the clean surface into a (1 × 3) phase by passing via a (1 × 5)

phase. The (1×5) phase was identified to be an semi-ordered arrangement of (1×2) and

(1×3) missing-row units; i.e. it corresponds to the ordered analog of the (1×2) - (1×3)

phase mixture seen for the H/Pd(110) system.

4.4. References

[1] D. P. Woodruff, *Adsorbate-induced reconstruction of surfaces: an atomistic alternative to microscopic faceting?*, J. Phys.: Condens. Matter **6**, 6067 (1994).

[2] H. Niehus, C. Hiller and G. Comsa, *ROW PAIRING INDUCED BY HYDROGEN ADSORPTION AT Pd(110)*, Surf. Sci. Lett. **173**, L599 (1986).

[3] J. Yoshinobu, H. Tanaka and M. Kawai, *Elucidation of hydrogen-induced (1 x 2) reconstructed structures on Pd(110) from 100 to 300 K by scanning tunneling microscopy*, Phys. Rev. B **51**, 4529 (1995).

[4] L. P. Nielsen, F. Besenbacher, E. Laegsgaard and I. Stensgaard, *Nucleation and growth of a H-induced reconstruction of Ni(110)*, Phys. Rev. B **44**, 13156 (1991).

[5] G. Kleinle, M. Skottke, V. Penka, G. Ertl, R. J. Behm and W. Moritz, *MECHANISTIC AND ENERGETIC ASPECTS OF THE H-INDUCED (1 x 2) RECONSTRUCTED STRUCTURES ON Ni(110) AND Pd(110)*, Surf. Sci. **189/190**, 177 (1987).

[6] B. S. Kang and K. S. Sohn, *Diffusion processes and interaction of hydrogen atoms in Pd*, Physica B **205**, 163 (1995).

[7] R. J. Behm, M. Penka, M. G. Cattania, K. Christmann and G. Ertl, *Evidence for "subsurface" hydrogen on Pd(110): An intermediate between chemisorbed and dissolved species*, J. Chem. Phys. **78**, 7486 (1983).

[8] K. H. Rieder, M. Baumberger and W. Stocker, *Selective Transition of Chemisorbed Hydrogen to Subsurface Sites on Pd(110)*, Phys. Rev. Lett. **51**, 1799 (1983).

[9] W. Eberhardt, S. G. Louie and E. W. Plummer, *Interaction of hydrogen with a Pd(111) surface*, Phys. Rev. B **28**, 465 (1983).

[10] T. Engel and H. Kuipers, *A MOLECULAR-BEAM INVESTIGATION OF THE SCATTERING, ADSORPTION AND ABSORPTION OF H2 AND D2 FROM/ON/IN Pd(111)*, Surf. Sci. **90**, 162 (1979).

[11] V. R. Dhanak, G. Comelli, G. Paolucci, K. C. Prince and R. Rosei, *Metastable (1 x 2) and (1 x 3) reconstructions of Pd(110)*, Surf. Sci. Lett. **260**, L24 (1992).

[12] H. Conrad, G. Ertl and E. E. Latta, *ADSORPTION OF HYDROGEN ON PALLADIUM SINGLE CRYSTAL SURFACES*, Surf. Sci. **41**, 435 (1974).

[13] G. Binnig, H. Rohrer, C. Gerber and E. Weibel, *(111) FACETS AS THE ORIGIN OF RECONSTRUCTED Au(110) SURFACES*, Surf. Sci. Lett. **131**, L379 (1983).

[14] I. K. Robinson, P. J. Eng, C. Romainczyk and K. Kern, *Higher Order Reconstructions of Pt(110) Induced by Impurities*, Surf. Sci. **367**, 105 (1996).

[15] M. Garofalo, E. Tosatti and F. Ercolessi, *STRUCTURE, ENERGETICS, AND LOW-TEMPERATURE BEHAVIOUR OF THE Au(110) RECONSTRUCTED SURFACE*, Surf. Sci. **188**, 321 (1987).

5. Reactions at the Si/Pd(110) interface

5.1. Introduction

Silicide formation at metal-silicon interfaces has been studied extensively, both because of its practical importance in semiconductor device physics and because epitaxial silicide films provide well-defined model systems for basic studies of interface reactions [1-5]. Much was learned about these fascinating systems, however, a complete microscopic understanding of the mechanisms for silicide formation at the interface is still lacking. Moreover, nearly all experimental studies of silicide formation concerned the reaction of deposited metals on silicon surfaces; the inverse scenario -Si deposition on metal surfaces- has rarely been studied [6-9]. The interest to study the silicide formation at the Si/Pd(110) interface arises because palladium-silicide provides the advantage of relative ease of fabrication and compatibility with existing semiconductor processing technology [10]. It was found that Pd films deposited on Si substrate at room temperature produced a polycrystalline Pd_2Si in the Pd/Si interface. Pd_2Si formed on Si(111) surface becomes epitaxial after annealing at 600 K [10].

In this chapter we report in situ scanning tunnelling microscopy (STM) and reflection absorption infrared spectroscopy (RAIRS) results of the growth of Si and/or silicide on the Pd(110) surface in the temperature range $100 K \leq T \leq 550 K$. The crucial parameter for the silicide growth is the deposition temperature, which determines the competition between Si subsurface diffusion and silicide formation. Despite the immiscibility of Pd and Si in the bulk [11, 12], silicon is found to dissolve in the selvedge of the Pd crystal. This system thus constitutes a further example of surface mixing of elements immiscible in the bulk; a phenomenon which was predicted many years ago [13] but discovered experimentally only recently for metal-on-metal [14, 15] and metal-on-semiconductor systems [16]. Our results demonstrate the following behavior of the Si/Pd(110) system. Below 140 K Si does not react with the Pd surface and amorphous silicon clusters form during deposition. With increasing temperature, Si penetrates into the metal surface and silicide is formed. Between 140 K and 320 K the silicide is amorphous, while above 320 K it is crystalline growing in well-shaped islands. The crystalline silicide islands are found to be unstable at elevated temperatures.

The combination of STM and RAIRS offers a unique possibility of correlating surface chemical analysis with atomic-level surface structure. This is particularly important in the case of very reactive systems like Si/Pd. As chemical sensor we will use the CO molecule which is adsorbed onto the well prepared and characterized heterogeneous surfaces. The frequency of the internal stretch vibration, which is easily accessible with RAIRS, responds quite sensitively to the chemical nature of its surrounding and it is thus a valuable probe of the surface chemical composition. Another motivation to investigate silicide layers by RAIRS comes from the fact that they exhibit a high reflectivity, comparable with metals, whereas Si single crystals are almost transparent in the infrared region [17].

Relatively little is known about the adsorption of CO onto semiconductor surfaces [18-20]. On the Si(100)-(2 × 1) surface CO molecules adsorb nondissociatively in bridge configuration on Si dimers [19, 20]. The infrared absorption at 2081 cm^{-1} is very close to the gas phase value (2143 cm^{-1}) indicating that the interaction of CO with the substrate is weak [20]. It is assumed that the CO molecule adsorbs in an upright position on top of the Si dimers. The molecule already desorbs at 220 K. On the Si(111)-(7 × 7) surface CO does not chemisorb at temperatures above 100 K [20]. On the other hand, the interaction of CO with metal surfaces was extensively studied and is reasonably well understood. On the Pd(110) substrate the CO molecule is adsorbed in short bridge site on adjacent Pd atoms [21-23]. The CO/Pd(110) monolayer reveals a (2 × 1) superstructure with *p2mg* symmetry with the C atoms at the surface. The infrared absorption of the internal stretch mode is centered at 2000 cm^{-1}. The CO molecules desorb at about 350 K [24]. Up to now there is no information available concerning the adsorption of CO on heterogeneous silicon/metal surfaces.

5.2. Basic experimental observations

5.2.1. Silicide formation as a function of temperature

At low temperatures (< 140 K) Si does not react with the Pd(110) surface. The Auger spectrum shows only one single Si peak at 92 eV demonstrating the absence of silicide formation [10]. The unreactive deposition at low temperatures is confirmed by vibrational spectroscopy of adsorbed CO. The series of spectra in figure 5.1.b depicts the dependence of

the CO vibration frequency on the Si deposition temperature. The Si deposition time is the same at each temperature (36 min). In order to facilitate the interpretation of the data, we have added spectra of CO on amorphous Si, a-Si, (a) and on clean Pd(110) (c) as references. The IR absorption of CO adsorbed on a-Si is centered at 2104 cm^{-1} and is $\approx$ 40 cm^{-1} red-shifted with respect to the gas phase. The infrared absorption of CO adsorbed on the clean Pd(110) surface shows a more significant red-shift of about 150 cm^{-1} with respect to the gas phase value indicating the strong interaction of CO with the metal surface. The peak maximum is centered at 2000 cm^{-1}. Upon deposition of Si onto the clean Pd(110) surface at a temperature below 140 K, the same vibrational band as on a-Si at 2104 cm^{-1} is detected (figure 5.1.b.1). There is no significant shift visible indicating the absence of any reaction of Si with the Pd substrate. The second absorption band around 2000 cm^{-1} is easily determined as being due to CO adsorbed on the remaining, uncovered Pd substrate sites (compare with figure 5.1.c) characterizing CO adsorption on clean Pd(110) in bridge configuration.

Above 140 K the deposition of Si on Pd(110) is reactive. Auger spectroscopy shows a different spectrum consisting of four peaks around 92 eV. It resembles much the spectrum assigned to Pd$_2$Si obtained by S. Okada and coworkers [10]. This close resemblance suggests that Pd$_2$Si is the reaction product of Si deposited on Pd(110) at T > 140 K. The silicide formation is also evident in the vibrational spectra of chemisorbed CO. Three representative spectra of CO adsorbed on silicide/Pd(110) are shown in figure 5.1.b.2, b.3 and b.4. One monolayer CO was dosed onto the surfaces at 100 K after Si deposition at 300 K (b.2), 400 K (b.3) and 550 K (b.4). The three IR spectra are similar. They show two distinct absorption bands: a low frequency band at 2000 cm^{-1} and a high frequency band at 2074 cm^{-1} (b.3, b.4) and 2090 cm^{-1} (b.2), respectively. The low frequency mode corresponds to CO bound in bridge position to Pd atoms of the uppermost layer, while the high frequency mode indicates the presence of silicide in this layer. The silicide formation is evident by comparing the spectra with the analogous spectrum of amorphous Si on Pd(110) in figure 5.1.b.1. The frequency has red-shifted by 30 cm^{-1} upon Si deposition at and above 400 K and by 14 cm^{-1} upon deposition at room temperature. In figure 5.1.d are displayed three STM images characterizing the silicide growth on Pd(110) as a function of temperature. At 300 K,

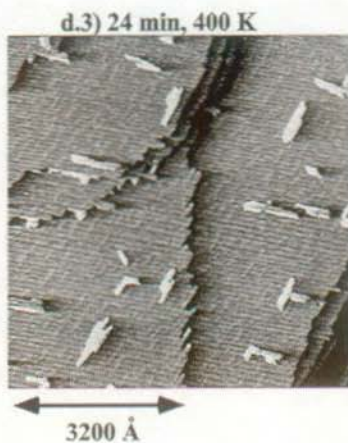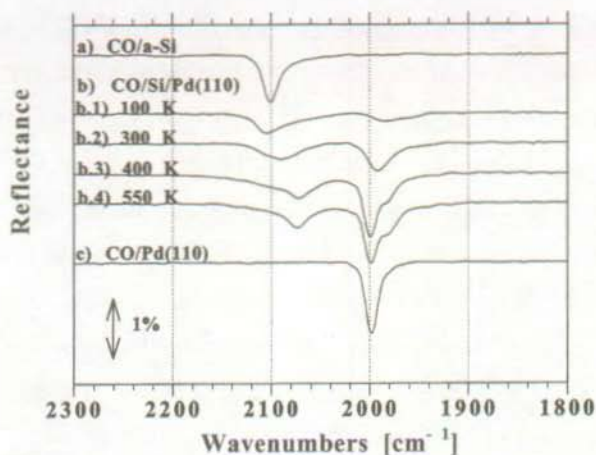Fig. 5.1: Infrared spectra of one monolayer CO adsorbed on: a) amorphous Si, b) Si/Pd(110) after a Si deposition time of 36 min at 100 K (b.1), 300 K (b.2), 400 K (b.3) and 550 K (b.4), c) clean Pd(110). Monolayer coverage was obtained after dosing 40 L CO at 100 K. d) Corresponding STM images obtained after a Si deposition time of 24 min at 300 K (d.2), 24 min at 400 K (d.3) and 36 min at 550 K (d.4).

amorphous silicide clusters nucleate on the surface (d.2). At 400 K, well shaped crystalline silicide islands grow epitaxially on Pd(110) (d.3). And at 550 K, the island strain is relieved through misfit dislocations and an entire silicide layer covers the substrate (d.3). By comparing the IR data to the STM measurements of figure 5.1.d, the band at 2074 cm^{-1} can be assigned to crystalline silicide while the broad vibrational band at 2090 cm^{-1} corresponds to CO adsorption on small amorphous silicide clusters.

5.2.2. Calibration of deposition rate by RAIRS on Si/Pd(110) at 100 K

The deposition rate of Si on Pd(110) at T = 100 K was calibrated by means of STM images and RAIR spectroscopy of adsorbed CO. At low coverages the STM data reveal that Si growth is two-dimensional. The area covered by Si and the IR signal of Si-bound CO are a direct measure for the Si dosage assuming a sticking coefficient of one.

In the whole coverage range, the absorption bands at 2104 cm^{-1} (CO/a-Si) and 2000 cm^{-1} (CO/Pd) of the RAIR spectra (as in figure 5.1.b.1) have still been observed. This indicates that no reaction occurs. With increasing Si coverage, the band at 2000 cm^{-1} due to CO bound to Pd atoms of the substrate decreases whereas the band at 2104 cm^{-1} due to CO bound to unreacted Si atoms progressively increases. The relative integrated intensities (with respect to the integrated absorption of the whole spectrum) are plotted in figure 5.2. For low Si coverage, the relative peak intensity of CO/Si is proportional to the Si coverage. In figure 5.2 we find by interpolation that 1 ML is reached after a deposition time of (30 ± 5) min which gives a rate of R = $(5.5 \pm 0.9) \times 10^{-4}$ MLs^{-1}. Thus the Si coverage values which will be given later are accurate at about 15%.

The graph of figure 5.2 shows that Si deposited at 100 K on Pd(110) grows in a three-dimensional mode because Si intensity saturates at a deposition time of $\approx$ 40 min. Although the amount of Si deposited on the surface exceeds 1 ML for the IR spectrum of figure 5.1.b.1 (1.2 ML), the Pd substrate is not yet completely covered. Both vibrational bands of the Si/Pd(110) surface are inhomogeniously broadened indicating that the clusters of amorphous Si and the remaining patches of the Pd substrate are small and randomly distributed. The amorphous structure of the Si clusters is confirmed by the LEED pattern which is more and more diffuse as Si is deposited on Pd(110) at 100 K.
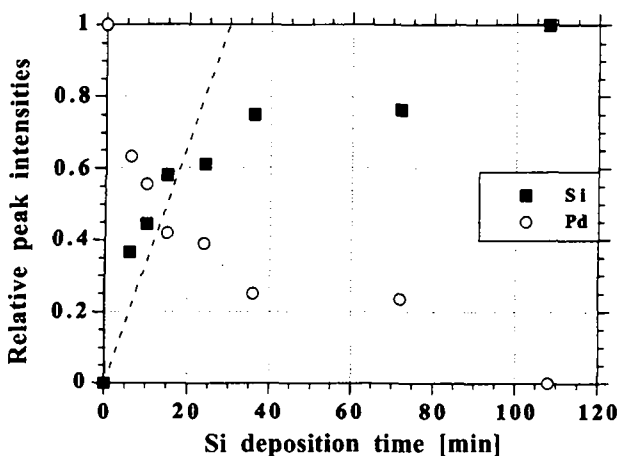
61

Fig. 5.2: Relative integrated intensity of the absorption bands of CO adsorbed on Si/Pd(110) at 100 K as a function of Si deposition time. The absorption band of CO bound to Si atoms is centered at 2104 cm⁻¹ (solid squares) and the one of CO bound to Pd substrate atoms at 2000 cm⁻¹ (open circles).

5.3. Growth morphology of silicide

The growth morphology of silicide resulting from the deposition of Si on Pd(110) has been studied in the temperature range 300 K - 550 K by variable temperature STM. At room temperature a high density of amorphous silicide clusters nucleates on the Pd(110) surface. Upon increasing the temperature above 320 K crystalline silicide islands are formed.

5.3.1. Room temperature grown silicide

5.3.1.1. Amorphous silicide clusters

Figure 5.3 shows as an example the nucleation of palladium silicide (likely Pd_2Si) clusters at 300 K after deposition of 0.8 and 1.8 ML Si. The clusters formed at submonolayer Si coverage (figure 5.3.a) have a typical size of 10 Å - 40 Å and a height of $\approx$ 0.7 Å and are uniformly distributed on the surface. In fact these silicide clusters are implanted in the first Pd layer emerging above the surface by $\approx$ 1/2 step height. They result from the chemical reaction of the impinging Si atoms with the substrate. The steps are also directly attacked by the reaction as seen in figure 5.1.d.2. The corresponding LEED pattern is diffuse indicating that

the clusters have no crystalline structure but are amorphous. Relating this surface morphology to the infrared spectra of figure 5.1.b.2, the anomalously large linewidth becomes quite reasonable. It is likely to be a consequence of both the small size of the silicide clusters and their amorphous structure. It must be noted that these amorphous silicide clusters are stable at 300 K: no evolution has been observed. The silicide formation on Pd(110) bears analogies to the initial growth of palladium-silicide on Si(111) at room temperature where also the formation of amorphous silicide has been observed [25, 26]. At a coverage of 1.8 ML (figure 5.3.b) the surface is also very rough. The irregular structures grown on the amorphous silicide clusters are much larger (~ 100 Å). Their chemical composition cannot be inferred from the STM images but RAIR spectroscopy reveals that a certain Si amount remains unreacted at the surface (see § 5.5.1).

5.3.1.2. Si subsurface diffusion

The STM image in figure 5.4.a reveals a very interesting feature concerning the Si deposition on Pd(110) at room temperature: besides the silicide reaction also a noticeable subsurface diffusion of Si atoms takes place during deposition. This is only observable at a very low Si coverage (≈ 0.06 ML in figure 5.4.a). The Si subsurface diffusion is evident in the surface morphology which shows besides the silicide clusters (SC) the presence of two additional surface structures: substrate holes (SH) and Pd adatom islands (PAI) (arrows point to these structures in figure 5.4). The substrate holes are mostly one monolayer deep and are elongated along the $[\bar{1}10]$ direction; they are mono- or diatomic in width. In addition to these holes we find a small number of Pd adatom islands (PAI), which are arranged as short chains also running along $[\bar{1}10]$. From our homoepitaxy experiments on the Pd(110) surface, we know that Pd atoms deposited at room temperature nucleate in dimer chains running along the close-packed $[\bar{1}10]$ direction (see chapter 3). We can thus identify the chain-like clusters as Pd adatom islands (PAI).

A likely scenario to explain this morphology is the following. It is schematized by a hard-sphere model in figure 5.4.b just below the STM image. During deposition, a certain proportion of the Si atoms react with the Pd atoms of the substrate to form silicide clusters (SC), the other part of deposited Si may diffuse subsurface. Firstly, they penetrate the
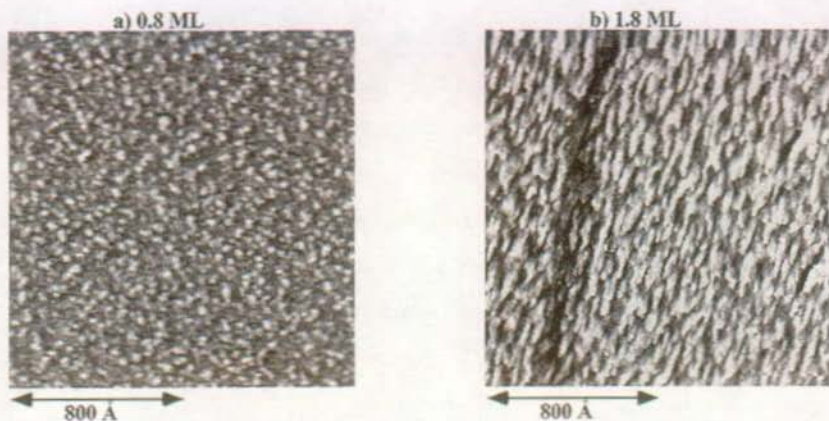
63

a) 0.8 ML **b) 1.8 ML**

800 Å   800 Å

Fig. 5.3: STM images showing the surface morphology after Si deposition on Pd(110) at 300 K. The Si coverages are indicated.

PAI   a)   ≈ 0.06 ML

[$\bar{1}$10]

[001]

300 Å

SC   SH   PAI

Fig. 5.4: a) Surface morphology as observed after the deposition of ≈ 0.06 ML Si on Pd(110) at 300 K. Si atoms can either react with the substrate to form silicide clusters (SC) or diffuse subsurface resulting in the creation of substrate holes (SH) and few Pd adislands (PAI). b) Hard-sphere model schematizing this mechanism.

● Pd adatom
○ Pd atom of the first layer
◉ Pd atom of the nth layer ($n \geq 2$)
⊗ Si atom

b)

[$\bar{1}$10]

[001]

substrate by exchanging their place with Pd atoms of the top surface layer. Since we observe holes in the substrate (SH) it is likely to assume that some of the incorporated Si atoms leave the surface sites and diffuse deeper into the Pd bulk. This process might be explained as follows. A nearby Pd atom in the surface layer is ejected to create a vacancy, which then can be filled by a Pd atom from the second layer exchanging its place with the Si atom in the first layer. A kicked-out Pd atom diffuses on the surface until it gets trapped: it can nucleate with other Pd adatoms and then form Pd adislands (PAI) or can react with Si adatoms to form additional silicide clusters (SC). Due to the anisotropic structure of the substrate, vacancy islands and Pd adislands are elongated along $[\bar{1}10]$ at room temperature (see chapters 3 and 4). This mechanism ensures an efficient subsurface diffusion of Si and is compatible with the morphology seen in figure 5.3.a. It is interesting to note that a very similar scenario as reported above for Si subsurface diffusion has been observed in the case of Au mixing into Ni(110) [14] and H penetration into the (110) surfaces of Pd [27] (see also chapter 3) and Ni [28]. Also in these cases the substrate penetration seems to occur via coupled exchange processes generating substrate holes and adislands. We can however exclude that the substrate holes of figure 5.4.a (SH) are induced by adsorption from the residual gas because the STM measurement has been done immediately after deposition and the background pressure was $\approx 2 \times 10^{-10}$ mbar.

5.3.2. High temperature (350 - 550 K) grown silicide

Above 320 K Si atoms also react with the Pd substrate to form a silicide as seen in RAIR spectra of figure 5.1.b.3 and b.4. The Auger spectra are of the same kind as those observed at 300 K suggesting again the formation of the compound Pd_2Si. But the reaction scenario is completely different: the silicide grows in well-shaped monocrystalline islands.

5.3.2.1. Crystalline silicide islands at 350 and 400 K

Figure 5.5.a displays two STM images characterizing the silicide growth on the Pd(110) surface at 350 K. The surface morphology has drastically changed with respect to Si deposition at 300 K: silicide now grows in well-shaped crystalline islands. For a very low coverage of 0.02 ML (figure 5.5.a.1), Si atoms predominantly react at step edges: this is noticeable because step edges become facetted. The crystalline silicide islands are hardly

65

visible at the facetted edges (lighter areas indicated by arrows in figure 5.5.a.1) which adopt their symmetry. One can find also a unique crystalline silicide adisland on the terrace (in white). Upon further Si deposition, numerous small islands are formed in and on the uppermost Pd layer (figure 5.5.a.2).

At 400 K the mobility is higher and the crystalline islands start to nucleate in the terrace and at the steps (figure 5.5.b.1) before one can find adislands on the terrace (figure 5.5.b.2). The morphology shown in the STM images of figures 5.5.a.2, b.2, and b.3 is exactly the same: two kinds of well-shaped silicide islands are formed, one embedded in the first Pd layer and the other on the Pd(110) surface, one step height above. The adislands (AI) and the embedded islands (EI) (see arrows in figure 5.5.b.2) are rhomboid. There are two domains visible which are oriented along the diagonal $[\bar{1}12]$ and $[\bar{1}1\bar{2}]$ directions of the Pd(110) surface unit cell (see vectors in the center of figure 5.5). The silicide islands have a crystalline structure as revealed by the LEED pattern (see § 5.3.2.3).

The two types of crystalline silicide islands give further evidence for the penetration of Si atoms into the substrate. The embedded silicide islands (EI) are formed by the direct reaction of Pd in the surface layer with impinging Si atoms. STM data in grey scale height representation reveal a height expansion of about 30% of the silicide layer compared to the Pd layer indicating the presence of additional atoms in that layer. The second type of silicide islands (adislands = AI), grown on top of the surface, is formed through reaction of Si adatoms with ejected Pd adatoms occuring at the beginning of the Si subsurface diffusion process (§ 5.3.1.2). The density of the embedded silicide islands is much higher than that of the adislands. This can be understood because the flux of Si atoms arriving at the Pd surface is larger than the "effective flux" of Pd adatoms ejected onto the surface due to the Si-Pd exchange. The nucleation probability of embedded silicide islands is thus higher than the probability that Si and Pd adatoms meet and nucleate an adisland.

At 400 K it is not possible to grow embedded islands on the whole substrate. From about 2 ML Si, the silicide growth is no more epitaxial and amorphous clusters cover the crystalline islands (figure 5.5.b.4) as also indicated by a diffuse LEED pattern (not shown). The chemical

a) T = 350 K

a.1) 0.02 ML   a.2) 0.1 ML

800 Å   800 Å

b) T = 400 K

b.1) 0.1 ML   b.2) 0.4 ML

EI

AI

1600 Å   1200 Å

$2[\bar{1}10]$ $[\bar{1}12]$

$[\bar{1}1\bar{2}]$ $2\,[001]$

b.3) 0.6 ML   b.4) 2.4 ML

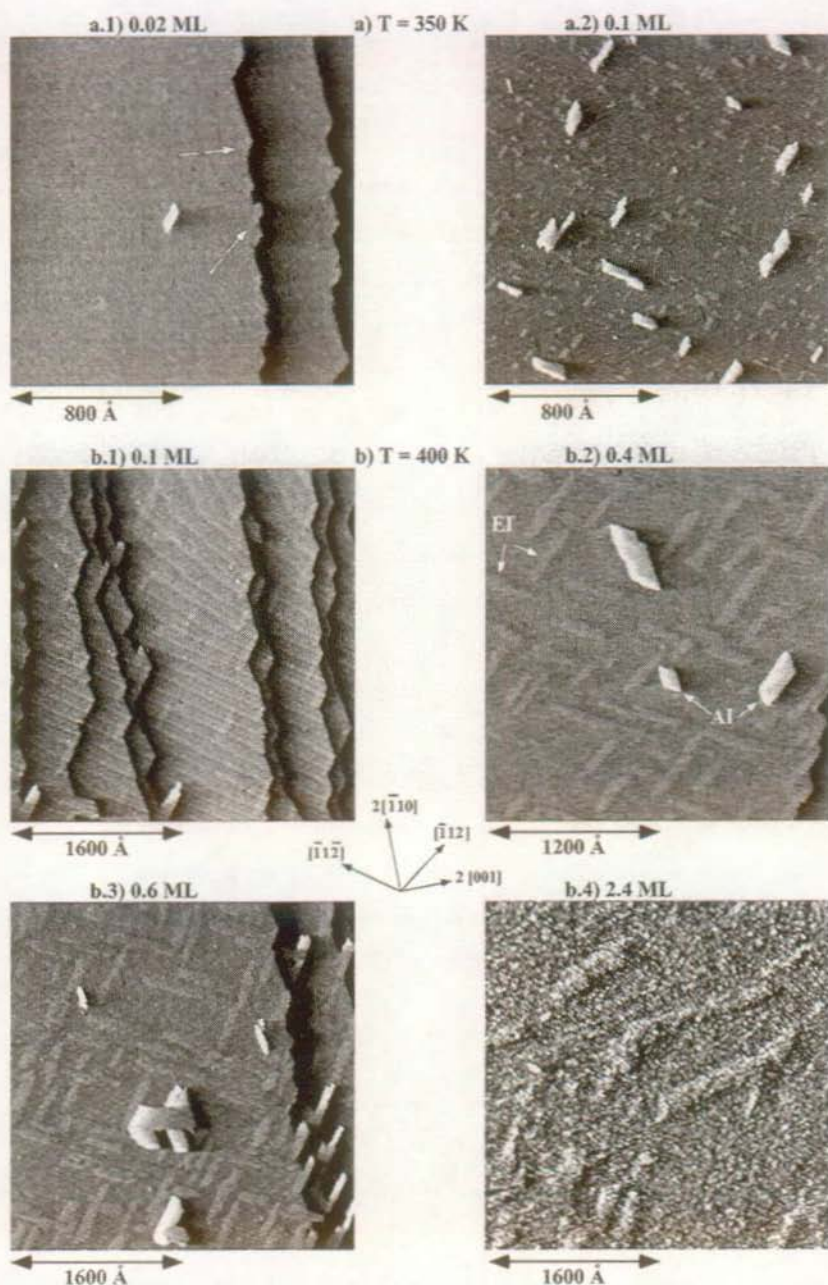1600 Å   1600 Å

Fig. 5.5: The growth of crystalline silicide islands on Pd(110) at 350 K (a) and 400 K (b). a.1) The dashed arrows indicate embedded silicide islands at facetted step edges. b.2) Embedded islands (EI) and adislands (AI) are indicated by arrows. b.4) At 2.4 ML Si, small amorphous clusters cover the epitaxially grown silicide islands.

67

composition of these small clusters can't be inferred from the STM pictures; complementary RAIRS experiment are useful with this respect (see § 5.5.2.2).

5.3.2.2. Strain relief through misfit dislocations at 550 K

With further increasing temperature, migration becomes increasingly faster with respect to deposition, i.e. the nucleation density decreases and only few very large embedded silicide islands grow at 550 K as shown in figure 5.6.a. A pattern of parallel dark stripes visible on the silicide islands attracts particular attention. The depression stripes running along the $[\overline{1}12]$ direction are ≈ 10 Å in width and have an average separation of ≈ 45 Å. We identify these stripes as misfit dislocations partially relieving the strain [29]. The silicide must thus be under substantial compressive strain perpendicular to $[\overline{1}12]$ and islands can only grow coherently up to a critical size. Larger islands have to relieve their strain by the introduction of misfit dislocations. By depositing more Si atoms on the Pd(110) surface at 550 K, it is possible to grow an entire silicide layer as shown in figure 5.6.b. The island at the left-hand side has grown from the step edge showing the same striped structure. The step flow growth mode is well activated at 550 K as shown on the next image (figure 5.6.c.1) where also some elongated silicide islands have nucleated on the first silicide layer. A zoomed area in the STM image of figure 5.6.c.1 reveals the characteristic striped pattern (figure 5.6.c.2). The silicide does not grow layerwise as shown in figure 5.6.d. Silicide growth in the third layer has already started before completing the second. The RAIRS study shows that for coverage above 2.4 ML unreacted Si is present in the topmost layer (see § 5.5.2.1). The LEED pattern indicates that between the misfit dislocations running along $[\overline{1}12]$ exactly the same structure as at 400 K is present (§ 5.3.2.3).

In figures 5.6.a-d only one single domain is visible on a terrace. Another symmetric domain is however present on the surface as revealed by LEED and STM. The appearence of one or the other domain depends on the direction of the step edge. As long as the step edge direction lies between the $[\overline{1}1\overline{2}]$ and the $[\overline{1}10]$ direction, the domain as shown if figure 5.6.a-d will be observed. If it lies between $[\overline{1}10]$ and $[\overline{1}12]$, the second domain will be observed. At higher Si coverages this step edge influence vanishes and both domains are equally distributed on the surface as shown in figure 5.6.e.

a) 0.4 ML

b) 1.2 ML

800 Å

800 Å

c.1) 1.8 ML

c.2) 1.8 ML

3200 Å

400 Å

2[$\bar{1}$10]   [$\bar{1}$12]

[$\bar{1}$1$\bar{2}$]   2[001]

d) 2.4 ML
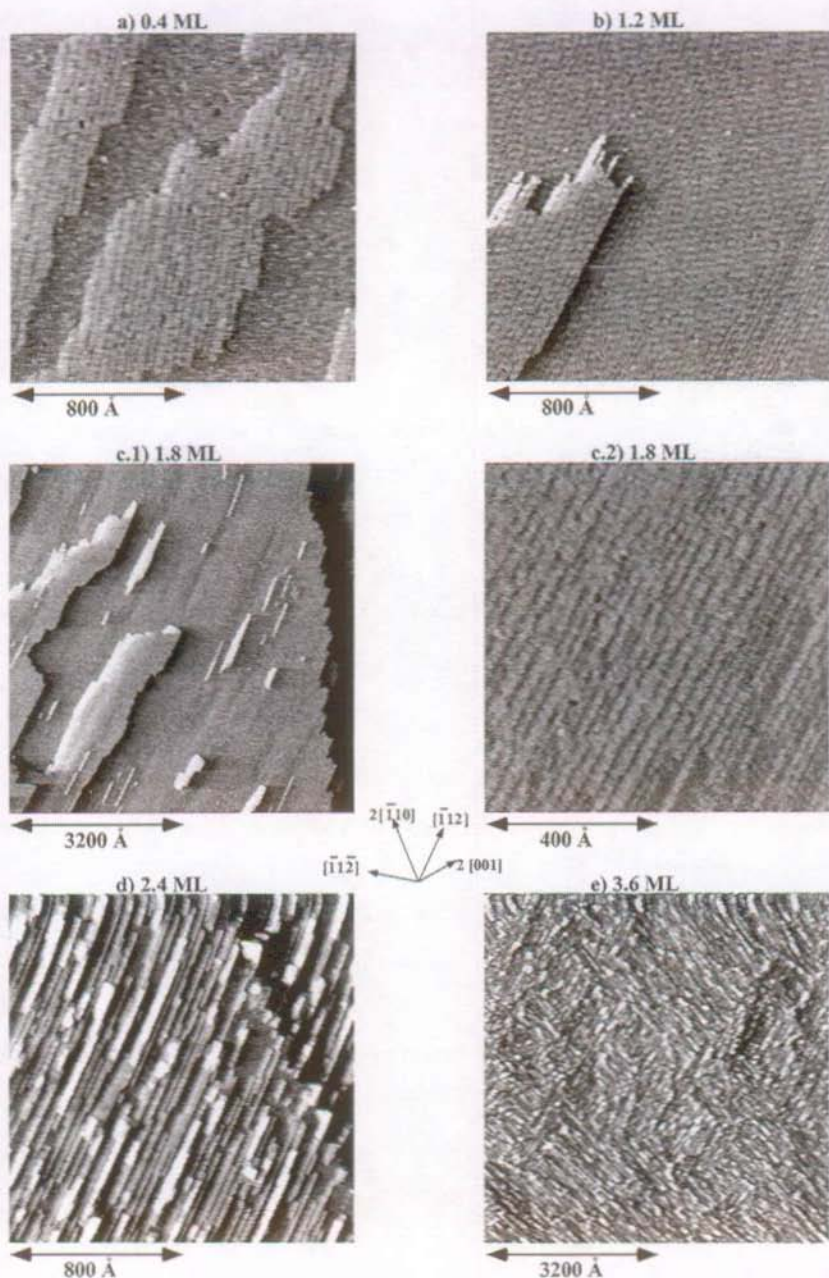
e) 3.6 ML

800 Å

3200 Å

Fig. 5.6: The growth of palladium-silicide on Pd(110) at 550 K at the indicated Si coverages. In figures a - c, the stripes are misfit dislocations relieving the stress. In figure d, already some material is found in the third layer. In figure e, both domains are present (white arrows).

At 400 K silicide islands grow epitaxially on the Pd(110) substrate indicated by a sharp LEED superstructure. We will determine the associated matrix. The LEED pattern of crystalline silicide formed after deposition of 0.6 ML Si on Pd(110) at 400 K is displayed in figure 5.7.a. The basis vectors of the Pd(110) reciprocal lattice $\vec{a}_1^{\ast}$ and $\vec{a}_2^{\ast}$ are easily recognized. The superstructure basis vectors in the reciprocal space are defined as:

$$\vec{b}_1^{\ast} = \frac{1}{4}\vec{a}_1^{\ast} \pm \frac{1}{4}\vec{a}_2^{\ast}$$
$$\vec{b}_2^{\ast} = \vec{a}_2^{\ast}$$

$$(5.1)$$

$\tilde{b}_1^{\ast}$ defines two domains (the + and the - domain). Equation 5.1 is written in matrix form just below the LEED image in figure 5.7.a. The matrix M relating $\vec{b}_i$ and $\vec{a}_i$ in the direct space is given by the inverse transposed matrix of $M^{\ast}$ [30]:

$$M = \tilde{M}^{\ast -1}$$

$$(5.2)$$

This relation is written in figure 5.7.b with the corresponding vectors. The vectors $\vec{b}_i$ spanning the unit cell of the silicide superstructure are:

$$\vec{b}_1 = 4\vec{a}_1$$
$$\vec{b}_2 = \pm\vec{a}_1 + \vec{a}_2$$

$$(5.3)$$

The vectors $\vec{b}_i$ define two rhomboid shaped unit cells resulting in two domains characteristic for crystalline silicide islands (embedded and adislands) formed at 350 K and 400 K (figure 5.5.a.1 - b.3).

In figure 5.7.b we show a model of crystalline Pd_2Si on Pd(110) which is consistent with the LEED pattern. The large white balls represent the Pd atoms of the well-known uppermost (110) layer. The black balls represent the Si atoms incorporated between the first and the second Pd layer. They are placed in the troughs on almost threefold hollow sites in the way to form the $\begin{pmatrix} 4 & 0 \\ \pm 1 & 1 \end{pmatrix}$ superstructure. Each cell contains 4 Pd atoms and 2 Si atoms (stoichiometry Pd_2Si), the Si surface coverage is 0.5 ML. In our model in figure 5.7.b the Si atoms are incorporated at favorable sites with a similar environment as in the Pd_2Si structure grown epitaxially on Si(111) [10, 31]. Furthermore the volume of the unit cell of the Pd_2Si [32, 33] corresponds to the one of the modeled structure knowing that it is $\approx 30\%$ expanded in height.

a) LEED pattern (55 eV)
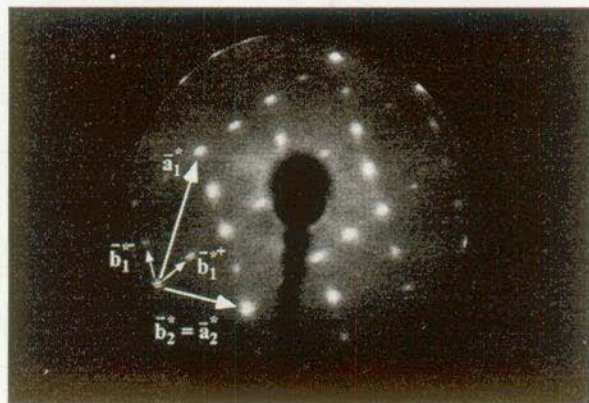
$$\begin{pmatrix} \vec{b}_1^* \\ \vec{b}_2^* \end{pmatrix} = \mathbf{M}^* \begin{pmatrix} \vec{a}_1^* \\ \vec{a}_2^* \end{pmatrix} = \begin{pmatrix} 1/4 & \pm 1/4 \\ 0 & 1 \end{pmatrix} \begin{pmatrix} \vec{a}_1^* \\ \vec{a}_2^* \end{pmatrix}$$

b) Direct space
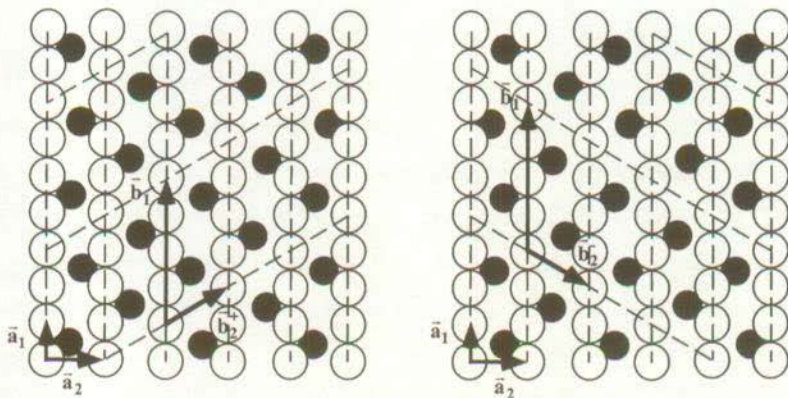
$$\begin{pmatrix} \vec{b}_1 \\ \vec{b}_2 \end{pmatrix} = \tilde{\mathbf{M}}^{*-1} \begin{pmatrix} \vec{a}_1 \\ \vec{a}_2 \end{pmatrix} = \begin{pmatrix} 4 & 0 \\ \pm 1 & 1 \end{pmatrix} \begin{pmatrix} \vec{a}_1 \\ \vec{a}_2 \end{pmatrix}$$

Fig. 5.7: a) LEED pattern of 0.6 ML Si deposited on Pd(110) at 400 K. The sample has been cooled down to 100 K for the LEED measurement (E = 55 eV). The Pd(110) basis vectors $\vec{a}_i^*$ and superstructure vectors $\vec{b}_i^*$ in the reciprocal lattice are indicated in the LEED image. b) Model of Pd_2Si fitting this LEED pattern, b_2 defines two domains. White balls denote the Pd(110) lattice and black balls the Si atoms.

71

In addition to the LEED pattern and the Auger spectra, this is a further support that the stoichiometry of the silicide islands is Pd_2Si.

The LEED measurement on silicide layers grown at 550 K is shown in figure 5.8. It reveals the same $\begin{pmatrix} 4 & 0 \\ \pm 1 & 1 \end{pmatrix}$ LEED pattern as in figure 5.7.a, however, with additional spot splittings along the diagonals indicating a periodic distribution of the misfit dislocations.

Fig. 5.8: LEED pattern of 0.8 ML Si deposited on Pd(110) at 550 K. The sample has been cooled down to 100 K for LEED measurement (E = 84 eV). Note the splitting of the spots along the diagonals.

5.3.2.4. Metastability of crystalline silicide

It is important to note that the crystalline silicide is not stable at elevated temperatures ($T \geq$ 350 K). At about 500 K the islands dissolve on a time scale of minutes while at temperatures below 400 K typical decay times are of the order of hours. This is demonstrated in figure 5.9.b imaging the Pd(110) surface 60 min after 0.4 ML Si deposition at 550 K (the temperature was kept at 550 K). The entire silicide islands have decomposed (compare with figure 5.9.a showing the same zone immediately after deposition), and the Si has disappeared leaving a flat Pd surface with some small holes. As already discussed in § 5.3.1.2, these holes are characteristic for the subsurface diffusion of Si via an exchange process with the Pd substrate atoms. It is most likely that the Si atoms, which are released during the silicide decomposition, diffuse subsurface and bury below the surface. A reevaporation of Si into the gas phase is impossible in the temperature range under study. Also a coarsening of the crystalline silicide into 3D clusters at the surface must be excluded: The large scale image in figure 5.9.b (3200 Å in width) shows no hints of 3D clusters on the flat terrace as well as at

step edges. We have scanned many different zone always observing similarly flat Pd terraces with some holes.

a) immediately after deposition   **b) after 60 min**

2[$\bar{1}$10]   [$\bar{1}$12]

1600 Å   1600 Å

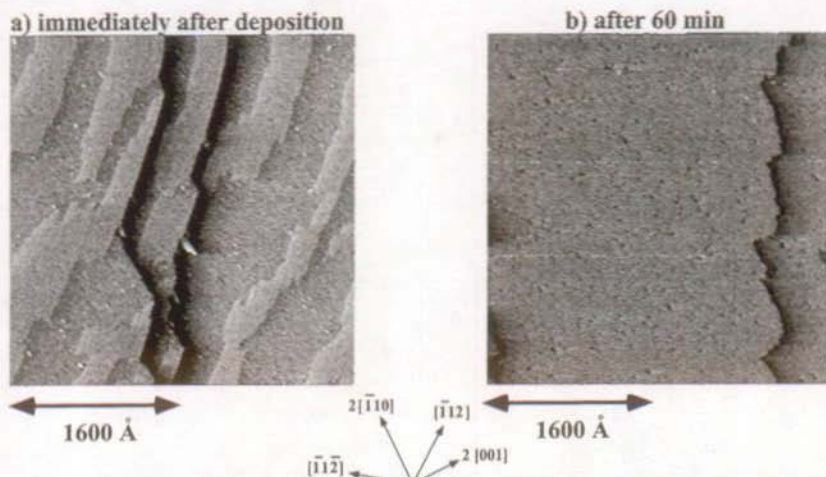[$\bar{1}1\bar{2}$]   2 [001]

Fig. 5.9: a) Crystalline silicide islands formed on Pd(110) after 0.4 ML Si deposition at 550 K. The STM image has been taken immediately after deposition. b) The same surface 60 min after the deposition while keeping the temperature at 550 K.

The RAIR spectra on figure 5.10 prove that the dissolution of the silicide is not a local effect associated with the limited image field of the STM. The infrared experiment is an integral probe sampling the entire macroscopic surface. It is clearly seen that the vibrational band at 2074 cm^{-1} (characteristic for the presence of Si at the surface) disappears completely when the surface is kept at 550 K for 60 min, while the Pd peak at 2000 cm^{-1} has gained intensity (figure 5.10.c). Thus, the vibrational spectra demonstrate that within experimental error the entire surface is completely Pd terminated and that Si has diffused subsurface. It is however important to note that the Si disappearing from the surface does not migrate completely into the bulk. This behavior is revealed by Auger spectroscopy showing that the Si AES peak does not disappear completely within several hours and indicating the presence of the silicon in the selvedge just beneath the surface.
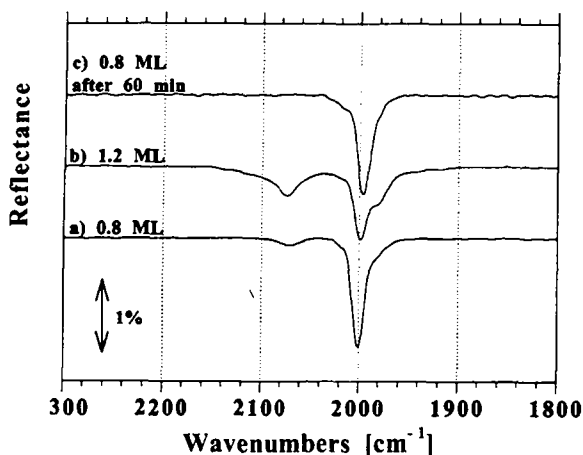
Fig. 5.10: Infrared spectra of one monolayer CO adsorbed on the palladium-silicide/Pd(110) surface. Si deposition of 0.8 ML (a) and 1.2 ML (b) at 550 K. The spectrum in (c) corresponds to the situation of figure 5.9.b where the surface was kept 60 min at 550 K after Si deposition.

5.4. Discussion

From STM images we evaluated the area covered by crystalline silicide as a function of Si coverage at 400 K, 500 K and 550 K (figure 5.11.a). At each temperature, the amount of surface silicide seems to grow linearly with the Si coverage. The STM images shown in figure 5.11.b are taken directly after deposition of 0.4 ML Si at 400 K, 500 K and 550 K, respectively. Obviously, the amount of silicide, which is formed at the substrate surface, is different. The surface area which is covered with silicide grown at 550 K, is about twice as large as the silicide area grown at 400 K and 500 K. We observe a pronounced formation of surface silicide at 550 K indicating an increase in silicide reaction at the surface at the expense of subsurface diffusion with increasing temperature. The amount of Si buried below the surface may be estimated as follows: from the STM image in figures 5.6.b (or 5.11.b.3) we know that 1.2 ML Si deposited at 550 K is transformed into about one layer of surface silicide. We take into account the stoichiometry of Pd_2Si as discussed above. In this case 0.5 ML of the deposited Si is necessary to create one layer of surface silicide (as on the model of figure 5.7.b) and 0.7 ML is missing at the surface. This estimation directly leads to the

74

a) 1.2

- o -	400 K
- □ -	500 K
- ■ -	550 K

Silicide layer
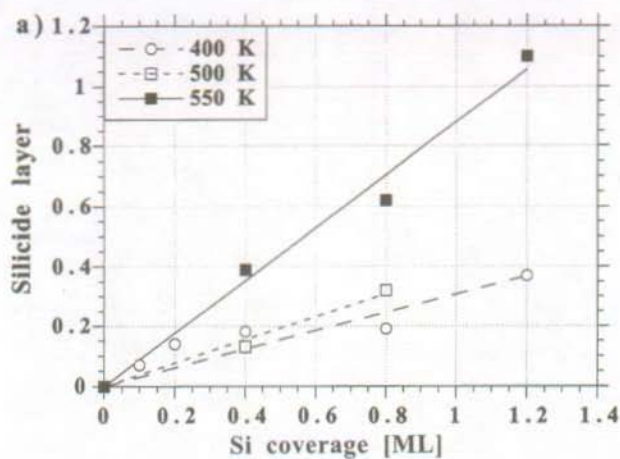
Si coverage [ML]

b.1) 0.4 ML, 400 K

1200 Å

b.2) 0.4 ML, 500 K

1600 Å

b.3) 0.4 ML, 550 K

1600 Å

$2[\bar{1}10]$

$[\bar{1}12]$

$[\bar{1}1\bar{2}]$

$2[001]$

Fig. 5.11: a) Surface area covered with crystalline silicide as a function of the Si coverage for the deposition temperatures of 400 K, 500 K and 550 K. b) STM images taken immediately after deposition of 0.4 ML Si at the indicated temperatures.

75

conclusion that more than half of the deposited Si is buried below the surface directly after deposition at 550 K. At 400 K and 500 K the fraction of subsurface Si is of the order of 75% since 1.2 ML Si deposited gives about 0.4 ML silicide layer which requires only 0.2 ML of Si.

The observed growth scenario can be understood qualitatively in the following picture (see diagram in figure 5.12). Si deposited on the Pd surface has two reaction channels leading to the global and to the local energy minimum of the system. The local minimum is reached via silicide reaction at the surface, but this state is found to be unstable at elevated temperatures. After decomposition of all silicide islands a flat, Pd terminated surface is left. Thus the energetic ground state of the system is the mixing of Si in the selvedge of the Pd substrate. This state is achieved through subsurface diffusion of the Si atoms via a Si-Pd exchange mechanism. As both processes, chemical reaction and subsurface diffusion were observed to be thermally activated processes, the corresponding reaction rates will depend exponentially on their respective activation barriers. At very low temperatures both reaction channels are frozen and unreacted Si nucleates at the surface. With increasing temperature the reaction channel with the lowest energy barrier becomes active first. Reaching a certain temperature also the higher energy barrier can be overcome and the population of the second minimum via the second channel will be observed. Since the nucleation of the silicide islands is only possible by Si atoms penetrating into the substrate, it is most likely that the barrier for interdiffusion is lower than the chemical activation energy for silicide formation. The efficient formation of surface silicide at 550 K confirmes the assumption. Thus, with increasing temperature subsurface diffusion becomes active first. Only at elevated temperatures silicide formation becomes significant; first amorphous then crystalline silicide is formed.

It must be noted that the observed crystalline Pd_2Si structure (model in figure 5.7.b) does not correspond to the previously known structure that epitaxially grows on Si(111) (see § 5.1) [10, 31]. The structure found in our experiment where we deposit Si on Pd(110) at $T \geq 350$ K is new and not stable at deposition temperature. Because the silicide phase is not the global

minimum, the only way to stabilize the formed silicide is the rapid quenching below the threshold for bulk diffusion (see figure 5.12).
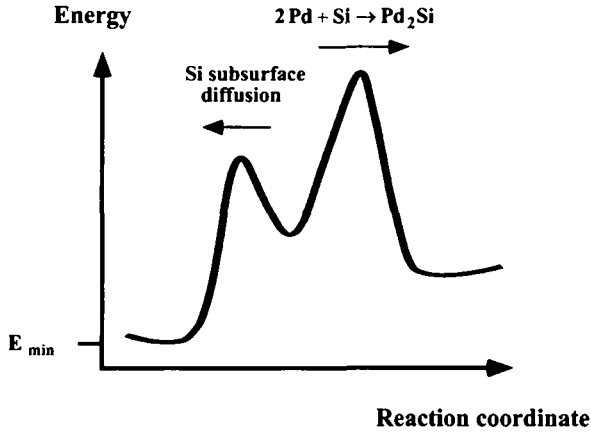

Fig. 5.12: Schematic potential diagram describing the Si/Pd(110) system.

From the early work of S. Okada et al. [10] it is already known that the volume phase diagram of Si/Pd fails in describing processes which proceed at the surface. In the case of Pd deposited on the Si substrate the deposit diffuses into the bulk although there is no miscibility indicated in the phase diagram. Later work from S. Nishigaki et al. confirmed these results [34]. Silicon on Pd(110) constitutes another example for the surface mixing of elements, which are immiscible in the bulk. Recent theoretical analysis suggests that surface mixing is expected generally in systems which are dominated by atomic size mismatch [35, 36]. While the mismatch renders the elements immiscible in the bulk, the reduced strain energy at the surface will cause a finite miscibility there. An interesting difference between the present system and the previously studied systems [13-16] is the fact that for Si/Pd(110) the intermixing is not confined to the topmost surface layer but rather to the first few layers just beneath the surface.

5.5. CO adsorption on Si/Pd(110)

In this paragraph we present the absorption spectra of CO adsorbed on Si/Pd(110) at room temperature (§ 5.5.1) and high temperature (T ≥ 350 K) (§ 5.5.2) in relation to the morphology observed by STM in § 5.3.

5.5.1. Room temperature grown silicide

In figure 5.13 are displayed the absorption spectra of CO on the reacted layers after Si deposition at 300 K on Pd(110). In the spectrum obtained after 0.4 ML Si deposition, the vibrational band at 2000 cm^{-1} characteristic for CO on Pd(110) is dominating. This Si amount reacted on the surface is too small to change the IR spectrum. It indicates that an important proportion of Si atoms has diffused subsurface (the spectrometer is sensitive to ~ 0.1 ML at the surface). With further Si deposition, the band at 2090 cm^{-1} increases (0.8 ML, 1.2 ML) whereas the band at 2000 cm^{-1} decreases. It means that Si reacts to form amorphous silicide clusters distributed at the surface as visible in figure 5.3.a; this morphology explains why the bands are relatively broad. A closer inspection of the spectrum after deposition of 1.2 ML Si reveals a small shoulder around 2104 cm^{-1}, indicating that a fair amount of unreacted Si is already present at the surface. With a Si coverage of 1.8 ML, the band has shifted to 2097 cm^{-1} indicating that the additional Si stays unreacted at the surface. The surface morphology has also changed: large white patches replace the small clusters (figure 5.3.b). At the coverage of 2.4 ML the silicide is hardly visible whereas at 3.6 ML only unreacted Si is visible and the substrate is totally hidden.
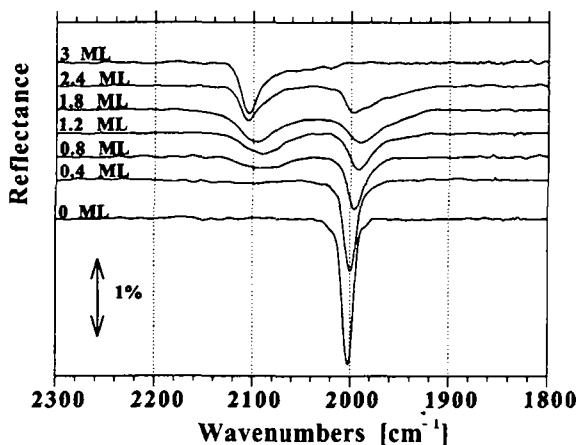

Fig. 5.13: A series of infrared spectra of one monolayer CO adsorbed on palladium-silicide grown at 300 K. The amount of deposited Si is indicated. One monolayer CO was reached after dosing 40 L CO at 100 K.

5.5.2. High temperature (350 - 550 K) grown silicide

<u>5.5.2.1. CO adsorption</u>

In this paragraph the absorption spectra of CO adsorbed on crystalline Pd silicide will be presented. The crystalline structures of the silicide grown at 400 K and 550 K are identical as already observed by STM (figures 5.5.b and 5.6) and LEED (§ 5.3.2.3). Consequently the RAIR spectra of adsorbed CO are also quite similar (figures 5.1.b.3 and b.4). Therefore we restrict ourselves to the discussion of the spectra at 550 K presented in figure 5.14. For a better interpretation of the spectra, the integrated band intensities relative to the whole integrated spectrum are plotted as a function of Si coverage in figure 5.15. The following discussion refers to both figures (5.14 and 5.15).
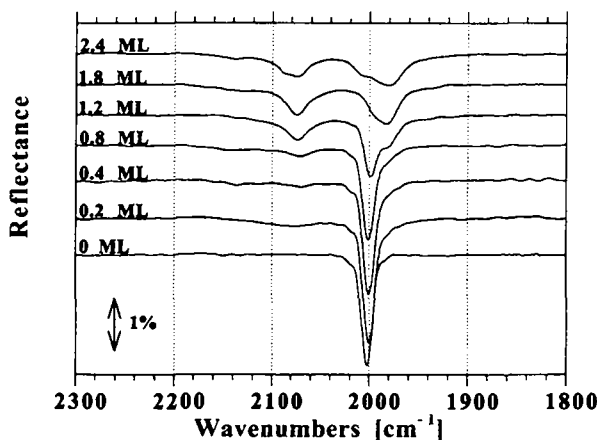

Fig. 5.14: The infrared spectra of one monolayer CO adsorbed on palladium-silicide grown at 550 K. The amount of deposited Si is indicated. One monolayer CO was achieved after dosing 40 L CO at 100 K.

The bottom spectrum of figure 5.14 (0.2 ML Si deposited) is dominated by the absorption band at 2000 cm^{-1} corresponding to CO adsorbed in bridge configuration on Pd atoms of the uppermost layer (compare with figure 5.1.c). The submonolayer Si deposition is accompanied by the appearence of a second absorption band at 2074 cm^{-1}. The intensity of the absorption at 2074 cm^{-1} increases with increasing Si dosage while the intensity of the initial absorption at 2000 cm^{-1} slowly decreases. This means that the crystalline silicide islands cover

progressively the Pd(110) surface (see figures 5.5.b.1 - b.3 and 5.6.a - b). Upon completion of the silicide monolayer (figure 5.6.b), the intensity of the high frequency absorption saturates. The maximum value of its relative intensity with respect to the integrated absorption of the whole spectrum amounts to about $I_{rel} \approx 40\%$ indicating that a large number of CO molecules still adsorbs on the crystalline silicide layer in bridge position over adjacent Pd atoms. There is no significant frequency shift due to silicide formation.
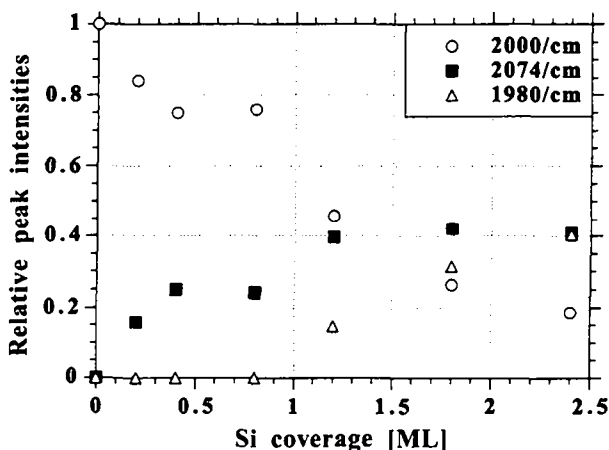

Fig. 5.15: Integrated peak intensities relative to the whole integrated spectra as a function of Si coverage. The band at 2000 cm^{-1} is assigned to CO adsorbed in bridge position on Pd atoms, the band at 2074 cm^{-1} refers to crystalline silicide and the one at 1980 cm^{-1} to Pd atoms of the second silicide layer.

With the onset of the silicide growth in the second layer, a third band appears as a low frequency shoulder of the main absorption peak at 2000 cm^{-1}. A deconvolution reveals a peak maximum at 1980 cm^{-1}. With increasing Si deposition the intensity of this absorption increases at the expense of the absorption at 2000 cm^{-1}. After deposition of more than 2 ML Si, this band dominates the spectrum. Since this absorption band is observed with the silicide growth in the second layer and since the absorption around 2000 cm^{-1} decreases simultaneously, it is possible to assume that this band is due to CO molecules adsorbed on the Pd atoms in the second silicide layer. The frequency indicates also a bridge position. The chemical red-shift of 20 cm^{-1} is reasonable because the Pd atoms in the first silicide layer are mainly bound to Pd atoms of the bulk whereas the Pd atoms of the second layer are

exclusively surrounded by silicide. In the uppermost spectrum of figure 5.14 after deposition of 2.4 ML, a small shoulder around 2100 cm^{-1} arises indicating the onset of the unreactive Si growth on top of the silicide layer. In the STM image it appears as white patches (see figure 5.6.d)

5.5.2.2. CO desorption

We now turn to the assignment of the absorption at 2074 cm^{-1} observed in spectra of adsorbed CO on crystalline silicide (figure 5.1.b.3 and b.4 and figure 5.14 upper spectra). We made thermal desorption experiments in order to clarify the origin of this mode. The infrared spectra in figure 5.16 represent the CO molecules remaining from a silicide surface prepared by depositing 2.4 ML Si at 400 K. The CO molecules corresponding to the small shoulder at ≈ 2100 cm^{-1} are the species which desorbs first. The temperature of about 200 K corresponds to CO desorbing from the reconstructed Si(100)-(2 × 1) surface. Consequently a small amount of unreacted Si already exists in the third silicide layer grown at 400 K (as at 550 K). Upon further annealing the intensities of the remaining two absorption bands at 2074 cm^{-1} and 2000 cm^{-1} decrease slowly. At an annealing temperature of 300 K both absorptions are still visible. Complete desorption takes place above 300 K. This temperature roughly coincides with the measured desorption of CO from the Pd(110) surface [24]. Since the band at 2074 cm^{-1} decays at about 300 K, well above the desorption temperature of CO/Si(100), it is likely that the corresponding CO species is also bound to Pd atoms. For the assignment of the absorption at 2074 cm^{-1} we consider the two most likely adsorption configurations: 1) a bridge-bound CO molecule above a mixed Si-Pd adsorption site and 2) a CO molecule in an on-top position over a Pd atom in the silicide. The occupation of a mixed adsorption site has already been observed for CO/CuNi(111) [37]. The resonance frequency of CO adsorbed in a mixed adsorption site would be expected between 2000 cm^{-1} (CO/Pd(110) bridge) and 2081 cm^{-1} (CO/Si(100) bridge) which would be consistent with the absorption at 2074 cm^{-1}. However, this peak frequency agrees also very well with the measured IR absorption (between 2060 cm^{-1} and 2090 cm^{-1}) of CO linearly bound on top of the Pd atoms of the (110) surface [23, 24]. Thus, an unambiguous assignment of the 2074 cm^{-1} mode of CO on the palladium-silicide is

not possible. Further investigations especially of the atomic structure of the grown silicide will be helpful.
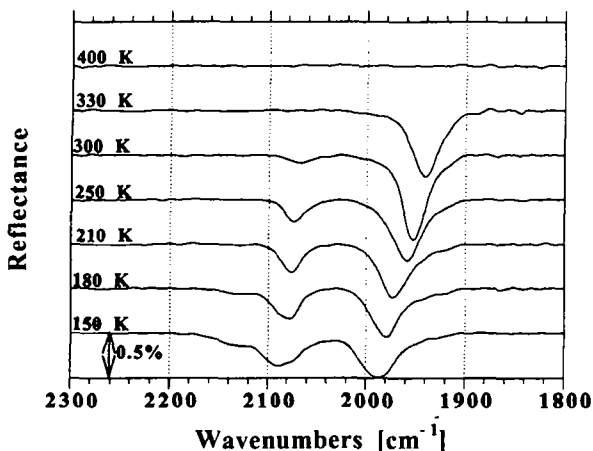

Fig. 5.16: The infrared spectra of CO adsorbed on palladium-silicide grown at 400 K upon deposition of 2.4 ML Si and after annealing the CO layer at the indicated temperatures.

5.5.2.3. Adsorption site model

In figure 5.17 a hard-sphere model is displayed which shows the possible adsorption sites of CO on palladium-silicide (Pd_2Si) modeled in figure 5.7.b (domain -). Each sphere is scaled with the respective Van-der-Waals radius. We assume that CO (small hatched spheres) will adsorb on this crystalline silicide the same way as it does on a bare Pd(110) surface i.e. in bridge configuration over two adjacent Pd atoms in a zigzag pattern [24, 38]. Each silicide cell thus contains 4 CO molecules. We note that one of those four CO molecule is mainly influenced by the incorporated Si atom. This is indicated by the overlap of the spheres of the Si atoms and the CO molecules. The strong interaction may lead to a configuration change and consequently to a change in the resonance frequency of the involved CO molecule.

With regard to figure 5.17, 75% of the adsorbed CO molecules are unaffected and remain in bridge position over adjacent Pd atoms of the silicide layer. Their resonance frequency is expected to be at 2000 cm^{-1}. About 25% of the integrated absorption will appear in a second

band corresponding to 2074 cm^{-1}. This is in good agreement with the measured infrared intensities at saturation (figure 5.15) and it justifies our model.
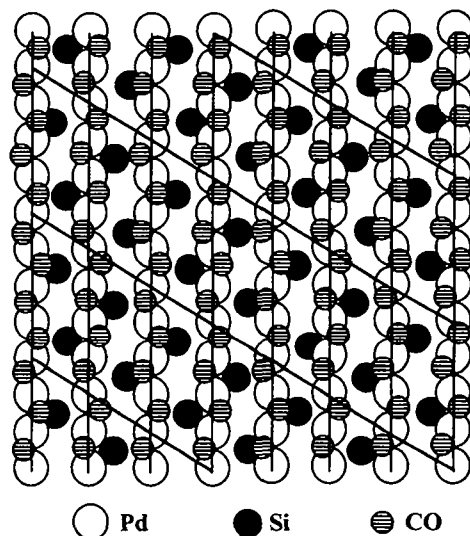

Fig. 5.17: Hard-sphere model of adsorption sites of CO on crystalline Pd$_2$Si. Each sphere is scaled with the respective Van-der-Waals radius.

5.6. References

[1] V. G. Lifshits, A. A. Saranin and A. V. Zotov, *Surface Phases on Silicon: Preparation, Structures, and Properties*, Wiley, Chichester (1994).
[2] J. M. Poate, K. N. Tu and J. W. Mayer, *THIN FILMS- INTERDIFFUSION AND REACTIONS*, Wiley, New York (1978).
[3] P. A. Benett and B. DeVries, *Layerwise Reaction at a Buried Interface*, Phys. Rev. Lett. **69**, 2539 (1992).
[4] S. P. Murarka, *Silicides for VLSI Applications*, Academic Press, Orlando (1983).
[5] X. Tong and J. M. Gibson, *Observation of dislocation-mediated layer-by-layer interface growth*, Appl. Phys. Lett. **65**, 168 (1994).
[6] M. C. Muñoz, F. Soria and J. L. Sacedon, *THE INTERACTION OF Si WITH Al(111) SURFACES ABOVE ROOM TEMPERATURE*, Surf. Sci. **189/190**, 204 (1987).
[7] A. Franciosi, D. W. Niles, G. Margaritondo, C. Quaresima, M. Capozi and P. Perfetti, *Au-Si interface formation: The other side of the problem*, Phys. Rev. B **32**, 6917 (1985).
[8] M. A. Chester and A. B. Horn, *The deposition of silicon on metal single-crystal surfaces, studied by RAIRS, LEED an AES*, J. Phys.: Condens. Matter **3**, S251 (1991).
[9] K. Nishimori, H. Tokutaka, H. Sumi and N. Ishihara, *Silicide Reaction of Si Thin Film Deposited on Platinum Metal*, J. Vac. Soc. Japan **34**, 143 (1991).
[10] S. Okada, K. Oura, T. Hanawa and K. Satoh, *A LEED-AES STUDY OF THIN Pd FILMS ON Si(111) AND (100) SUBSTRATES*, Surf. Sci. **97**, 88 (1980).
[11] W. G. Moffat, *Handbook of binary phase diagram*, Genium Publ. Company, Schenectady (1987).
[12] R. P. Elliot, *Constitution of Binary Alloys, First Supplement*, McGraw Hill, New York (1965).
[13] B. Mutaftschiev and A. Bonissent, *ADSORPTION ET CONDENSATION EN COUCHES MIXTES: I. PROPRIETES DES ISOTHEREMES*, Surf. Sci. **34**, 649 (1973).

[14] L. P. Nielsen, F. Besenbacher, I. Stensgaard and E. Laegsgaard, *Initial Growth of Au on Ni(110): Surface Alloying of Immiscible Metals*, Phys. Rev. Lett. **71**, 754 (1993).

[15] H. Röder, R. Schuster, H. Brune and K. Kern, *Monolayer-Confined Mixing at the Ag-Pt(111) Interface*, Phys. Rev. Lett. **71**, 2086 (1993).

[16] R. M. Tromp, A. W. Denier van der Gon and M. C. Reuter, *Surface Stress as a Driving Force for Interfacial Mixing*, Phys. Rev. Lett. **68**, 2313 (1992).

[17] W. Ehrley, R. Butz and S. Mantl, *External infrared reflection absorption spectroscopy of methanol on an epitaxially grown Si(100)2x1 surface*, Surf. Sci. **248**, 193 (1991).

[18] T. Sakurai and H. D. Hagstrum, *Study of clean and CO-covered Ge(111) surfaces by photoemission and ion- neutralization spectroscopies*, Phys. Rev. B. **20**, 2423 (1979).

[19] J. P. Chamberlain, J. L. Clemons, A. J. Pounds and H. P. Gillis, *Adsorption of CO on Si(100)-(2x1) at room temperature*, Surf. Sci. **301**, 105 (1994).

[20] Y. Bu and M. C. Lin, *Interaction of CO with silicon single-crystal surfaces studied by HREELS, UPS and TPD*, Surf. Sci. **298**, 94 (1993).

[21] M. A. Chester, G. S. McDougall, M. E. Pemble and N. Sheppard, *THE CHEMISORPTION OF CO ON Pd(110) AT 110 AND 300 K STUDIED BY ELECTRON ENERGY LOSS SPECTROSCOPY*, Surf. Sci. **164**, 425 (1985).

[22] A. Locatelli, B. Brena, S. Lizzit, G. Comelli, G. Cautero, G. Paolucci and R. Rosei, *Adsorption Site Determination by Means of Surface Core Level Shift High Energy Photoelectron Diffraction: Pd{110}(2x1)p2mg-CO*, Phys. Rev. Lett. **73**, 90 (1994).

[23] R. Raval, M. A. Harrison and D. A. King, *TEMPERATURE EFFECTS IN COMPRESSION STRUCTURES: CARBON MONOXIDE ON Pd(110) BY RAIRS*, Surf. Sci. **211/212**, 61 (1989).

[24] E. Hahn, E. Kampshoff and K. Kern, *Surface stress effects in chemical activation*, Chem. Phys. Lett. **223**, 347 (1994).

[25] U. K. Köhler, J. E. Demuth and R. J. Hamers, *Surface Reconstruction and the Nucleation of Palladium Silicide on Si(111)*, Phys. Rev. Lett. **60**, 2499 (1988).

[26] L. Casalis, C. Casati, R. Rosei and M. Kiskinova, *Surface structure of some stages preceding formation of a Pd2Si phase*, Surf. Sci. **331-333**, 381 (1995).

[27] E. Kampshoff, N. Waelchli, A. Menck and K. Kern, *Hydrogen-induced missing-row reconstructions of Pd(110) studied by scanning tunneling microscopy*, Surf. Sci. **360**, 55 (1996).

[28] L. P. Nielsen, F. Besenbacher, E. Laegsgaard and I. Stensgaard, *Nucleation and growth of a H-induced reconstruction of Ni(110)*, Phys. Rev. B **44**, 13156 (1991).

[29] H. Brune, H. Röder, C. Boragno and K. Kern, *Strain relief at hexagonal-close-packed interfaces*, Phys. Rev. B **49**, 2997 (1994).

[30] G. Ertl and J. Küppers, *Low Energy Electrons and Surface Chemistry*, VCH, Weinheim (1985).

[31] H. Roux and N. Boutaoui, *AES quantitative interpretation of the first stages of Pd2Si formation during Pd adsorption on Si(111) at room temperature*, Surf. Sci. **260**, 113 (1992).

[32] J. Angilello, F. d'Heurle, S. Peterson and A. Segmüller, *Observations of stresses in thin films of palladium and platinum silicides on silicon*, J. Vac. Sci. Technol. **17**, 471 (1980).

[33] P. P. Buaud, F. M. d'Heurle, S. Chevacharoenkul and E. A. Irene, *In situ strain measurements during the formation of palladium silicide films*, J. Vac. Sci. Technol. B **11**, 304 (1993).

[34] S. Nishigaki, T. Komatsu, M. Arimoto and M. Sugihara, *INITIAL STAGE OF Pd ADSORPTION ON Si(111)7x7 SURFACE STUDIED BY AES AND EELS*, Surf. Sci. **167**, 27 (1986).

[35] J. Tersoff, *Surface-Confined Alloy Formation in Immiscible Systems*, Phys. Rev. Lett. **74**, 434 (1995).

[36] M. Schmid, W. Hofer and P. Varga, *Surface stress, surface elasticity, and the size effects in surface segregation*, Phys. Rev. B **51**, 10937 (1995).

[37] E. Garfunkel, M. Yu, S. Yang and X. Feng, *A mixed Cu-Ni bridge site for CO adsorption*, J. Vac. Sci. Technol. A **7**, 1579 (1989).

[38] E. Hahn, *STRUCTURE AND REACTIVITY OF VICINAL Pt AND LOW-INDEX Cu/Pd SURFACES*, THESE N° 1218, EPFL (1994).

6. Reactions at the Si/Pd(100) interface

The heterogeneous Si/Pd(100) system has been investigated by STM and RAIRS in the temperature range 100 K ≤ T ≤ 600 K. Several similarities between Si deposition on Pd(110) and (100) have been observed: critical temperature for silicide reaction (T ≥ 150 K), Si-Pd exchange mechanism, Si subsurface diffusion. But in contrast to the Si/Pd(110) system, no crystalline silicide phase could be grown at the Pd(100) surface. In order to account for the different densities of the (110) and (100) Pd faces, the monolayer is now defined as: $1 \, ML_{(100)} = \sqrt{2} \, ML_{(110)}$ (see figures 2.5 and 2.6).

6.1. Basic experimental observations

6.1.1. Silicide formation on the Pd(100) surface as a function of temperature

Figure 6.1.a shows the spectrum of one monolayer CO adsorbed on 2.5 ML Si deposited on Pd(100) at 100 K. The CO/Si/Pd(100) layers are then annealed at 150, 200, 250 and 300 K for 2 min and cooled back to 100 K for each IR measurement. The obtained RAIR spectra are displayed in figure 6.1.b - e. The diffuse LEED pattern indicates each time an amorphous surface morphology. The bottom spectrum shows a single absorption band at 2106 cm^{-1}. This band is already known from CO adsorption onto amorphous silicon (figure 5.1.a, b.1). Thus we deduce that amorphous Si has grown on the Pd(100) surface, covering it completely. This deduction is confirmed by AES which gives a single peak at 92 eV characteristic for Si [1]. Upon annealing the sample to 150 K, a new band appears at 1979 cm^{-1} while the band at $\approx$ 2100 cm^{-1} loses intensity. The position of the new band indicates that it is due to CO adsorbed in bridge configuration over 2 Pd atoms. The absorption spectra of CO on Pd(100) as a function of the CO exposure is presented in the next paragraph.

Two possible explanations can account for the appearence of the band at 1979 cm^{-1}: either Si forms 3D clusters and Pd substrate is uncovered or a certain amount of Pd diffuses through the a-Si layer up to the surface. The AES measurement gives a multiple peak shape around 92 eV which indicates that Si atoms have reacted to form palladium-silicide (most probably Pd_2Si) [1]. So we conclude that the second explanation is correct to explain the RAIRS data. The band centered at 1979 cm^{-1} is quite broad (33 cm^{-1} linewidth) indicating that small

patches of Pd atoms have mixed with Si on the surface and are randomly distributed. The band at ≈ 2100 cm^{-1} does not shift substantially upon silicide formation. At 200 K the intensity of the vibrational band around 2100 cm^{-1} decreases while the intensity of the second absorption band increases indicating that the amount of Pd atoms in the topmost layer increases. At 250 K the band at ≈ 2100 cm^{-1} has almost disappeared and a small band at 2081 cm^{-1} remains. Above 300 K complete desorption takes place. The formation of silicide upon Si deposition on Pd(100) takes place for T $\geq$ 150 K. The temperature coincides with the silicide formation temperature on the Pd(110) substrate (§ 5.2.1).
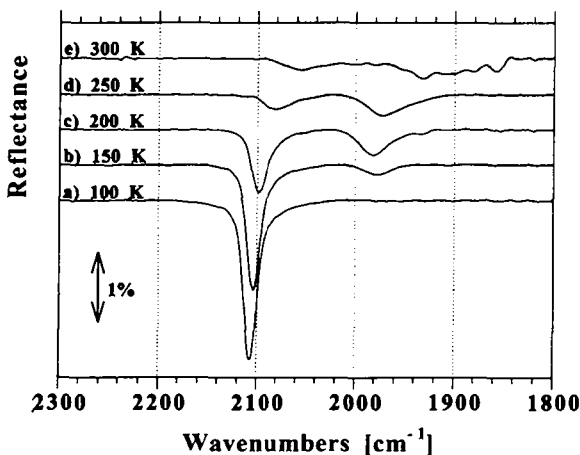

Fig. 6.1: a) Infrared spectrum of one monolayer CO adsorbed on 2.5 ML Si deposited on Pd(100) at 100 K. (CO exposure: 40L.) b - e) The CO/Si/Pd(100) layers were annealed at the indicated temperatures for 2 min and cooled back to 100 K for RAIRS measurements.

6.1.2. CO adsorption on Pd(100)

The RAIR spectra of CO adsorbed on Pd(100) as a function of the CO exposure have been measured in order to determine the adsorption configuration at high CO coverage. It is known that CO adsorbs on Pd(100) predominantly in bridge configuration over adjacent Pd atoms. The occupation of the on-top sites is also observed from CO saturation coverage. RAIR spectra revealing these two adsorption sites have already been measured at 150 K [2] and at 300 K [3]. The spectra displayed in figure 6.2 show a CO adsorption series at 150 K. The exposure of 0.4 L CO reveals a broad band at 1937 cm^{-1} in the RAIR spectrum. The intensity

of this band increases and the maximum shows a pronounced blue-shift upon further exposure. At a 2 L CO exposure, a second band at 2099 cm^{-1} appears. The assignment of the two bands is as follows: the low frequency mode (now at 1987 cm^{-1}) is due to the CO molecules adsorbed over two adjacent Pd atoms in twofold bridge position, the high frequency mode is due to CO adsorbed on-top of Pd atoms, most probably located at domain boundaries. A larger exposure does not substantially change the shape of the CO absorption spectra. The integrated intensity of the peak at 2099 cm^{-1} amounts to about 10% of the total integrated spectrum (see figure 6.8 in § 6.3.1).

The CO coverage dependent frequency shift of the low frequency mode (CO in bridge position) amounts +50 cm^{-1} between 0.4 L and 2 L. This positive shift is a superposition of the dipole and the chemical shift (see § 2.2.2).

The appearance of the band at 2099 cm^{-1} is due to CO molecules which adsorb in on-top configuration at domain walls between the $(n\sqrt{2} \times \sqrt{2})R45°$ (n = 2, 3, 4) structures at coverages > 0.50 ML [2, 4]. In the following we have to account for this band since the absorption maximum unfortunately matches with the peak maximum of CO adsorbed on amorphous Si (figure 5.1.a, b.1).
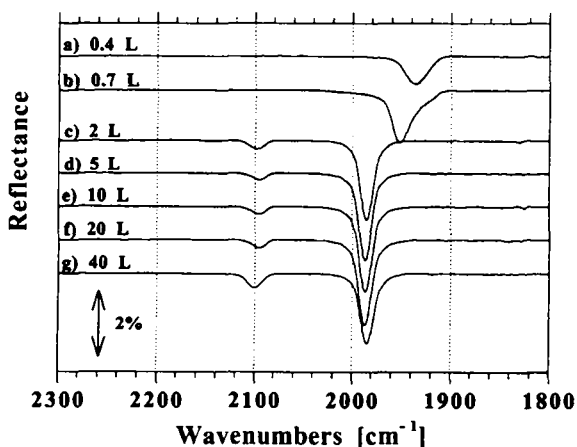

Fig. 6.2: RAIR spectra of CO adsorbed on Pd(100) as a function of exposure at 150 K.

6.2. Growth morphology of amorphous silicide

The surface morphology of Si deposited on Pd(100) at 200 K ≤ T ≤ 600 K is studied by variable temperature STM. At 200 and 300 K a high density of small amorphous embedded clusters nucleates in the topmost Pd layer. RAIR measurements indicate that the chemical character of the Si atoms in the silicide layer is most similar to the one of unreacted amorphous Si (see § 6.3.2). At 400 and 500 K, in addition to these clusters, silicide adislands resulting from the reaction of Si atoms with ejected Pd atoms are created. These Pd adatoms are most probably due to exchange mechanisms between Si and Pd when the Si atoms penetrate into the substrate during the formation of the embedded clusters. At 600 K the adislands are no longer visible. Due to the high mobility of the adatoms on the terraces, the nucleation of the adislands takes place at step edges.

6.2.1. Amorphous silicide clusters at 300 K

In figure 6.3 a series of STM images is displayed characterizing the growth morphology of silicide on the Pd(100) surface at 300 K. We notice that the deposition of 0.15 ML leads to the formation of a high density ($\approx 6 \times 10^{-3}$ ML) of uniformly distributed small clusters (diameter 5 - 10 Å) more or less implanted in the surface. A STM image in grey-scale height representation reveals that these clusters emerge from the surface with variable heights between 20% and 80% of the Pd(100) step height (1.95 Å [5]). Upon further Si deposition (0.3 ML) the cluster density and their average width remain constant: the growth is three-dimensional. At Θ_{Si} = 1.7 ML a very rough surface is observed. The corrugation varies and can reach one Pd(100) step height. With increasing Si deposition the LEED spots of the Pd(100) progressively lose intensity and the pattern become more and more diffuse indicating that the growing clusters do not have any ordered structure and are thus amorphous. The Auger spectrum shows a peak shape around 92 eV which can be considered as being mainly due to Pd_2Si. However the presence of a certain amount of unreacted Si cannot be excluded.
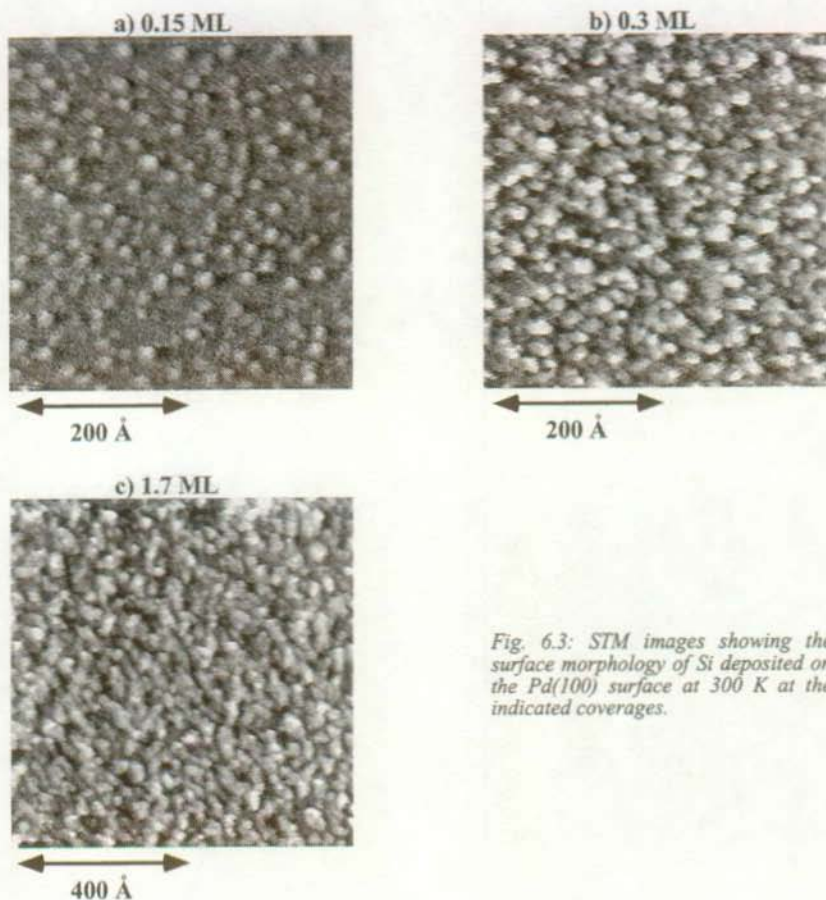
a) 0.15 ML

b) 0.3 ML

200 Å

200 Å

c) 1.7 ML

400 Å

Fig. 6.3: STM images showing the surface morphology of Si deposited on the Pd(100) surface at 300 K at the indicated coverages.

6.2.2. Silicide formation at 400, 500 and 600 K

Figure 6.4 displays STM images revealing two types of islands formed after Si depositon on Pd(100) at 400 K. The first type of islands is embedded in the substrate (hardly visible and therefore indicated by arrows in figure 6.4.a). The second type has grown on Pd(100) one step height above. These adislands are 30 - 50 Å in width. Upon further Si coverage (0.3 ML, 0.8 ML) the adisland density ($\approx 1 \times 10^{-3}$ ML) does not change substantially. These adislands become larger (up to 100 Å in width) and their height remains constant (one Pd(100) step height).

a) 0.15 ML

b) 0.3 ML
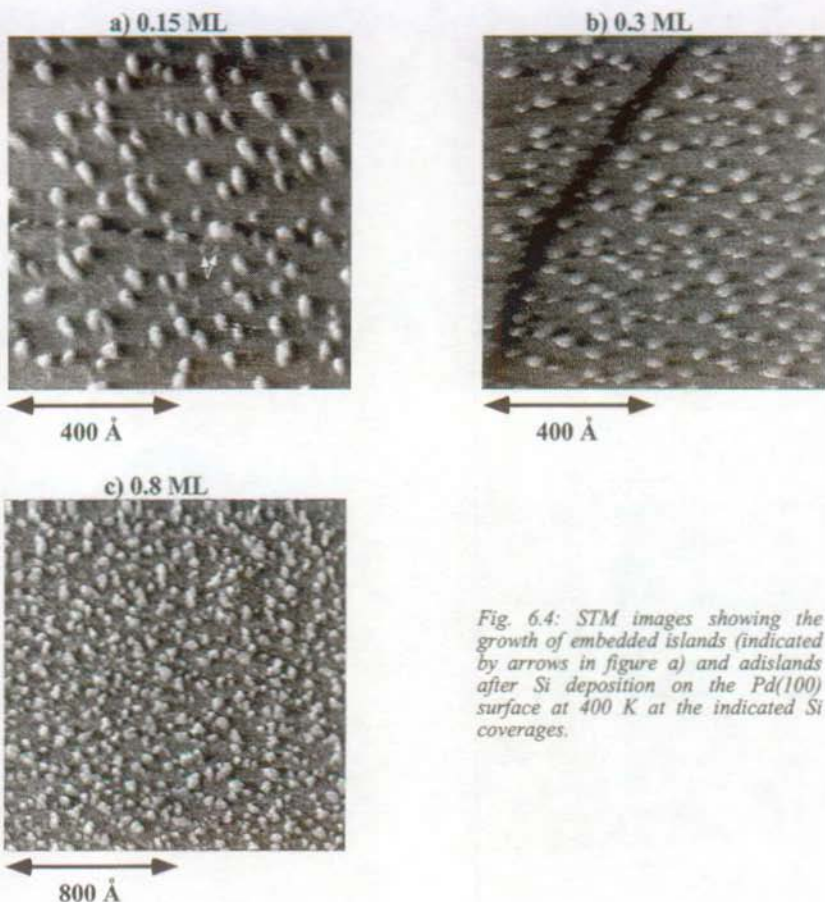
400 Å

400 Å

c) 0.8 ML

Fig. 6.4: STM images showing the growth of embedded islands (indicated by arrows in figure a) and adislands after Si deposition on the Pd(100) surface at 400 K at the indicated Si coverages.

800 Å

Figure 6.5 shows a series of STM images of Si/Pd(100) as a function of Si coverage deposited at 500 K. The surface morphology is quite similar to the one observed at the deposition temperature of 400 K. We find again two types of islands: the topmost Pd layer is covered by a large number of embedded islands. The bright patches are 10 - 20 Å in width. The adisland surfaces show the same characteristic corrugation pattern as the substrate layer. Comparing figures 6.5 and 6.4 it seems that the adislands become much larger and that their density decreases with increasing temperature. This effect may be explained by the increased

diffusion path of the adatoms. With increasing Si coverage, the number of adislands progressively increases (figure 6.5.a - c).

At 600 K silicide formation proceeds in the same way as at 400 and 500 K: impinging Si atoms penetrate the surface to form small embedded clusters or diffuse subsurface via the exchange mechanism ejecting Pd atoms onto the topmost Pd layer. The Pd adatoms react with Si adatoms to form adislands. The growth of these adislands obviously proceeds in a step-flow mode as suggested by the shape of the step edge observed in figure 6.6.a. Some impurities may hinder a perfect growth from the step edge and so it shows several bends. At higher Si coverage (figure 6.6.b, 1.7 ML), the entire terrace is covered with numerous small clusters, (10 - 20) Å in width. The corrugation varies between 30% and 50% of one step height. Increasing Si coverage does not change the morphology.

The formation of both types of islands can be explained by the same process as described in § 5.3.2.1 for Si/Pd(110): Impinging Si atoms either react with Pd substrate atoms to create the embedded islands or diffuse subsurface by ejecting Pd atoms which can then react with Si adatoms on top of the surface to create the adislands. The embedded islands formed in Pd(100) are different from those in Pd(110). The (110) surface is more open and the Si atoms can fit in the troughs at well-defined places forming crystalline silicide (model of figure 5.7.b). In Pd(100) these sites are not available and so Si must be placed in interstitial positions. This might explain the varying height of the embedded clusters in STM images (figures 6.3 - 6.6).

It must be noted that the LEED and AES measurements reveal basically the same results at all temperatures ≥ 300 K: the LEED pattern is diffuse indicating the absence of any crystalline structure and the multiple peak shape of the Auger spectra around 92 eV indicates the silicide formation [1]. RAIRS will be helpful to determine the chemical composition of the surface.

a.1) 0.3 ML

a.2) 0.3 ML

800 Å

400 Å

500 K

b) 0.8 ML
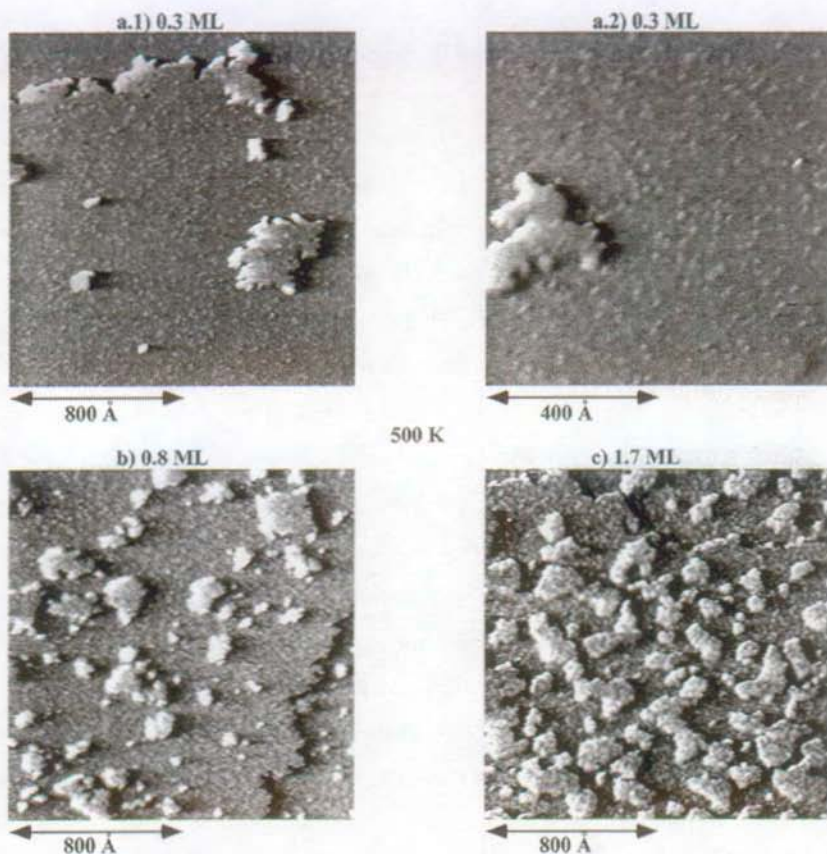
c) 1.7 ML

800 Å

800 Å

Fig. 6.5: STM images showing the growth of embedded islands and adislands after Si deposition on the Pd(100) surface at 500 K at the indicated coverages.
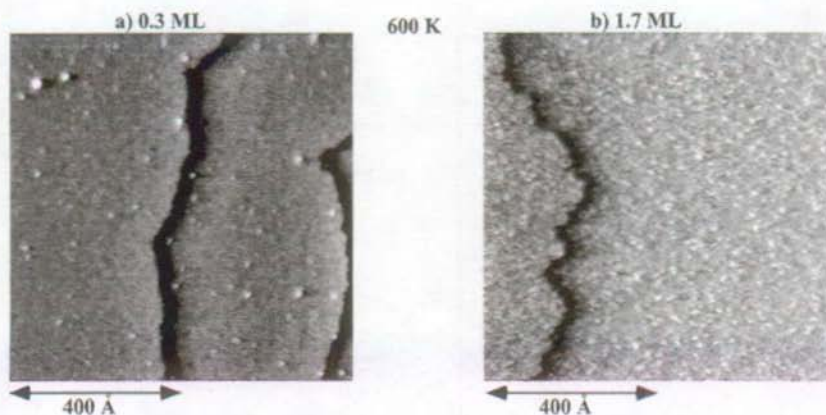
a) 0.3 ML

600 K

b) 1.7 ML

400 Å

400 Å

Fig. 6.6: STM images showing the growth morphology after Si deposition on the Pd(100) surface at 600 K at the indicated coverages.

92

6.3. CO adsorption on Si/Pd(100)

6.3.1. Adsorption spectra as a function of the CO exposure

Figure 6.7 shows a series of RAIR spectra of CO adsorbed on Si/Pd(100) at 150 K as a function of the CO exposure. 0.3 ML Si were dosed onto the substrate at 400 K. At low CO exposure only one band around 1950 cm^{-1} is seen in the IR spectra (figure 6.7.a - b). It is assigned to CO bound in bridge configuration over uncovered Pd substrate atoms as it is also measured on a bare Pd(100) surface (figure 6.2.a - b). With increasing exposure up to 20 L, a blue-shift to 1979 cm^{-1} is observed for the same reasons as on bare Pd(100) (§ 6.1.2). At 2 L CO exposure a second band appears at 2105 cm^{-1}. Band intensities and absorption maxima of both peaks do not change significantly with increasing CO exposure.
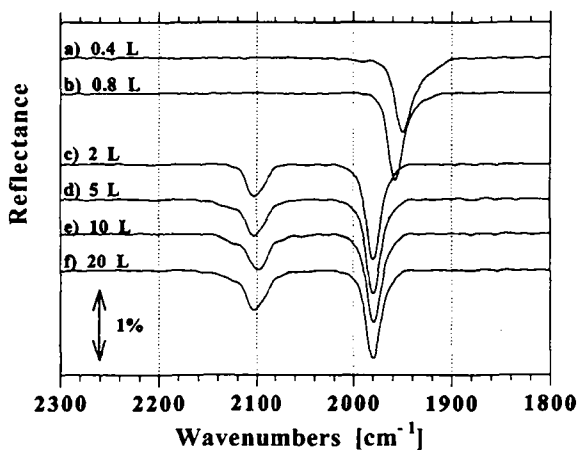

Fig. 6.7: RAIR spectra of CO on 0.3 ML Si deposited on Pd(100) at 400 K (STM image: see figure 6.4.b). The sample has been cooled down to 150 K before CO exposure.

The integrated intensity of the band at ≈ 2100 cm^{-1} relative to the whole integrated spectrum saturates at about 5 L CO exposure as shown in figure 6.8. In the same graph the relative intensity of the band at ≈ 2100 cm^{-1} obtained for CO adsorbed in on-top position on pure Pd(100) (figure 6.2) is indicated as solid triangles. Saturation also occurs at about 5 L CO exposure with a value of about 10%. Thus the silicide contribution to the absorption in

figure 6.7 is obvious: due to CO adsorption on Si of the silicide the integrated band at ≈ 2100 cm^{-1} increases from 10% to 40% of the relative integrated intensity.
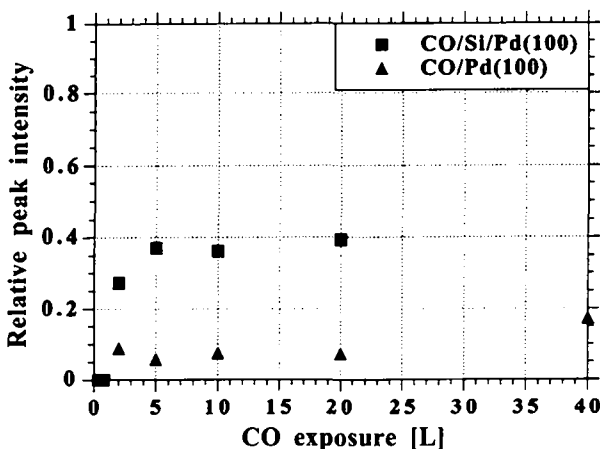

Fig. 6.8: Integrated intensity of the peak at ≈ 2100 cm^{-1} relative to the whole integrated absorption spectrum for CO adsorbed on 0.3 ML Si deposited on Pd(100) at 400 K (solid squares) and CO adsorbed on Pd(100) (solid triangles) as function of CO exposure.

It must be noted that at low CO exposure the Si band is not measurable by RAIRS (figure 6.7.a - b). Similarly to CO adsorption on Pd(100) the most favorable CO adsorption site is over two Pd substrate atoms (frequency ≈ 1950 cm^{-1}), between the clusters formed after the deposition of 0.3 ML Si at 400 K (STM image displayed in figure 6.4.b). For an exposure above 2 L, the CO atoms are forced to adsorb at domain walls on unfavorable adsorption sites. These sites are on top of Pd substrate atoms (see § 6.1.2) or in bridge position on two Si atoms. Both give the same CO absorption band at ≈ 2100 cm^{-1}. The CO absorption band around 2100 cm^{-1} is a superposition of both contributions. It is not possible to separate one contribution from the other. The RAIRS measurements have all been performed with a CO coverage of one monolayer (corresponding to exposure above 5 L) in order to detect this band at ≈ 2100 cm^{-1}.

6.3.2. CO adsorption on silicide formed at 300, 400 K

Figure 6.9 shows the RAIR spectra of one monolayer CO adsorbed on the heterogeneous Si/Pd(100) surface as a function of Si coverage deposited at 400 K.
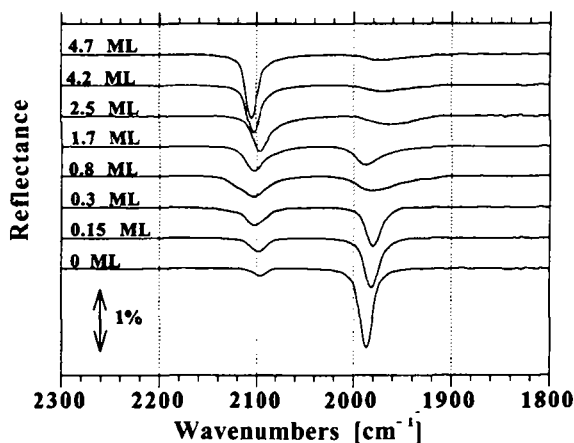
Fig. 6.9: The infrared spectra of one monolayer CO adsorbed on Si/Pd(100) as a function of Si coverage deposited at 400 K. At 150 K the surface is exposed to 20 L CO.

These spectra are quite similar to the ones obtained at 300 K. We observe two absorption bands which do not substantially shift in the whole coverage range: a low frequency mode at ≈ 1980 cm^{-1} and a high frequency mode at ≈ 2100 cm^{-1}. The former is assigned to CO adsorbed in bridge configuration over two Pd atoms of the uncovered substrate and the latter is a superposition of two contributions: CO adsorbed on Si atoms and CO adsorbed on-top of Pd atoms as dicussed in § 6.3.1. With increasing Si coverage the intensity of the band at 2100 cm^{-1} progressively increases at the expense of the intensity of the low frequency mode at 1980 cm^{-1}. At a coverage of 4.7 ML this band has almost disappeared indicating that the suface is almost entirely Si terminated.

6.3.3. CO adsorption on silicide formed at 600 K

The RAIR spectra of one monolayer CO adsorbed on Si/Pd(100) as a function of the Si coverage deposited at 600 K is presented in figure 6.10. We observe again the two absorption bands around 2100 cm^{-1} and 1990 cm^{-1} without substantial shift in the whole coverage range. At very low Si coverages, the intensity of the high frequency mode at ≈ 2100 cm^{-1} slowly increases at the expense of the low frequency mode. At about 0.8 ML the saturation coverage is reached.
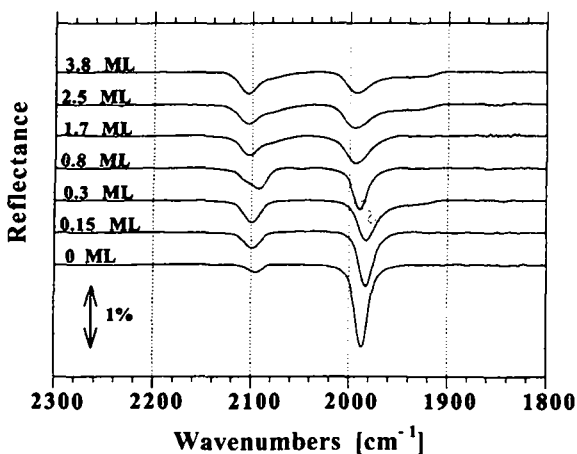
95

Fig. 6.10: The infrared spectra of one monolayer CO adsorbed on Si/Pd(100) as a function of Si coverage deposited at 600 K. The sample has been cooled down to 150 K before exposure to 20 L CO.

Figure 6.11 shows the relative integrated intensity of the band at ≈ 2100 cm^{-1} for the three different deposition temperatures as a function of Si coverage. At 600 K it saturates at 40% at coverages ≥ 0.8 ML. Increasing the Si coverage does not change the IR spectrum. In consequence, the stoichiometry of the reacted surface remains constant. The diffusion of Si and Pd through the silicide layer is thermally activated and the whole Si deposited onto the surface will react. The intensity ratio between the high and the low frequency mode is about 2/3. Taking into account the proportion of the molecules which adsorb on Pd in on-top position ($\leq 10\%$, figure 6.8) and therefore contribute to the intensity of the mode at ≈ 2100 cm^{-1}, we may conclude that the amount of CO-Si (in the silicide) and CO-Pd bound species is about 1:2. This ratio is quite similar to the ratio obtained in the case of Si/Pd(110) deposited at 550 K at saturation (§ 5.5.2.1) indicating the stoichiometry of Pd$_2$Si also on the Pd(100) surface. A similar intermixing was found to occur upon depositing Cu on Pd(100) at 600 K: between 0.6 and 1.2 ML Cu deposited, the intensity of the CO-Pd (bridge) band remains constant [2]. In contrast to the deposition at 600 K, no saturation is observed in the case of Si deposition at 300 K and 400 K indicating a continuous change of the Pd stoichiometry in the Si/Pd layer starting from pure Pd and finally reaching a completely Si terminated surface.
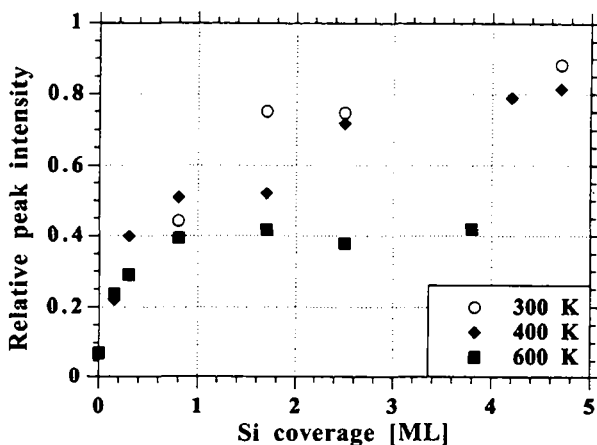
Fig. 6.11: Relative integrated intensity of the high frequency mode around 2100 cm^{-1} as a function of Si coverage for the three indicated deposition temperatures.

6.3.4. CO desorption and discussion

Si deposition on Pd(100) reveals two absorption bands at all temperatures. In order to clarify the origin of the high frequency mode at ≈ 2100 cm^{-1}, a thermal desorption experiment was performed. 1.7 ML Si is deposited at 600 K, CO is adsorbed at 150 K and the surface is subsequently annealed. The RAIR spectra are displayed in figure 6.12.

The CO molecules corresponding to the main absorption at 2105 cm^{-1} are the first desorbing species. The desorption temperature of 220 K corresponds to CO desorbing from the reconstructed Si(100)-(2 × 1) surface [6]. Obviously the chemical character of a certain amount of Si in the silicide layer is most similar to the one of unreacted Si. This is indicated by the low desorption temperature as well as by the resonance frequency which is also identical to CO/a-Si. At 220 K a broad band centered at 2090 cm^{-1} remains. This frequency is known from CO adsorbed on top of Pd atoms, slightly shifted because of the smaller CO coverage. This band is also known from CO adsorbed on amorphous silicide clusters grown on the Pd(110) surface at 300 K (see figure 5.1.b.2). At 270 K this band has slighltly shifted and lost a little intensity before desorbing completely at about 330 K.
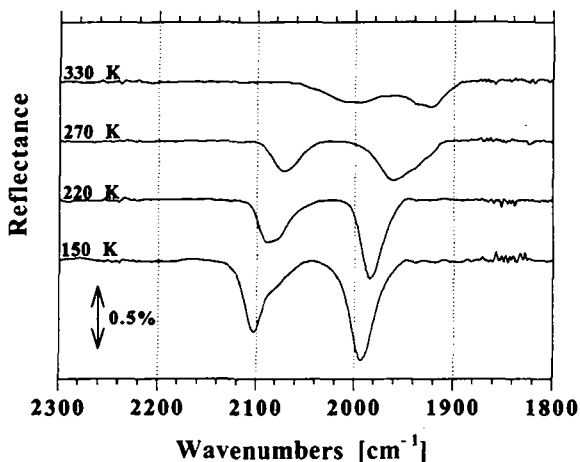
Fig. 6.12: The infrared spectra of one monolayer CO adsorbed on the palladium-silicide layer formed after deposition of 1.7 ML at 600 K (STM image: figure 6.6.b). One monolayer CO is obtained by adsorbing 20 L at 150 K (bottom spectrum). The layer is then annealed to 220 K, 270 K, 330 K for 2 min before recording the spectrum at 150 K.

The surface morphology which is revealed upon 1.7 ML Si deposition at 600 K on Pd(100) is already shown in figure 6.6.b. A rough surface with a corrugation comparable to half a step height is revealed. From RAIRS we know that the average stoichiometry is about 2 atoms Pd for 1 atom Si. The amorphous silicide formation gives a CO absorption band at ≈ 2100 cm^{-1} while one would have expected it at ≈ 2090 cm^{-1} like for Si/Pd(110) on figure 5.1.b.2. As indicated by the thermal desorption experiment of figure 6.12, the RAIR spectra consist of the *superposition of a continuous range of vibrational bands between 2090* cm^{-1} (Si in silicide) and 2100 cm^{-1} (unreacted Si). These data suggest that the silicide grows on Pd(100) as an amorphous alloy with randomly varying chemical composition. As a consequence of the dipolar interaction between the adsorbed CO (§ 2.2.2), the intensity of all the lower frequency vibrations is transferred to their higher frequency counterpart (2100 cm^{-1}). The Si peak is thus amplified and the proportion of the unreacted Si atoms in the silicide must not be overestimated.

6.4. Summary

The heterogeneous Si/Pd(100) system has been investigated by STM and RAIRS in the temperature range 100 K ≤ T ≤ 600 K. We found that the silicide reaction is activated above 150 K, the same temperature as for Si/Pd(110). The silicide formation is quite similar in both experiments, Si on Pd(110) and on Pd(100). Impinging Si atoms have two reaction channels: chemical reaction to form silicide or subsurface diffusion. In contrast to the (110) surface no crystalline silicide can be grown on Pd(100). Silicide grows on Pd(100) only in the form of a random alloy where the local environment of a Si atom is not constant. The stoichiometry of Pd_2Si given by RAIRS is an average on a large area.

6.5. References

[1] S. Okada, K. Oura, T. Hanawa and K. Satoh, *A LEED-AES STUDY OF THIN Pd FILMS ON Si(111) AND (100) SUBSTRATES*, Surf. Sci. **97**, 88 (1980).

[2] E. Hahn, *STRUCTURE AND REACTIVITY OF VICINAL Pt AND LOW-INDEX Cu/Pd SURFACES*, THESE N° 1218, EPFL (1994).

[3] A. M. Bradshaw and F. M. Hoffmann, *THE CHEMISORPTION OF CARBON MONOXIDE ON PALLADIUM SINGLE CRYSTAL SURFACES: IR SPECTROSCOPIC EVIDENCE FOR LOCALISED SITE ADSORPTION*, Surf. Sci. **72**, 513 (1978).

[4] W. Berndt and A. M. Bradshaw, *Domain wall superlattices in high coverage CO adlayers on Pd(100)*, Surf. Sci. Lett. **279**, L165 (1992).

[5] J. M. MacLaren, J. B. Pendry, P. J. Rous, D. K. Saldin, G. A. Somorjai, M. A. Van Hove and D. D. Vvedensky, *Surface Crystallographic Information Service. A handbook of Surface Structures*, D. Reidel Publishing Company, Dordrecht (1987).

[6] Y. Bu and M. C. Lin, *Interaction of CO with silicon single-crystal surfaces studied by HREELS, UPS and TPD*, Surf. Sci. **298**, 94 (1993).

7. Conclusion

A variety of atomic scale structural modifications on the palladium (110) and (100) surfaces has been produced. In that purpose we have had to control fundamental processes like hydrogen adsorption linked to bulk diffusion, epitaxy, reactive epitaxy with silicon and silicon subsurface diffusion.

Hydrogen is highly soluble in the Pd bulk [1-5]. Its adsorption on Pd(110) at 300 K is thus coupled to bulk diffusion. This involves exchange processes with substrate atoms initiating a surface reconstruction: Pd dimer chains and corresponding vacancy islands are progressively nucleating. This structural evolution can be "frozen" at any time by pumping down the hydrogen pressure. After a certain hydrogen exposure, a stationary state of hydrogen coverage is reached ending up in a missing-row reconstruction. At low hydrogen coverage, we have observed a new phase of the H/Pd(110) phase diagram, the (1×3) structure. With increasing coverage, a two-phase regime with coexisting (1×3) and (1×2) reconstructed zones is passed. At 1 ML hydrogen coverage, the surface exhibits a complete (1×2) reconstruction, a phase already known from previous work [6].

Homoepitaxial growth experiments on Pd(110) have shown that the island shape is determined by the growth kinetics. At 300 K exactly the same dimer chains as those observed at the beginning of the hydrogen-induced reconstruction are produced. Surprisingly, despite the highly anisotropic island shapes, Pd adatoms are found to diffuse rather isotropically on the surface. Isotropic adatom self-diffusion on fcc(110) has already been measured by FIM [7] and calculated [8]. For each system in-channel diffusion is thought to proceed via hoppings whereas cross-channel diffusion via exchanges. These results stimulated the development of a theoretical model for metal-on-metal fcc(110) epitaxy [9]. According to this model, the anisotropic shape of adislands is caused by an anisotropic corner-rounding process. By controlling the substrate temperature and deposition rate, various kinds of anisotropic Pd adislands can be created on the surface. We were able to grow Pd chains of monoatomic or diatomic width.

Structural changes of the (110) surface of Pd have been induced by Si deposition. At relatively low substrate temperature, already at 150 K, the Si deposition is reactive on Pd (110). On the open (110) face, Si atoms can easily be incorporated in the surface layer between the Pd close-packed rows facilitating the formation of embedded crystalline silicide islands. This newly found crystalline phase of silicide (Pd_2Si) grows with a substantial compressive strain on Pd(110) and is metastable. We have demonstrated that only a small part of the deposited Si atoms react with the Pd substrate to form silicide; the other Si atoms diffuse subsurface. This scenario is very similar to hydrogen penetration into Pd(110). The major difference is the hydrogen solubility in the Pd bulk [1-5] whereas Si and Pd are immiscible [10, 11]. Surface mixing of elements immiscible in the bulk was discovered for metal-on-metal systems [12, 13]. In contrast, in our case the Si atoms diffuse to subsurface sites, in the selvedge just beneath the Pd(110) surface. The Pd atoms ejected from the surface layer during this mechanism once again nucleate at 300 K as dimer chains in the same way as corresponding vacancy islands. The ejected Pd atoms can also react with incoming Si atoms to form silicide adislands.

Comparative experiments were done on Pd(100): silicide formation is also activated above 150 K. In contrast to Pd(110), no crystalline silicide can be grown on Pd(100): on the more compact (100) surface the Si atoms must occupy interstitial sites resulting in a variable corrugation. Amorphous silicide clusters of varying composition are formed.

In order to investigate a reactive and heterogeneous system like Si/Pd, RAIR spectroscopy of adsorbed CO is a valuable complement to STM. The RAIRS technique has proven to be successfull in determining the chemical composition of Si/Pd layers, an information not avalaible by STM only.

References

[1] B. S. Kang and K. S. Sohn, *Diffusion processes and interaction of hydrogen atoms in Pd*, Physica B **205**, 163 (1995).
[2] R. J. Behm, M. Penka, M. G. Cattania, K. Christmann and G. Ertl, *Evidence for "subsurface" hydrogen on Pd(110): An intermediate between chemisorbed and dissolved species*, J. Chem. Phys. **78**, 7486 (1983).
[3] K. H. Rieder, M. Baumberger and W. Stocker, *Selective Transition of Chemisorbed Hydrogen to Subsurface Sites on Pd(110)*, Phys. Rev. Lett. **51**, 1799 (1983).
[4] W. Eberhardt, S. G. Louie and E. W. Plummer, *Interaction of hydrogen with a Pd(111) surface*, Phys. Rev. B **28**, 465 (1983).

[5] T. Engel and H. Kuipers, *A MOLECULAR-BEAM INVESTIGATION OF THE SCATTERING, ADSORPTION AND ABSORPTION OF H2 AND D2 FROM/ON/IN Pd(111)*, Surf. Sci. **90**, 162 (1979).

[6] J. Yoshinobu, H. Tanaka and M. Kawai, *Elucidation of hydrogen-induced (1 x 2) reconstructed structures on Pd(110) from 100 to 300 K by scanning tunneling microscopy*, Phys. Rev. B **51**, 4529 (1995).

[7] G. L. Kellogg, *Field ion microscope studies of single-atom surface diffusion and cluster nucleation on metal surfaces*, Surf. Sci. Rep. **21**, 1 (1994).

[8] L. S. Perkins and A. E. DePristo, *Self-diffusion of adatoms on fcc(110) surfaces*, Surf. Sci. Lett. **317**, L1152 (1994).

[9] Y. Li, M. C. Bartelt, J. W. Evans and A. E. DePristo, *Transition from One- to Two-Dimensional Island Growth on Metal(110) Surfaces Induced by Anisotropic Corner Rounding*, **to be published**, .

[10] W. G. Moffat, *Handbook of binary phase diagram*, Genium Publ. Company, Schenectady (1987).

[11] R. P. Elliot, *Constitution of Binary Alloys, First Supplement*, McGraw Hill, New York (1965).

[12] L. P. Nielsen, F. Besenbacher, I. Stensgaard and E. Laegsgaard, *Initial Growth of Au on Ni(110): Surface Alloying of Immiscible Metals*, Phys. Rev. Lett. **71**, 754 (1993).

[13] H. Röder, R. Schuster, H. Brune and K. Kern, *Monolayer-Confined Mixing at the Ag-Pt(111) Interface*, Phys. Rev. Lett. **71**, 2086 (1993).

List of Publications

[1] E. Hahn, E. Kampshoff, N. Waelchli and K. Kern, *Strain Driven fcc-bct Phase Transition of Pseudomorphic Cu Films on Pd(100)*, Phys. Rev. Lett **74**, 1803 (1995).

[2] N. Waelchli, E. Kampshoff, A. Menck and K. Kern, *Reactions at the Si/Pd(110) interface* in *6th European Conference on Applications of Surface and Interface Analysis*, Montreux 1995, Edited by H. J. Mathieu, B. Reihl and D. Briggs, Wiley, Chichester (1996).

[3] E. Kampshoff, N. Waelchli, A. Menck and K. Kern, *Hydrogen-induced missing-row reconstructions of Pd(110) studied by scanning tunneling microscopy*, Surf. Sci. **360**, 55 (1996).

[4] N. Waelchli, E. Kampshoff and K. Kern, *CO vibrational spectroscopy at heterogeneous Si/Pd(110) surfaces*, Surf. Sci., **in press** (1996).

[5] N. Waelchli, E. Kampshoff, A. Menck and K. Kern, *Silicide growth at metal surfaces: competion between subsurface diffusion and chemical reaction*, submitted to Surf. Sci. Lett. (1996).

Remerciements

Je tiens à sincèrement remercier les personnes qui ont contribué à la réalisation de cette thèse:

- Prof. K. Kern, directeur de thèse, pour m'avoir guidé dans mon travail;

- Dr E. Kampshoff, cheffe de projet, pour son engagement tout au long de ces recherches et ses innombrables conseils;

- Dr H. Brune, Dr K. Kuhnke, Dr J. Barth et Dr V. Marsico pour leurs corrections et suggestions concernant le manuscrit et l'exposé de l'examen oral;

- Dr H. Röder et Dr E. Hahn, mes prédécesseurs qui m'ont transmis leur savoir-faire;

- A. Menck, B. Fischer, K. Bromann, L. Nedelman, O. Cavalleri, A. Hirstein et M. Blanc, mes collègues doctorants, pour leur sympathique collaboration;

- C.-L. Bandelier, C. Blanc, P. Cordey, M. Doy, M. Fazan, G. Grandjean, A. Guisolan, J. Savoie et P. Zürcher, les collaborateurs techniques, pour leur précieuse contribution.

Curriculum Vitae

Nom, prénom:	Waelchli Nicolas
Domicile:	Chemin du Rosy 5
	2013 Colombier
Date de naissance:	31.12.1968
État civil:	Célibataire
Nationalité:	Suisse
Langue maternelle:	Français
Scolarité:	1975 - 1980: Collège primaire de Colombier
	1980 - 1984: Ecole secondaire à Cescole, Colombier
	1984 - 1987: Gymnase Cantonal de Neuchâtel
Études de Physique:	1987 - 1993: Université de Neuchâtel. Travail de diplôme: "Théorie et mesure de photoconductivité transitoire petit signal dans silicium amorphe hydrogéné non-dopé recuit" sous la direction des Prof. H. Beck et A. Shah
Travail de recherche:	1993 - 1996: EPFL, Institut de Physique Expérimentale, "Structure changes at low-index Pd surfaces induced by adsorption and epitaxy" sous la direction du Prof. K. Kern
Assistant de cours:	1993 - 1996: Cours de Mécanique Générale pour étudiants en mécanique et en électricité de 1ere année à l'EPFL du Prof. J.-Ph. Ansermet